

Development of Both Al-Mn and Al-Si System Alloys for a Sustainable Society, and Their As-cast Applicability

(持続可能な社会を実現する Al-Mn 系、Al-Si 系両合金の開発、およびそれらの鋳放し使用可能性)

Dec. 2022

ZEZE XIAO

CONTENTS

Chapter 1 Background and objectives

<i>1.1 Introduction</i>	3
<i>1.2 Development of lightweight material in transportation sectors</i>	5
<i>1.2.1 Introduction of lightweight materials</i>	6
<i>1.2.2 The application of Al alloys in transportation sectors</i>	8
<i>1.3 Introduction of Al-Mn alloys</i>	9
<i>1.3.1 Development of Al-Mn alloys</i>	9
<i>1.3.2 The Properties and application of Al-Mn alloys</i>	9
<i>1.4 Introduction of Al-Si alloys</i>	11
<i>1.4.1 Development of Al-Si alloys</i>	11
<i>1.4.2 The Properties and application of Al-Si alloys</i>	11
<i>1.5 Development of alloy design methods</i>	13
<i>1.5.1 Semi-empirical mode method</i>	13
<i>1.5.2 Molecular orbital theory method</i>	14
<i>1.5.2.1 Ab initio molecular orbital method</i>	14
<i>1.5.2.2 DV-Xα cluster method</i>	15
<i>1.6 Objective of the thesis</i>	17
<i>References</i>	19

Chapter 2 Effects of Si addition on microstructure and mechanical properties of Al-1.5%Mn alloys

<i>2.1 Introduction</i>	27
<i>2.2 Electron parameter for the determination of alloy compositions</i>	28
<i>2.2.1 Electronic parameter representing alloying effects</i>	28
<i>2.2.2 Selection of experimentally alloys</i>	30

2.3 Experimental procedure.....	31
2.3.1 Materials and manufacturing process.....	31
2.3.2 Evaluation of properties.....	32
2.4 Results and discussion.....	33
2.4.1 Microstructures.....	33
2.4.2 Mechanical properties.....	38
2.4.3 Dislocation behavior.....	41
2.4.4 Relationship between M_k values and mechanical properties in Al-1.5Mn- XSi/Mg alloys.....	44
2.5 Summary.....	48
References.....	50

Chapter 3 Effects of Mo and Zr addition on microstructure and mechanical properties of Al-9Si alloy

3.1 Introduction.....	55
3.2 Electron parameter for the designation of the Al-9Si alloys.....	56
3.2.1 Electronic parameter representing alloying effects.....	56
3.2.2 Selection of experimentally alloys.....	58
3.3 Experimental procedures.....	58
3.3.1 Materials and manufacturing process.....	58
3.3.2 Evaluation of properties.....	59
3.4 Results and discussion.....	62
3.4.1 Microstructures.....	63
3.4.2 Solidification behaviors.....	65
3.4.3 Tensile behaviors.....	70
3.4.4 Nanoindentation behaviors in the α -Al phase.....	73
3.4.5 TEM observation for the solidification process.....	75
3.4.6 As-cast application possibility of the 0.2Mo+0.2Zr alloy.....	79
3.5 Summary.....	80
References.....	82

Chapter 4 Effects of Ti and V addition on microstructure and mechanical properties of Al-9Si alloy

4.1	<i>Introduction</i>	86
4.2	<i>Experimental procedure</i>	81
4.2.1	<i>Materials and manufacturing process</i>	81
4.2.2	<i>Evaluation of properties</i>	81
4.3	<i>Results and discussion</i>	83
4.3.1	<i>Microstructural characterization</i>	83
4.3.2	<i>Tensile properties</i>	86
4.4	<i>Summary</i>	93
	<i>References</i>	94

Chapter 5 Investigate the as-cast applicability for different series of Al-Mn and Al-Si alloys by electronic parameters

5.1	<i>Introduction</i>	101
5.2	<i>Proposed method for the estimation of mechanical properties</i>	103
5.3	<i>Results and discussion</i>	105
5.3.1	<i>Microstructural characterization</i>	105
5.3.2	<i>Tensile properties for as-cast applicablity</i>	107
5.4	<i>Summary</i>	111
	<i>References</i>	112
	<i>Appendix</i>	113

Chapter 6 Conclusions.....115

Acknowledgments	117
Published papers with this thesis	118
Presentations	120
Awards	121

Chapter 1

Background and objectives

1.1	Introduction	3
1.2	Development of lightweight materials in transportation sectors	5
1.2.1	Introduction of lightweight materials.....	6
1.2.2	The application of Al alloys in transportation sectors	8
1.3	Introduction of Al-Mn alloys.....	9
1.3.1	Development of Al-Mn alloys	9
1.3.2	The Properties and application of Al-Mn alloys	9
1.4	Introduction of Al-Si alloys.....	11
1.4.1	Development of Al-Si alloys	11
1.4.2	The Properties and application of Al-Si alloys.....	11
1.5	Development of alloy design methods	13
1.5.1	Semi-empirical material design calculation method	13
1.5.2	Molecular orbital theory calculation and design method	14
1.5.2.1	Ab initio molecular orbital method.....	14
1.5.2.2	DV-X α cluster method	15
1.6	Objectives of this study.....	17

References 19

1.1 Introduction

Because of the rapid lack of resources and energy, environmental pollution, ecological destruction, and other social ills in the current industrialized society, how to develop a sustainable society has become an urgent concern. The development of a sustainable society calls on all countries to take action to curb climate change and protect the environment.¹⁻⁴⁾ In recent years, the problem of global warming, which is a long-term increase in the average temperature of the Earth's surface atmosphere and oceans, has become increasingly severe. The statistics are based on scientific temperature observations dating back to the 19th century, and in the 100 years from 1911 to 2010, the global average temperature rose by 0.73K.⁶⁾ Upon assessment, there is no doubt that there is a long-term upward trend. The leading cause of global warming in the second half of the 20th century is considered to be greenhouse gases emitted by human industrial activities. According to the Fourth Assessment Report (AR4), the probability of greenhouse gases causing global warming exceeds 90%.⁷⁾ Figure 1.1 shows the breakdown of gas emissions from the total anthropogenic greenhouse gas emissions. Emissions⁸⁾. This pie chart shows that carbon dioxide significantly impacts global warming. Therefore, CO₂ reduction has become a global proposition.

The transportation sector accounts for about one-fifth of Japan's CO₂ emissions, accounting for 17% and 18% of direct and indirect emissions, respectively. At the same time, the demand for lightweight non-ferrous metals in the automotive industry is increasing by reducing body weight to improve fuel efficiency and mobility. Figure 1.2 shows the change in aluminum production from 1900 to 2014⁹⁾. As can be seen, aluminum production has proliferated since the turn of the century. Compared with traditional iron-based alloys and cast iron, it has high specific strength, high electrical and thermal conductivity, machinability, and good corrosion resistance in the atmosphere. It ranks first in the number of practical metal cracks.

For this reason, it was chosen as a master alloy, and it was widely used not only in the automobile industry but also in structural materials and household appliances. In

addition, producing new aluminum ingots from bauxite requires much electricity. On the other hand, the energy required to remelt scrap aluminum to produce recycled steel is about one-thirtieth of the energy required to produce new steel ingots, saving energy so that aluminum alloys can be recycled.

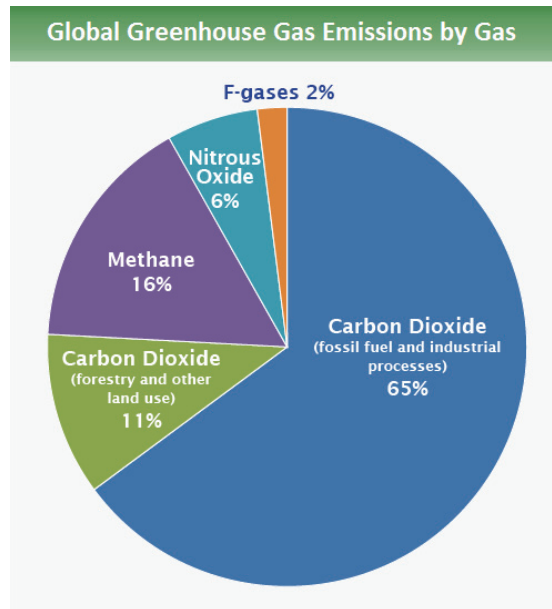


Fig. 1.1 The breakdown of emissions by gas in total greenhouse gas emissions⁸⁾.

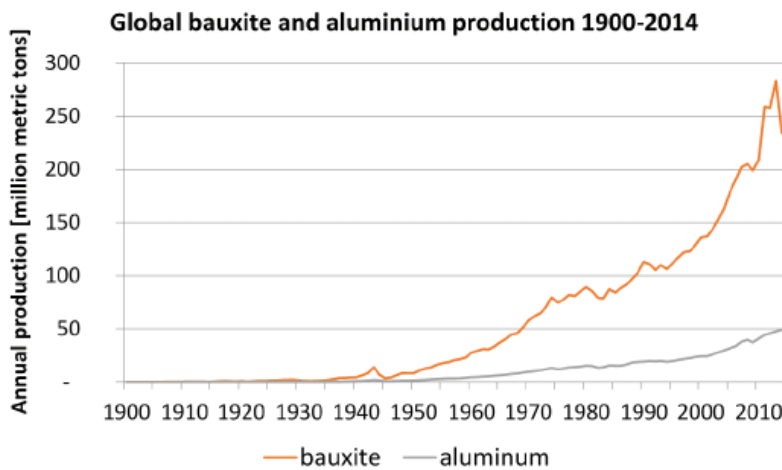


Fig. 1.2 Change of aluminum production in the world⁹⁾.

Many countries and regions in the world have formulated energy-saving and emission-reduction targets. Among the current energy-saving and emission-reduction paths, vehicle light-weighting is the easiest and has a relatively large potential. For passenger gasoline vehicles, for every 100kg reduction, up to 0.39L/100km of fuel can be saved, as shown in Fig. 1.3. On the other hand, for new energy vehicles, it is also necessary to improve the battery life by reducing the weight of the vehicle.

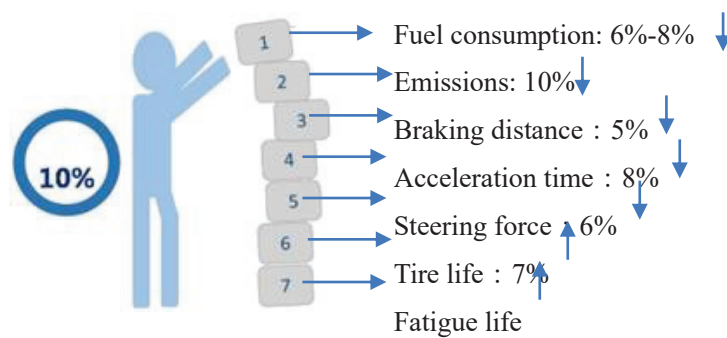


Fig. 1.3 The advantages of 10% weight loss in the vehicle.

1.2 Development of lightweight materials in transportation sectors

Due to the increasingly severe problems of energy and environmental protection, countries around the world pay more and more attention to the research of energy-saving and emission-reduction technology, and the lightweight of automobiles has inevitably become the leading way to achieve the above goals. Automotive lightweight technology is mainly divided into structural optimization, lightweight materials, forming technology, and advanced connection technology. Further, replacing and upgrading automotive materials can reduce the car's total weight from the root, which is highly feasible and is the most critical direction for light weighting of automobiles at present.

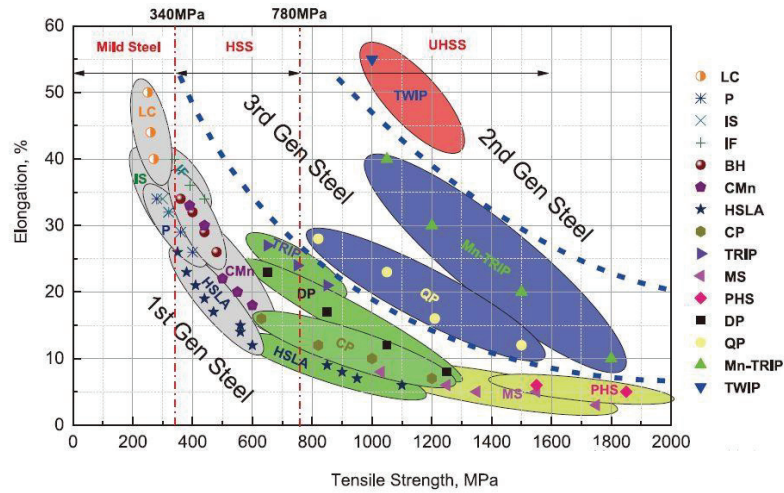


Fig. 1.4 The strength-ductility diagram of high-strength steels.

1.2.1 Introduction of lightweight materials

Advanced high-strength steels include dual-phase steels, multi-phase steels, ferritic+bainitic steels (FB), martensitic steels, transformation-induced plasticity steels, hot-formed steels, and twin-induced plasticity steels). The first and second-generation advanced high-strength steels can meet the application requirements of different components. For example, complex-phase steel and transformation-induced plasticity steel are used in the crash area of automobiles, and their energy absorption effect is significant. For structural parts of the passenger compartment, especially high-strength steels such as martensitic and hot-formed steels can improve safety performance. Due to the lower cost of high-strength steel than other lightweight materials, major car companies and related supporting companies are investing more and more in the research and capital of the third-generation advanced high-strength steel. By adjusting the alloy composition and heat treatment process, these steel grades achieve higher strength and ductility than existing advanced high-strength steels. The joining ability is also more efficient and lowers costs. More properties can be found in the strength-ductility diagram, as shown in Fig. 1.4. However, due to the improvement of the

strength of high-strength steel plates, the traditional cold stamping process is prone to cracking during the forming process, which cannot meet the processing requirements of high-strength steel plates. If the forming conditions cannot be met, the hot stamping technology of ultra-high-strength steel plates is gradually being studied internationally. It is estimated that by 2020, the global demand for advanced high-strength steel for automobiles will be 28.39 million tons, with a compound annual growth rate of 12%.

Magnesium alloys are the lightest commercially available metal structural materials. The density of magnesium is only 1.74 g/cm^3 , which is $2/3$ of aluminum and $2/9$ of steel. Using magnesium alloy can reduce 15%-20% based on using aluminum alloy. Currently, 62% of magnesium alloy products are used in the automobile industry). The countries and regions with many magnesium alloys in the automobile industry are mainly North America, Europe, and Japan. So far, there are more than 60 parts in automobiles using magnesium alloys. Mainly divided into two parts: shell and frame: shell parts include a cylinder head, clutch shell, transmission shell, oil filter shell, air filter shell, transfer case, supercharger shell, lampshade, etc.; Such parts include the steering wheel, instrument panel, fan mount, fender mount, pedal mount, steering mount, brake mount, light mount, seat mount, body mount, door frame, wheel hub, etc. Currently, the most widely used magnesium alloys are body and chassis parts, such as instrument panel frame and beam, seat frame, steering wheel, intake manifold, and various brackets, covers, etc.

1.2.2 The application of Al alloys in transportation sectors

The density of aluminum is $1/3$ of that of steel, the weight is lighter, and it has high specific strength, good extrudability, strong corrosion resistance, and high recyclability. It can be used to manufacture engine parts, shell parts, and other parts on the chassis; deformed aluminum alloys (forged aluminum alloys and aluminum alloy sheets) are also developing rapidly in the application of body parts and structural parts, mainly used in engine covers, fenders, bumpers, floor structures, heat exchangers, wheels, and body

frames). Every year, the total volume of cast aluminum alloys in automotive technology grows steadily. This was especially true in the last decade, when "aluminum" cars started being produced and the number of aluminum-intensive cars exploded. Details such as cylinder blocks, pistons, other engine parts, frames and covers for the different equipment "under the hood" are now traditionally cast from aluminum. All these intricate details and products are manufactured using different casting techniques, producing millions of parts every year. Due to its excellent specific strength, corrosion resistance and relatively low production labor intensity, cast aluminum alloys are also widely used in aerospace, shipping, railway transportation and other transportation economic fields. It is estimated that in 2020, the amount of aluminum used in automobiles will be 5.1 million tons. The CAGR from 2016 to 2020 is 12%, of which SUVs and new energy vehicles will be the fastest-growing areas of automotive aluminum. There are two aspects to limit the application of lightweight materials. One is Cost. Cost is the biggest problem restricting the application of lightweight new materials for automobiles. It is also a problem that has plagued the development of new materials and automobile industries for many years. Figure 1.5 shows the body and panel light cost curve. The other is due to the comprehensive advantages of ordinary high-strength steel in terms of strength, plasticity, impact resistance, recycling, and low cost; at present, the application of ultra-high-strength steel and advanced high-strength steel is still less, and the proportion of use is only 15%. The material strength must be reasonably arranged on the safe force transmission path to effectively absorb the collision energy and ensure the safety of passengers. Then, the suitable material is used in the right place, and the cost of the system is also considered, which is not an easy task.

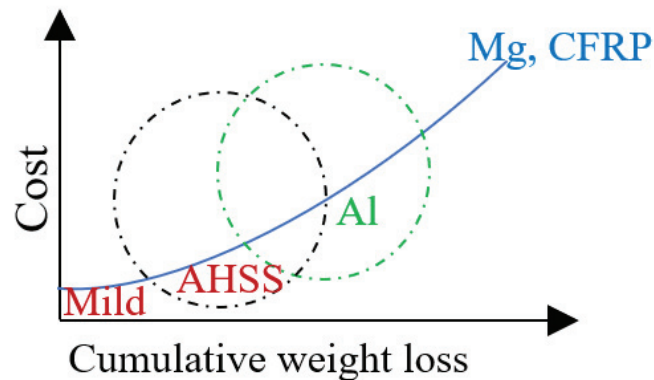


Fig. 1.5 Body and panel lightweight cost curve.

1.2 Introduce of Al-Mn alloys

1.2.1 Development of Al-Mn alloys

The Al-Mn alloys have a long history as practical alloys. Al-Mn alloys mainly include AA3003, AA3004, AA3104, AA3005, and AA3105, etc. The 3003 alloys were already introduced in 1906, and in 1929 the 3004 alloy, a solid solution strengthened with about 1% Mg, was announced⁴²⁾. Mn is counted as one of Al alloys' most important additive elements. The background to the widespread use of Mn as a major additive element is that, in addition to its relatively low price, it can be varied in various ways by adjusting the size and degree of dispersion of precipitated particles. They are non-heat-treatable alloys and show great ductility. This, along with its moderate strength, makes them interesting in many applications, although limited alloys are commonly used.

1.2.2 The properties and application of Al-Mn alloys

The study of alloys is inseparable from phase diagrams. The phase diagrams of Al-Mn alloys were carried out in the early to mid-1900s⁴⁶⁾. The aluminum side of the Al-

Mn binary system is a eutectic reaction, and the phase in equilibrium with the aluminum side solid solution is orthorhombic Al_6Mn . The addition of Mn to the pure Al-Mn binary system is related to the solidification of aluminum. Lower the temperature slightly, and the eutectic temperature is 658.5K Also, the solubility of Mn at this temperature is 1.82 mass%, and the crystal composition is 1.95 % Mn. The reaction occurs along the liquidus to form ternary compounds in the Al-Mn-Si ternary system.

The structure of ternary compound α in equilibrium with Al solid solution is cubic, but researchers have published molecular formulas of $\text{Mn}_2\text{SiAl}_{10}$ ⁵⁴), $\text{Mn}_3\text{SiAl}_{12}$ ⁵⁵), $\text{Mn}_3\text{Si}_2\text{Al}_{15}$ ⁵⁶), etc. Fe is added as an impurity element in the solid alloy, but the constant lattice changes slightly. However, the structure changes in the same cubic crystal structure, but a solid solution of Fe is formed, such as $\text{Al}_{12}(\text{MnFe})_3\text{Si}$ ⁵⁷). Al-Mn series alloys are suitable for application and performance research, limited to AA3003, AA3004, AA3005, and AA3105 alloys. When selecting applications, machine performance, moldability, corrosion resistance, and welding performance are very important. The AA3000 series alloy is used for medium strength, moldability, and corrosion resistance performance applications: AA3003 and AA3004 alloy composite plywood. For example, the water heat exchanger is used to wrap 7072 alloyed AA3003 alloyed skin material. This is an example of a 7072 alloy subject to sun exposure, which can be prevented from occurring, and is usually suitable for use in chemical processing equipment. In addition, the AA3003 alloys for the core material and the 4343 alloys for the skin are also used in the automotive heat exchanger. In addition to these alloys, body AA3104 alloys in the United States have increased in recent years. This is due to the minimum capacity of the heavy melting and recovery of the can body material. At the same time, it is possible to collect different ingredients in the open tank lid.

1.3 Introduce of Al-Si alloys

1.2.1 Development of Al-Si alloys

Al-Si alloy has good casting performance, which is why it is the most widely used casting iron alloy, suitable for various casting methods. Si is the primary alloying element addition, with high alloy casting performance, improved fluidity, low thermal cracking tendency, low reduced density, high airtightness, obtainable structural density, With metal fitting good resistance and moderate strength but very low plasticity. Si is the second phase in the alloy structure, and the casting performance of the alloy is improved, but the base strength of the Si alloy is equally uniform and weak ($\text{Si} > 7\%$). For this reason, the focus of research on Al-Si alloys is to strengthen the alloying elements, modify the second phase structure, reduce the alloy content, etc., to achieve high mechanical performance.

1.2.2 The properties and application of Al-Si alloys

Due to financial requirements, reducing vehicle weight is becoming increasingly important. For such an objective, Al-Si cast alloys have been widely employed to produce automotive components working at ambient and fairly high temperatures due to excellent characteristics such as low-cost manufacturing, excellent castability, high specific strength and recyclability⁵⁷⁻⁶⁰). Si is the main and most important alloying element of Al-Si casting alloys. In Al-Si alloys, the Si content usually varies between 5 and 12%. Si is primarily responsible for what is known as "good castability," the ability to easily fill molds and solidify castings without hot tearing or cracking problems. The more Si content in the alloy, the lower the coefficient of thermal expansion. Si is a tough phase; therefore, it contributes significantly to the wear resistance of the alloy. Si combines with other elements to increase the strength of the alloy and make the alloy heat treatable. Alloys containing more than 7% Si form upon solidification a three-dimensional eutectic Si network of interconnected Si platelets embedded in a ductile-Al

matrix. The contribution to the strength of Al-Si alloys is caused by the load transfer from the α -Al matrix to the rigid, highly interconnected Si plate^{61,62}. The load-carrying capacity of eutectic silicon can be reduced by spheroidization, thereby improving the machinability, ductility and fatigue resistance of the alloy. When Al-Si cast alloys are exposed to high temperatures, the eutectic Si grains are first fragmented and spheroidized, then coarsened, and their aspect ratio is reduced, leading to loss of interconnectivity of the eutectic phase⁶³⁻⁶⁹. The rate at which interconnectivity is lost is highly dependent on temperature and exposure time. reported that increasing the Si content from 7% to 12% in a low-alloying Al-Si casting alloy resulted in an increase in yield strength and ultimate tensile strength (σ_{UTS}) to 22 and 25 MPa at 523 K, respectively⁷⁰⁻⁷⁵. The application of aluminium alloys in the as-cast condition has attracted great attention in recent years in view of reducing production costs.⁷⁶⁻⁸⁰ For example, the Silafont-30 (Al-9SiMg) showed the 0.2% proof stress ($\sigma_{0.2}$) of 90-150MPa, σ_{UTS} of 180-240MPa and the fracture strain (ϵ_f) of 2-9% in the as-cast condition.⁷⁶ The alloy compositions are referred to in mass % unless otherwise noted. And this alloy has been applied to the automobile parts, such as cylinder heads for compressors, compressor housing, and intermediate flange for SF₆ switch system.⁷⁶

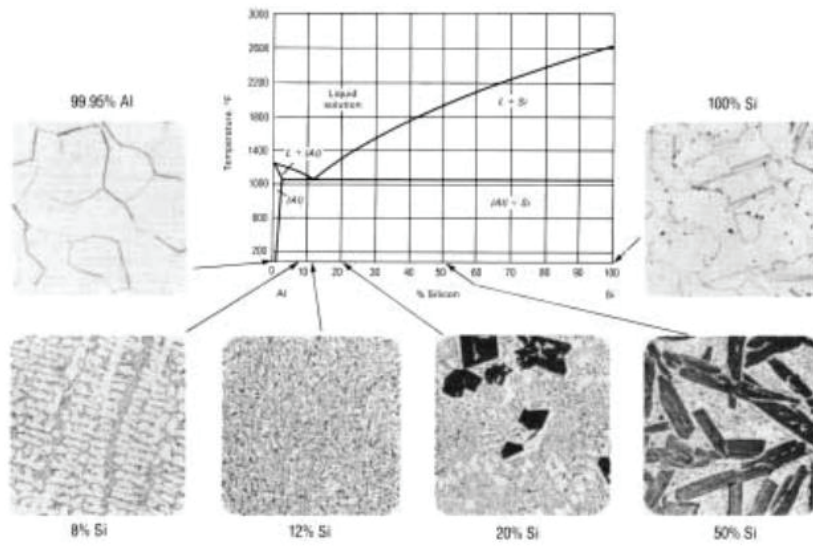


Fig. 1. 6 Aluminum-silicon phase diagram and cast microstructures of pure components and alloys of various compositions.

1.4 Development of alloy design methods

It is a general material design method adopted by most researchers to confirm material components with the best performance by seeking rules through many technological tests. Almost all kinds of literature on the development of Al alloy have introduced the experimental method that adopts a “tentative” test. Although some tests adopt the orthogonal test method to reduce tests amount, this “tentative” test is time-consuming and laborious and needs significant economic losses.

The alloy design refers to that researching alloy with a specific target performance, under the guidance of theory, to confirm which alloy element needs to be added to base metal and its quantity and to forecast the property. Based on efficient, scientific, economical, and predictive requirements of science development to material design, it will be the inevitable trend to conduct material design through calculation. Along with the condition that continuous development of metal materials on the theory of microstructure, phase structure, atomic structure (or electronic structure), energy band theory, chemical bond theory, electronic theory, and also the continuous development of computer technology, the material scientific design continues to mature and moves toward experimental stage gradually. The following contents will introduce a variety of methods of alloy design.

1.4.1 Semi-empirical mode method

This method predicts material structure and property based on existing experimental data. Since 1996, Japan Engineering Manufacturing Center (RACE) has been funded by Japan Science and Technology Association for a long term and has established LPF (Linus Pauling File) database. This database covers the structure, diffraction, composition, intrinsic properties, and other information of alloys, intermetallic compounds, ceramics, minerals, and so on ⁸¹). At least 200,000 data items related to structure, diffraction, and intrinsic properties, and 35 thousand data items recorded since 1900 are stored in this knowledge information system. Based on this robust material

database with accuracy beyond 95%, prediction for material properties can be realized only by entering the atomic number and considering possible compound composition⁸¹). LPF researchers think that, based on the LPF database, a knowledge-information system can be established by taking advantage of existing science principles, and new materials can be predicted and developed systematically by calculation.

1.4.2 Molecular orbital theory method

Molecular orbital theory refers to the study of electronic motion states based on quantum chemical calculations. This method can design and predict the structure and performance of materials macroscopically. Molecular orbital theory is based on non-relativistic approximation, Born-Oppenheimer approximation, and orbital approximation. Its basic concept is to regard the molecule as a whole; the atomic orbital corresponding to each atom in the molecule is composed of several molecular orbitals; then Arranging the atoms in a series of molecular orbitals, the atoms belong to the whole molecule. Among them, the ab initio method and the Discrete Variational (DV)-X α cluster method are widely used in the field of material design.

1.4.2.1 Ab initio molecular orbital method

The ab initio method is a quantum theory all-electronic calculation method that uses only Planck's constant, electron rest mass, and electricity quantity, three physical constants without any empirical parameters to solve the quantum electronic theory. This method is based on three approximations of molecular orbital theory. In principle, any exact suitable solution for approaching to self-constant field limit can be obtained as long as one suitable function is selected and the number of self-consistent iterations is sufficient. The ab initio method is somewhat better than the semi-empirical method, can obtain the electronic motion status of various systems (ions, molecules, clusters, and chemical reaction systems) and relevant microscopic information, and can explain or predict reasonably atomic bonding, molecular structure, chemical reaction process,

nature of the material and related experimental observations. However, due to the complexity of the calculation system, the calculated amount and occupied computer storage spaces of the ab initio method increase dramatically, which constantly puts forward new tasks for computer technology.

On the other hand, the error of the ab initio method is mainly from non-relativistic approximations and orbital approximations. Currently, the configuration interaction method is mainly adopted to correct these errors. However, this method increases the demand for computer memory and machine hour, obviously, so this method is hard to realize for larger molecules.

2.4.2.1 DV- $X\alpha$ cluster method

The $X\alpha$ method was first used by Slater in 1951⁸²). The DV- $X\alpha$ cluster method is based on the Hartree-Fock-Slater approximation, which provides relatively accurate electronic structures even for broader cluster systems. In this approach, the potential energy of Slater's local electron exchange involves the interaction between electrons. V_{XC} is given by eq.(1-1) as below:

$$V_{XC} = -3\alpha[3\rho(r)/8\pi]^{1/3} \quad (1-1)$$

where $\rho(r)$ is the local electron density and the parameter α is fixed at 0.7. The calculation uses self-consistent electronic approximation, and the matrix elements are integrated by a discrete sampling method. Hamiltonian matrix elements and overlapping integrals are computed by random sampling⁸²). Molecular orbitals consist of linear combinations of atomic orbitals. Compared with the ab initio method, the DV- $X\alpha$ clustering method does not have a unique physical model, but only an improvement in the computational method. Its accuracy is generally slightly lower than the ab initio method. Nevertheless, because it has adopted the localized density functional approximation of exchange potential, it does not need to calculate many multi-center integrals. Its calculated quantity is only 1/100 of the ab initio method. This method is one of the standard methods of calculating heavy atom-containing molecules and solid atom clusters.

The d-electron concept based on theoretical calculation of electronic structure proposed by Morinaga et al.^{83,84)} has been applied in the design of high-performance alloys such as Al⁸²⁻⁸⁷⁾, Bi⁸⁸⁾, Ni⁸⁹⁻⁹²⁾ and Ni⁸⁹⁻⁹²⁾ Ti⁹³⁻⁹⁶⁾. This concept successfully predicts some physical or chemical properties of the designed alloys.⁸³⁾ The bond order (Bo) and d-orbital levels of transitional alloying elements (Md) are used in this concept. Bo is a measure of the strength of the covalent bond between atoms. In addition, Md is involved in charge transfer. Md was also found to be related to the electronegativity and atomic radius of the element.¹³⁾ Both electronegativity and atomic radius are classical parameters that have been used to describe the properties of chemical bonds between atoms in solids.¹⁵⁾ For aluminum alloys of s and p simple metals, the value of ΔMk is defined by the average composition of the s orbital energy level. See Section 2 for details. Compared with other alloy design methods, it is easier for practical application.⁸¹⁻⁸³⁾ Figure 1.7 is the relation of ΔMk and alloy tensile strength⁸⁹⁾. This method is highly convenient and effective in predicting the mechanical properties of multi-component alloys and the design of high-performance alloys.

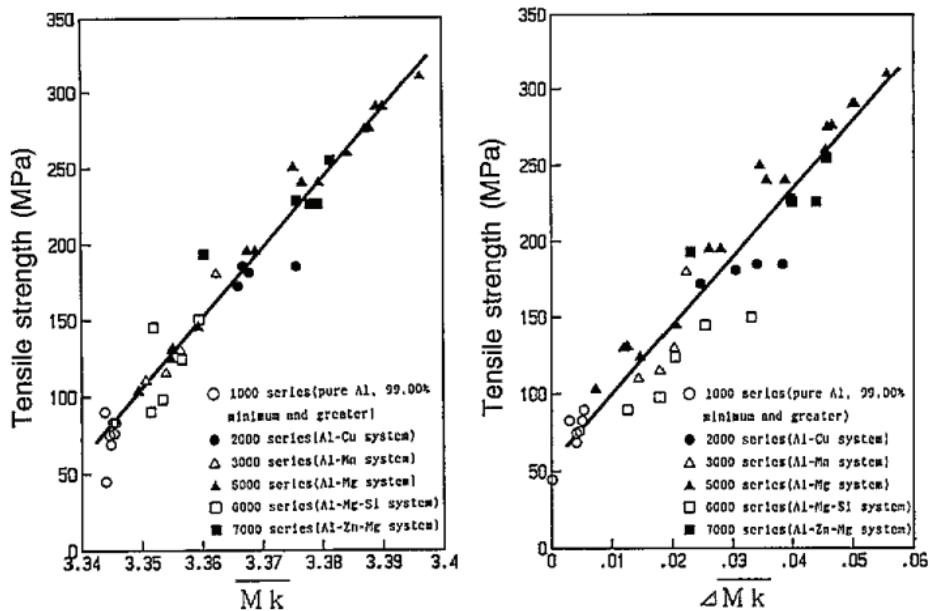


Fig. 1.7 Correlation of the tensile strength with (a) Mk and (b) ΔMk for the Al alloys.

1.4 Objectives of this study

With the rapid development of the industry and the increasing attention to environmental issues, the research of designing and improving the properties of aluminum alloys for low cost and improving the proportion of aluminum alloys used in lightweight materials is imminent. Different series of aluminum alloys, Al-1.5Mn and Al-9Si with multiple components, were chosen for low-cost alloys as the as-cast applications, and the target mechanical values and reference commercial of Al-Mn and Al-Si alloys are shown in Table 1. It is essential to find a prediction method for the mechanical properties of Al alloys irrespective of the alloy series.

1. Al-1.5Mn was chosen as the base alloy, and 1.0 and 3.3Si were added to it to maintain the same ΔMk values as Al-1.5Mn-0.8 and 2.4Mg alloys, respectively. The relationship between their microstructure, mechanical properties and electronic parameters was investigated experimentally on Al-1.5Mn-Si alloys. It was also compared with the Al-1.5Mn-Mg alloy, showing the applicability of the as-cast alloy due to its excellent tensile properties.

2. Al-9Si-0.3Fe-0.15Mn alloy is selected as the base alloy, and 0.2Mo, 0.2Zr, 0.2Mo+0.2Zr, 0.2Ti and 0.2V are added to the base alloy to maintain ductility and increase strength. The effects of tensile properties and their alloying on the solidification microstructure, solidification path, and tensile properties were investigated to develop low-cost alloys for as-cast applications.

Table. 1 Target mechanical values and reference commercial of Al-Mn and Al-Si alloys.

Properties	Target values	Reference commercial Al alloys
Ultimate tensile strength, σ_{UTS}/MPa	> 150	Al-Mn alloy (AA3005)
Fracture strain, %	> 9	
Ultimate tensile strength, σ_{UTS}/MPa	> 160	Al-Si alloy (A356)
Fracture strain, %	> 7	

3. Among these parameters, the s-orbital energy level Mk was found to be suitable for estimating the mechanical properties of commercial aluminum alloys with multiple

components. This paper presents a series of results and will propose a new approach to the mechanical properties of Al-1.5Mn and Al-9Si alloys.

References

- 1) Parris, Thomas M., and Robert W. Kates. "Characterizing and measuring sustainable development." *Annual Review of environment and resources*, **28** (2003) 559-586.
- 2) Rogers P P, Jalal K F, Boyd J A. *An introduction to sustainable development*[M]. Routledge, 2012.
- 3) Mitlin, D.. *Sustainable development: A guide to the literature*. *Environment and urbanization*, **4** (1992), 111-124.
- 4) Chichilnisky, Graciela. "What is sustainable development?." *Land Economics* (1997): 467-491.
- 5) F. W. Gayle, G. Becka, A. Syed, J. Badgett, G. Whitten, T. Y. Pan, A. Grusd, B. Bauer, R. Lathrop, J. Slattery: *JOM* **53** (2001) 17-21.
- 6) M.Gupta, W.L.E. Wong. *Materials Characterization*. **105** (2015) 30-46.
- 7) Saevarsdottir G, Kvande H, Welch B J. Aluminum production in the times of climate change: The global challenge to reduce the carbon footprint and prevent carbon leakage[J]. *JOM*, 2020, 72(1): 296-308.
- 8) Ashby, M.F., Evans, A.G., Fleck, N.A., Gibson, L.J., Hutchinson, J.W., and Wadley, H.N.G., *Metal Foams: A Design Guide* (Butterworth-Heinemann, Boston, 2000.
- 9) Ashby, M.F., *Materials Selection and Mechanical Design*, 2nd ed. (Butterworth-Heinemann, Oxford, 1999.
- 10) Clark, J.P., Roth, R. and Field, F.R., in *ASM Handbook Volume 20: Materials Science and Design*, edited by Dieter, G.E. (ASM International, Materials Park, OH, 1997.
- 11) Ashby, M.F., *Acta Mater.* **48** (2000) 359-369.
- 12) Allen, H.G., *Analysis and Design of Structural Sandwich Panels* (Pergamon Press, Oxford, 1969.
- 13) Agarwal, B.L. and Sobel, L.H., *AIAA J.* **14** (1977) 1000-1011.
- 14) Koiter, W.T., *Koninkl. Nederl. Akademie van Wetenschappen—Amsterdam, Ser.*

- B, **66** (1963)265-276.
- 15) Hutchinson, J.W., *Adv. Appl. Mech.* **14** (1974) 67-80.
 - 16) Budiansky, B. and Hutchinson, J.W., in *Contributions to the Theory of Aircraft Structures* (Delft University Press, Delft, The Netherlands, (1972) 239.
 - 17) Budiansky, B. *Int. J. Solids Struc.* **36** (1999) 3677-3708.
 - 18) Catchpole, E.J., *J. R. Aeronaut. Soc.* **58** (1954) 765-768.
 - 19) Evans, A. G.. *Lightweight materials and structures. MRS bulletin*, **26** (2001) 790-797.
 - 20) Campbell, Flake C., ed. *Lightweight materials: understanding the basics.* ASM international, 2012.
 - 21) Farrar, D.J., *J. R. Aeronaut. Soc.* **53** (1949) 1041-1052.
 - 22) Gerard, G. *Minimum Weight Analysis of Compression Structures* (New York University Press, New York, 1956.
 - 23) Tvergaard, V. *Int. J.Solids Struc.* **9** (1973) p.177-198.
 - 24) Weaver, P.M. and Ashby, M.F., *Prog. Mater. Sci.* **41** (1997) 61-75.
 - 25) Parkhouse, J.G., in *Proc. 3rd Int. Conf. on Space Structures*, edited by Nooschin, H. (Elsevier, London, 1984) 367.
 - 26) Weaver, P.M. and Ashby, M.F., *J.Eng. Design* **7** (1996) 129-150.
 - 27) Wicks, N. and Hutchinson, J.W., *Int. J. Solid. Struc.* **38** (2001) 5165-5183.
 - 28) Evans, A.G., Hutchinson, J.W., Fleck, N.A., Ashby, M.F., and Wadley, H.N.G., *Prog. Mater. Sci.* **46** (2001) 309-315.
 - 29) Deshpande, V.S. and Fleck, N.A., *J. Mech. Phys. Solids* **48** (2000) 1253-1269.
 - 30) Fuller, R.B., *Patent, U.S. No.2,986, 241* (1961).
 - 31) Evans, A.G., Hutchinson, J.W., and Ashby, M.F., *Prog. Mater. Sci.* **43** (1999) 171-175.
 - 32) Chiras, S. Mumm, D.R., Evans, A.G., Wicks, N. Hutchinson, J.W., Dharmasena, K. Wadley, H.N.G., and Fichter, S. *Int. J.Solids Struc.* in press.
 - 33) Sypeck, D.J. and Wadley, H.N.G., *J. Mater. Res.* **16** (2001) 890-897.
 - 34) Wallach, J.C. and Gibson, L.G., *Int. J. Solids Struc.* submitted for publication.

- 35) Bart-Smith, H., Hutchinson, J.W., and Evans, A.G., *Int. J. Mech. Sci.* **43** (2001) 1045-1963.
- 36) Gibson, L.J. and Ashby, M.F., *Cellular Solids: Structure and Properties*, 2nd ed. (Cambridge University Press, Cambridge, 1997).
- 37) Hyun, S. and Torquato, S. J. *Mater Res.* **16** (2001) 280-285.
- 38) Mumm, D.R., Chiras, S. Evans, A.G., Hutchinson, J.W., Sypeck, D.J., and Wadley, H.N.G., *Acta Mater.* to be published.
- 39) Fleck, N.A. (personal communication).
- 40) Wadley, H.N.G. and Sypeck, D.J. (personal communication).
- 41) Hutchinson, J.W. and He, M.Y., *Int. J. Solids Struc.* **37** (2000) 6777-6794.
- 42) A. J. McAlister, J. L. Murray: *Journal of Phase Equilibria* **8** (1987) 438-447.
- 43) Zhen Li, Zhen Zhang, X. -Grant Chen: *Mater. Sci. Eng. A* **729** (2018) 196-207.
- 44) K. Liu, X. -Grant Chen: *Mater. Sci. Eng. A* **697** (2017) 141-148.
- 45) K. Liu, X. -G. Chen: *Materials & Design* **94** (2015) 340-350.
- 46) K. Matsugi, S. Yamamura, Z.F. Xu, Y.B. Choi, K. Sugio, G. Sasaki and N. Oda: *Mater. Trans.* **56** (2015) 1675-1682.
- 47) Kamat, R. G: *JOM* **48** (1996) 34-38.
- 48) Y. J. Li, L. Arnberg: *Acta Materialia* **51** (2003) 3415-3428.
- 49) Jiantao Liu, Robert E. Dick, Joseph M. Fridy, Thomas N, Rouns: *Mater. Sci. Eng. A* **458** (2007) 73-87.
- 50) M. Zamin: *Corrosion* **37** (1981) 627-632.
- 51) D. Park, J. G. Morris: *Scripta Metallurgica et Materialia* **29** (1993) 365-369.
- 52) F. G. Coury, C. S. Kiminami, W. J. Botta, C. Bolfarini, M. J. Kaufman: *Materials & Design* **110** (2016) 436-448.
- 53) Zhen Li, Zhen Zhang, X. -Grant Chen: *Mater. Sci. Eng. A* **708** (2017) 383-394.
- 54) Hu Ting, Yin Dengfeng, Yu Xinxiang, Cheng Rence, Cao Hanquan: *Rare Metal Materials and Engineering* **47** (2018) 2631-2636.
- 55) Shiyun Ruan, Christopher A. Schuh: *Acta Materialia* **57** (2009) 3810-3822.

- 56) M. Somerday, F. J. Humphreys: *Materials Science and Technology* **19** (2003) 20-29.
- 57) Javidani M, Larouche D. Application of cast Al–Si alloys in internal combustion engine components[J]. *International Materials Reviews*, 2014, 59(3): 132-158.
- 58) Zhuang W. Z. and Swansson N. S.: ‘Thermo-mechanical fatigue life prediction: a critical review’, 1998, Melbourne, Vic., Australia, DSTO Aeronautical and Maritime Research Laboratory.
- 59) Neu R. and Sehitoglu H.: *Metall. Mater. Trans. A*, 1989, 20, (9), 1755–1767.
- 60) Riedler M., Leitner H., Prillhofer B., Winter G. and Eichlseder W.: *Meccanica*, 2007, 42, (1), 47–59.
- 61) Minichmayr R., Riedler M., Winter G., Leitner H. and Eichlseder W.: *Int. J. Fatigue*, 2008, 30, (2), 298–304.
- 62) Su X., Zubeck M., Lasecki J., Sehitoglu H., Engler-Pinto C. C., Tang C. Y. and Allison J. E.: ‘Thermomechanical fatigue behavior of materials’, 2003, W. Conshohocken, PA: ASTM International.
- 63) Wilfried E., Gerhard W., Robert M. and Martin R.: *Recent Trends in Processing and Degradation of Aluminium Alloys*, InTech, Montanuniversität Leoben, Austria, 2011, 14, 329–346.
- 64) Löhe D., Beck T. and Lang K. H.: 5th Int. Conf. on ‘Low cycle fatigue’, 161–175; 2004, Berlin, Germany: Deutscher Verband für Materialforschung und-prüfung.
- 65) Tichánek R., Španiel M. and Divi M.: *Acta Polytech.*, 2005, 45, (3), 43–48.
- 66) Španiel M. and Tichánek R.: *MECCA J. Middle Eur. Constr. Des. Cars*, 2004, 2, (2).
- 67) Fuoco R. and Moreira M. F.: *AFS Trans*, 2009, 117, 225–240. [Google Scholar]
- 68) Thalmair S., Thiele J., Fischersworing-Bunk A., Ehart R. and Guillou M.: *SAE Technical Paper*, 2006, 01–0541.
- 69) Shojaefard M. H., Ghaffarpour M. R., Noorpoor A. R. and Alizadehnia S.: *Proc. Inst. Mech. Eng., Part D*, 2006, 220, (5), 627–636.

- 70) Lee K. S., Assanis D. N., Lee J. and Chu K. M.: SAE Technical Paper, 1999, 01–0973.
- 71) Shalev M., Zvirin Y. and Stotter A.: *Int. J. Mech Sci.*, 1983, 25, (7), 471–483.
- 72) Thomas J. J., Verger L., Bignonnet A. and Charkaluk E.: *Fatigue Fract. Eng. Mater. Struct.*, 2004, 27, (10), 887–895.
- 73) Bertodo R. and Carter T. J.: *J. Strain Anal.*, 1971, 6, (1), 1–12.
- 74) Takahashi T., Nagayoshi T., Kumano M. and Sasaki K.: SAE Technical Paper, 2002, 01–0585.
- 75) Norris P. M., Hoag K. L. and Wepfe W.: *Exp. Heat Transfer*, 1994, 7, (1), 43–53.
- 76) RHEINFELDEN ALLOYS GmbH & Co. KG: Primary Aluminum Casting alloys (2016) 17-63.
- 77) Silvia Lombardo, Ildiko Peter, Mario Rosso: *Materials Today: Proceedings* **10** (2019) 271-276.
- 78) Mohammadreza Zamani, Hoda Dini, Ales Svoboda, Lars-Erik Lindgren, Salem Seifeddine, Nils-Eric Andersson, Anders E. W. Jarfors: *International Journal of Mechanical Science* **121** (2017) 164-170.
- 79) M. Morinaga, N. Yukawa, and H. Adachi: *Tetsu-to-Hagane* **72** (1986) 555-562.
- 80) M. Morinaga, N. Yukawa: “Alloy Design Base on Molecular Orbital Method” *Computer Aided Innovation of New Materials*, Amsterdam (1991) 803-808.
- 81) M. Morinaga, S. Nasu, H. Adachi, J. Saito, and N. Yukawa: *J. Phys. Condens. Matter* **3** (1991) 6817-6828.
- 82) M. Morinaga and S. Kamado: *Model. Simul. Mater. Sci. Eng.* **1** (1993) 151-164.
- 83) Zeze Xiao, Kazuhiro Matsugi, Zhefeng Xu, Yongbum Choi, Kenjiro Sugio, Nobuyuki Oda and Jinku Yu: *Mater. Trans.* **61** (2020) 1255-1361.
- 84) K. Matsugi, S. Yamamura, Z.F. Xu, Y.B. Choi, K. Sugio, G. Sasaki and N. Oda: *Mater. Trans.* **56** (2015) 1675-1682.
- 85) R. Ninomiya, H. Yukawa and M. Morinaga: *J. Japan Inst. Light Metals* **44** (1994) 171-177.
- 86) Zeze Xiao, Kazuhiro Matsugi, Zhefeng Xu, Taishi Matsuoka, Tomoshi Uomi,

- Nobuyuki Oda, Hironobu Kominato, and Yasuo Uosaki: PRICM-10, Xi'an (CHINA MACHINE PRESS) (2019) 449-456.
- 87) Meiqi Yu, Zhenfeng Xu, Yong Bum Choi, Takuma Konishi, Kazuhio Matsugi, Jinku Yu, Satoshi Motozuka, Kenichiro Suetsugu: *Mater. Trans.* **58** (2017) 140-147.
- 88) M. Morinaga, N. Yukawa, H. Adachi, and H. Ezaki: The Metallurgical Society of AIME, Warrendale (Superalloys 1984) (1984) 523-532.
- 89) R. Nomiya, H. Yukawa, M. Morinaga: *Alloys. Compd.* **215** (1994) 215-232.
- 90) K. Matsugi, Y. Murata, M. Morinaga, and N. Yukawa: The Minerals, Metals and Materials Society, Warrendale (Superalloys 1992) (1992) 307-316.
- 91) K. Matsugi, T. Endo, Y. B. Choi and G. Sasaki: *Mater. Trans.* **51** (2010) 740-748.
- 92) K. Matsugi, Y. Murata, M. Morinaga and N. Yukawa: *Mater. Sci. Eng. A* **172** (1993) 101-110.
- 93) M. Morinaga, Y. Murata, and H. Ezaki: *Material Chemistry in Nuclear Environment, Tsukuba (Proc. Int. Symp.)* (1992) 241-252.
- 94) K. Matsugi, H. Mamiya, Y. B. Choi, G. Sasaki, O. Yanagisawa and H. Kuramoto: *Int. J. Cast Metals Res.* **21** (2008) 156-161.
- 95) XiLong Ma, Kazuhiro Matsugi, Zhefeng Xu, Yongbum Choi, Ryohei Matsuzaki, Zifeng Lin, Xingang Liu and Hao Huang: *Mater. Trans.* **60** (2019) 2426-2434.
- 96) XiLong Ma, Kazuhiro Matsugi, Zhefeng Xu, Yongbum Choi, Ryohei Matsuzaki, Zifeng Lin, Xingang Liu and Hao Huang: *Mater. Trans.* **61** (2020) 740-749.

Chapter 2

Effects of Si addition on microstructure and mechanical properties of Al-1.5Mn alloys

<u>2.1</u>	<u>Introduction</u>	27
<u>2.2</u>	<u>Electron parameter for the determination of alloy compositions</u>	28
<u>2.2.1</u>	<u>Electronic parameter representing alloying effects</u>	28
<u>2.2.2</u>	<u>Selection of experimentally alloys</u>	30
<u>2.3</u>	<u>Experimental procedures</u>	31
<u>2.3.1</u>	<u>Materials and manufacturing process</u>	31
<u>2.3.2</u>	<u>Evaluation of some properties</u>	32
<u>2.4</u>	<u>Results and discussion</u>	33
<u>2.4.1</u>	<u>Microstructures</u>	33
<u>2.4.2</u>	<u>Mechanical properties</u>	38
<u>2.4.3</u>	<u>Dislocation behavior</u>	41
<u>2.4.4</u>	<u>Relation between M_k and mechanical properties in Al-1.5Mn-xSi/Mg alloys</u>	44

<u>2.5</u> <u>Summary</u>	48
<u>References</u>	50

2.1 Introduction

The Al-Mn series alloys¹⁾ are extensively used in industry because of their excellent corrosion resistance, moderate mechanical strength, and high ductility. It can be considered that solid solution strengthening can be achieved by adding a small amount of elements to the alloys²⁻⁵⁾. Previous research⁴⁾ using Al-1.5Mn alloy as the base, and Ca, Zn, Mg, and Ti were selected as alloying elements, and the relationship between mechanical properties and ΔMk value were studied in detail. According to the relationship between the tensile properties and the ΔMk value, the composition of the alloy was determined to be Al-1.5Mn-2.4Mg, and the ΔMk value was 0.029, which was used as an indicator of the solid solution strengthening level of the alloy. This as-cast alloy, which was the champion data, showed $\sigma_{0.2}$ of 135 MPa, σ_{UTS} of 270 MPa and ϵ_f of 18%, and excellent corrosion resistance in NaCl solution, leading to as-cast application to automotive structural parts.

The d-electron concept proposed by Morinaga et al.^{6, 7)} based on theoretical calculation of electronic structure has been applied to the design of high-performance alloys such as Al^{4, 8-10)}, Bi^{11, 12)}, Ni¹³⁻¹⁵⁾ and Ti^{16, 17)}, this Concept successfully predicts some physical or chemical properties of the designed alloy.⁴⁾ The bond order (Bo), which is a measure of the strength of the covalent bond between atoms and the d-orbital level of the transitional alloying element (Md), which is related to charge transfer have been used in d-electron concept¹⁸⁾. Md is also found to be related to the electronegativity and atomic radius of the element.⁴⁾ Electronegativity and atomic radius are both classical parameters used to describe the nature of chemical bonds between the atoms in the solids.⁹⁾ For Al alloys with s, p simple metal, the ΔMk values are defined by taking the compositional averages of s-orbital energy level as described in later, which is easy to use in practical application compared to other alloy design methods.^{18, 31-33)}

In this chapter, in order to develop low-cost Al alloys, the Al-1.5Mn was selected as the base alloy, and 1.0 and 3.3Si were added to maintain the same ΔMk values as Al-1.5Mn-0.8 and 2.4Mg⁴⁾ alloys, respectively. The relationship between their

microstructures, mechanical properties, and electron parameters was investigated experimentally on Al-1.5Mn-Si alloys. It was also compared with the Al-1.5Mn-Mg alloys, showing the applicability of the as-cast alloy due to its superior tensile properties.

2.2 Electron parameter for the determination of alloy compositions

2.2.1 An electronic parameter representing alloying effects

Parameters for compositional optimizations of Al alloys had been obtained from electronic methods for alloy design.⁸⁻¹⁰⁾ The electronic parameter Mk_i is the s-orbital energy level above the Fermi energy level of the iAl_{18} cluster, containing the alloying element i and its surrounding Al atoms.²⁰⁾ Various parameters have been proposed to describe the alloying behavior. However, the elements' electronegativity and atomic radius were chosen here because they represent the properties of chemical bonds between atoms in solids.²⁰⁾ There was a good correlation between the atomic radius or electronegativity of transition metals and the Md parameter of d-orbital energy level, as discussed in section 1. For s, p simple metals such as Al, the d-orbital energy level was no longer valid in transition metal-based alloys. The Mk_i is an s-orbital energy level exciting above the Fermi energy level, and obtained it from the discrete variational $X\alpha$ ³⁴⁾ (DV- $X\alpha$) cluster calculation. Therefore, the alloy effect inevitably involved Mk_i .²⁰⁾ It is well known that the calculated energy levels of the DV- $X\alpha$ cluster represent the electronegativity itself.^{19, 20)}

The Mk_i values of each alloy element calculated by the iAl_{18} cluster model in FCC Al is shown in Table 2.1.^{19, 20)} The Mk_i value decreased as electronegativity increasing. In contrast, it increased with the atomic radius of the elements, as shown in Fig. 2.1.^{19, 20)} In addition, the p-orbital energy levels can be considered instead of the s-orbital energy level. However, for studying the mechanical properties of aluminum alloys, spherically symmetric s-orbitals may be better than oriented p-orbitals.²⁰⁾

Table 2.1 List of Mk_i values of alloying elements in the FCC Al cluster.^{19, 20)}

Elements	Mk_i (eV)	Elements	Mk_i (eV)	Elements	Mk_i (eV)
Li	5.096	Sc	5.200	Cu	4.037
Be	3.650	Ti	5.009	Zn	3.290
Na	5.036	V	4.782	Ga	3.013
Mg	4.136	Cr	4.601	Ge	2.614
Al	3.344	Mn	4.443	Zr	5.433
Si	2.680	Fe	4.328	Nb	5.227
K	6.196	Co	4.314	Mo	5.079
Ca	5.550	Ni	4.248		

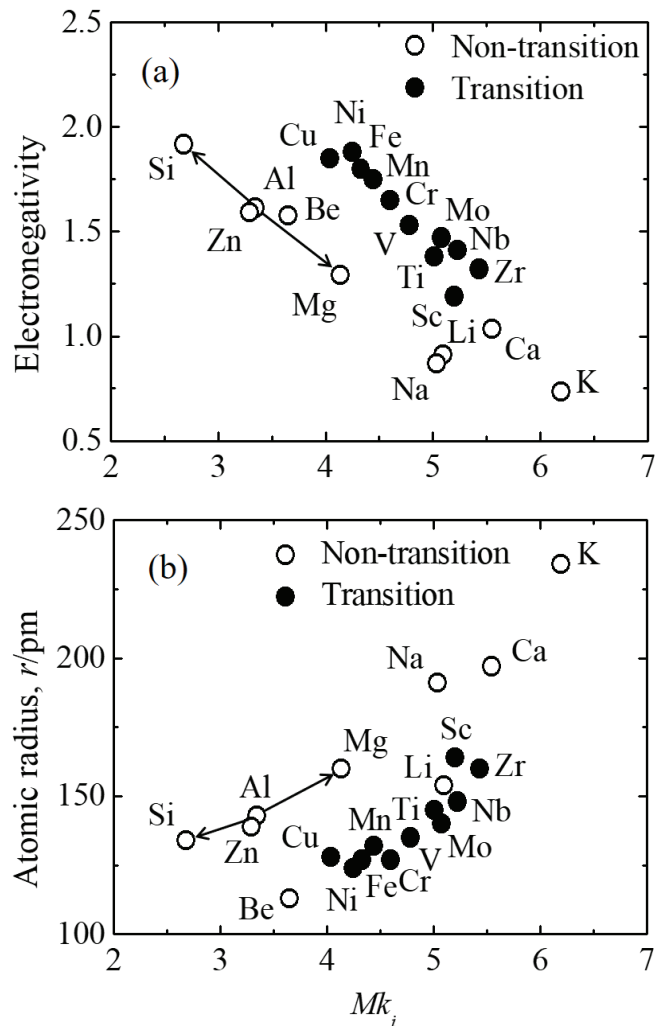


Fig. 2.1 Relationship between Mk_i values and the (a) electronegativity, (b) atomic radius of elements: \circ non-transition metals and \bullet transition metals.^{19, 20)}

Except for Si, Zn, Ga, and Ge, most elements have Mk_i value higher than Al. For alloys, the two mean values of the s-orbital energy levels, Mk_t and ΔMk , are defined by taking compositional averages using the equation (2-1) and (2-2).

$$Mk_t = \sum x_i Mk_i \quad (2-1)$$

$$\Delta Mk = \sum x_i |Mk_i - Mk_m| \quad (2-2)$$

Where x_i is the mole fraction of component i in the alloy, Mk_i and Mk_m are the Mk value of component i and Al, respectively. When all elements in the alloy have Mk_i value above or below Al, two averages differ only by a constant deviation of 3.344 from the Mk_m value; therefore, there is no essential difference between them. But when the elements with higher and lower Mk_i values are mixed in the alloy, the meaning of the two average values is different.²⁰⁾

2.2.2 Selection of experimentally alloys

In this chapter, Si added alloys were designed based on the Al-1.5Mn alloy, maintaining the same ΔMk values as those of Al-1.5Mn-0.8 and 2.4Mg¹⁵⁾ alloys, respectively. There were opposite alloying vectors between Al and Si and Al and Mg, as shown in Fig. 2.1, because the alloying vector is considered in the selection of alloying elements, so the same alloying effect is respected due to the same vector.^{25,28)} The ΔMk values for 0.8 and 2.4Mg addition alloys, showing that the as-cast was suitable due to the excellent tensile properties, are 0.015 and 0.029, respectively. Therefore, the ΔMk values for 1.0 and 3.3Si addition alloys were 0.015 and 0.029, respectively. The Mk_t values of 1.0 and 3.3Si addition alloys were also 3.346 and 3.331, respectively. The Al-1.5Mn-XSi (X: 0.0, Al-1.5Mn; 1.0; 3.3) alloys was also designed in this study, as mentioned above.²⁸⁾

2.3 Experimental procedure

2.3.1 Materials and manufacturing process

Al-Mn and Al-Si master alloys were used to prepare the experimental alloys, and the target Si concentrations of 0.0, 1.0 and 3.3 were achieved by adding Al. The constant melting temperature is maintained at 963~993K for 1.2ks. The melt is then poured into a steel mold preheated to 423K. The steel ingot is cooled to room temperature in the steel mold. The ingot size was 190mm×23mm×39mm.

2.3.2 Evaluation of properties

Samples for microstructural observation using an optical microscope (OM) and an electron probe microanalyzer (EPMA) equipped with a wavelength-dispersive X-ray spectrometer (WDS) and a transmission electron microscope (TEM, JEM-2010, JEOL, Japan). Image-pro software was used to measure the volume fraction and secondary dendrite arm spacing of the experimental alloys. Measure secondary dendrite arm spacing using OM images with precise scales. The line intercept method³⁵⁾ was used to measure the secondary dendrite arm spacing, and at least 100 dendrites were taken to determine the secondary dendrite arm spacing.

The X-ray diffraction (XRD) patterns of the experimental alloys were the particle sizes obtained by using an X-ray diffractometer (D/max-2500PC, Rigaku, Japan) with Cu radiation ($\lambda = 0.15418$ nm, 40 kV, 200 mA) during the scanning step 0.001° , with silicon as the internal standard. Lattice constants were calculated from the interplanar spacing of the (111), (200), (220), (311) and (222) plane Al-1.5Mnd according to Bragg's law. Choose a minimum scan step size of 0.001° to determine the angular precision of the lattice constants. Therefore, the lattice constants of the experimental alloys have five significant figures.

Tensile specimens with a diameter of 6 mm and a gauge length of 60 mm were machined from the ingot. Tensile tests were performed at room temperature with an

initial strain rate of $6.7 \times 10^{-4} \text{ s}^{-1}$ using a testing machine (DCS-R-5000, SHIMADZU, Japan). Tensile strain up to necking was accurately measured by using an extensometer.

To reveal the dislocation behavior at 1%, 5% and 10% flow stress levels in tensile tests, 1%, 5% and 10% plastic strains in cold rolling were applied to Al-1.5Mn-XSi samples and annealed at 453K for 3.6ks. The dislocation density was measured by the equal thickness fringe method using regions with a thickness greater than 100 nm in the TEM sample. Estimate the dislocation density (ρ) using Eq. (2-3). Values of ρ are measured on arbitrary cross-sections over 50 regions per sample.

$$\rho = n / A \quad (2-3)$$

Where n and A are the numbers and area of dislocation in an arbitrary cross-section, respectively.

Nanoindentation experiments were performed on the α -Al phase of each alloy by instrumentation (ENT-1100a, Elionix, Japan) using a Berkovich diamond indenter at room temperature. Measurements were performed at a holding load (load control) of 30 mN, loading within 30 s, holding at peak load for 10 s, and unloading each sample within 30 s. Nanoindentation hardness (H_{IT}) was calculated using the Oliver-Pharr method³⁶⁾ as shown in Eq. (2-4) and (2-5) respectively according to the load-depth curve.

$$H_{IT} = P_{max} / A_p \quad (2-4)$$

$$A_p = 23.46 \times h_c^2 \quad (2-5)$$

Where H_{IT} is the nanoindentation hardness of the α -Al phase, P_{max} is the maximum indentation load, A_p is the indentation's projected area, and h_c is the indentation depth.

2.4 Results and discussion

2.4.1 Microstructures

The optical micrographs of the Al-1.5Mn and Al-1.5Mn with 1.0Si and 3.3Si addition alloys are shown in Fig. 2.2 (a), (b), and (c), respectively. Dendritic structures with different sizes were obtained in the alloys, and these dendritic structures predominantly

consisted of the α -Al phase. The measured average dendrite size of the α -Al phase decreases from 104.3 μm for the Al-1.5Mn alloy to 98.7 μm for the 1.0 Si addition alloy and 43.1 μm for the 3.3 Si addition alloy. Fig. 3 and Table 3 illustrate the XRD analysis results and the quantitative EDS analyses of chemical compositions of various phases in the alloys. Combined with EDS and XRD analyses, the microstructure of the Al-1.5Mn alloy mainly consists of α -Al matrix and a few Al_6Mn compounds. Compared with the Al-1.5Mn alloy, irregular-shaped intermetallic compounds were also observed in the Al-1.5Mn-xSi alloys. Quantitative EDS analysis indicated that the irregular-shaped phase consists of Al, Mn, and Si. The results of XRD analyses in Fig. 2.3 confirm that the compound is similar to the $\text{Al}_{12}\text{Mn}_3\text{Si}$ phase. The XRD analysis results also show that both the most substantial diffraction peak and the most significant peak sum of the α -Al phase, compared with the diffraction peaks of the other phase, imply that the α -Al matrix was the dominant phase. In addition, quantitative EDS analysis shows that a part of Si dissolved into the α -Al phase and the Si content in the α -Al matrix increases with the increase of Si in the Al-1.5Mn-xSi alloys. The smallest average dendrite size of the α -Al was obtained in the 3.3Si addition alloy. It can be seen that the refinement effect was gradually enhanced with an increase in the Si content. The reduction in dendrite size was mainly attributed to a significant number of the formation of $\text{Al}_{12}\text{Mn}_3\text{Si}$, which was uniformly distributed along the grain boundaries.

To better understand the evolution of the $\text{Al}_{12}\text{Mn}_3\text{Si}$ phase concerning Si content in the Al-1.5Mn-XSi alloys, optical micrographs of Fig.2.2 have been investigated by image pro software, and the obtained results are demonstrated separately in Table 2.1. The volume fraction of the α -Al phase in Al-1.5Mn-XSi alloy was 99.3%, 98.6%, and 96.1%, respectively. There is no $\text{Al}_{12}\text{Mn}_3\text{Si}$ phase in Al-1.5Mn alloy, and the volume fraction of the $\text{Al}_{12}\text{Mn}_3\text{Si}$ phase increases from about 1.4% to 3.6% when Si content in the Al-1.5Mn-XSi alloys is improved from 1.0 to 3.3 mass%. The volume fraction of each phase through the image analysis method is shown in Table 2.1. The transformation from Al_6Mn to $\text{Al}_{12}\text{Mn}_3\text{Si}$ intermetallic phase has been reported earlier in the reference²⁰). Therefore, it was believed that the amount of the $\text{Al}_{12}\text{Mn}_3\text{Si}$ phase

mainly depends on the Si content in the Al-1.5Mn-xSi alloys. Different Si content changes the size and content of the Al₁₂Mn₃Si phase in the Al-1.5Mn-xSi alloys. It can be seen that the amount of the Al₁₂Mn₃Si phase with a bigger size increase with the increase of Si content. As shown in Fig. 2.2(d), (e), and (f), the proportion of Al₁₂Mn₃Si phase with a smaller size (<1 μm²) decreases from 42.8% to 39.6% when Si content increases from 1.0 to 3.3 mass%. The proportion of the coarser particles (>10 μm²) is improved from 5.8% (1.0 Si) to 7.33% (3.3Si).

Figure 2.4 shows a typical DTA curve obtained from Al-1.5Mn-XSi alloys cooling at 5 K min⁻¹. There was one exothermic peak in Al-1.5Mn alloy during the cooling process, and this peak was the precipitation of the α-Al phase. The extrapolated onset temperature on point P₁ was 925 K. The liquidus temperature of the α-Al phase took place at 920 K, which corresponded to the first exothermic peak during the cooling process in the 1.0 Si addition alloy. A significant change in the 3.3 Si addition alloy was the signals on point P₃, situated at about 842 K, corresponding to the eutectic reaction temperature.

Furthermore, the liquidus temperature took place at 902 K. In addition, the exothermic peak of the Al₁₂Mn₃Si phase (point P₂) was obtained in 1.0 and 3.3 Si addition alloys, and their extrapolated onset temperature was about 906 K. The decrease in liquidus temperature could increase the number of solid solution elements in the α-Al phase. It was worth noting that the precipitation temperature of the Al₁₂Mn₃Si phase was higher than that of the α-Al phase in Si addition alloy. It was considered that the Al₁₂Mn₃Si phase acted as nucleation sites of the α-Al phase, thereby refining the alloy's microstructure. The solidification sequence was consistent with the change of microstructure which has been shown in Fig 2.2.

Based on the analyses mentioned above, the addition of Si promoted the formation of the Al₁₂Mn₃Si phase, which was distributed along the α-Al grain boundary. Moreover, the volume fraction and the size of the Al₁₂Mn₃Si phase increased with the increase in Si content. Moreover, with the increase of Si addition, the content of Si dissolved into the α-Al phase also improved. As illustrated in Table 3, the solubility of Si in the α-Al

phase among the Al-1.5Mn with 0.0, 1.0, and 3.3 Si addition alloys were 0.0, 0.7, and 1.2 mol%, respectively. However, it should be noted that the content of Si dissolved in the α -Al phase hardly did not change in the 3.3 Si addition alloy. It indicated that the addition of Si in this alloy system mainly led to the formation of the $\text{Al}_{12}\text{Mn}_3\text{Si}$ phase and the solid solution of Si in the α -Al phase had a specific limitation, as shown in the XRD results in Fig. 2.3, respectively.

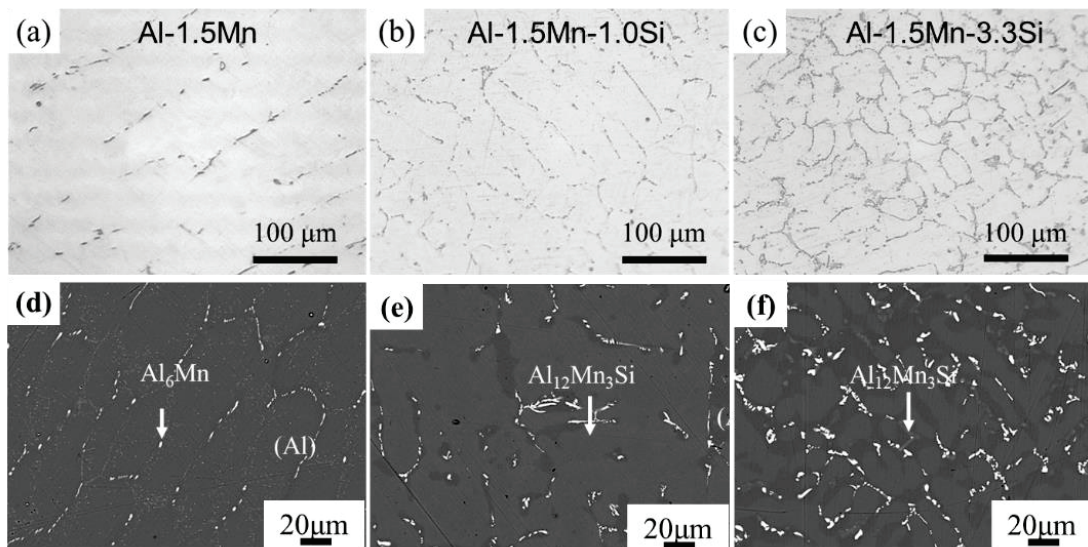


Fig. 2.2 The OM and BSE images of the (a) and(d): Al-1.5Mn, (b)and(e): 1.0Si and (c)and(f): 3.3Si addition experimental alloys.

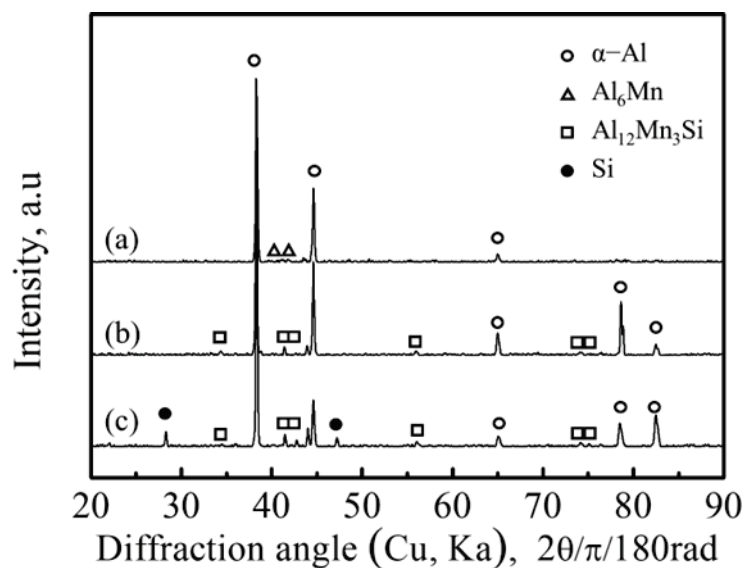


Fig. 2.3 XRD of the Al-1.5Mn-XSi alloys.

The number of nucleation sites of the α -Al grain increased due to the increment of Si addition. More, the melting points of alloys decreased with the increment of Si content. The slower diffusion rate of the solute elements led to the small secondary dendrite arm spacings. The compositions of the α -Al phase varied with the Si content, as listed in Table 2.2, which was caused by the change in the partition ratio between the α -Al phase and the eutectic for each element.²⁸⁾ The partition ratio of Mn and Si in the α -Al phase was exchanged by the increment of Si content, which led to the small amount of Mn in the 3.3Si addition alloy.²⁸⁾ The Mk_α values of the three alloys differ less than Mkt , as shown in Table 2.2. It can be considered that the alloy has reached a sufficient solid solubility. The Mk_α value for each alloy is defined by the measured composition in the α -Al phase listed in Table 2.2, and this value probably corresponds to the level of solid solution strengthening of the α -Al phase.

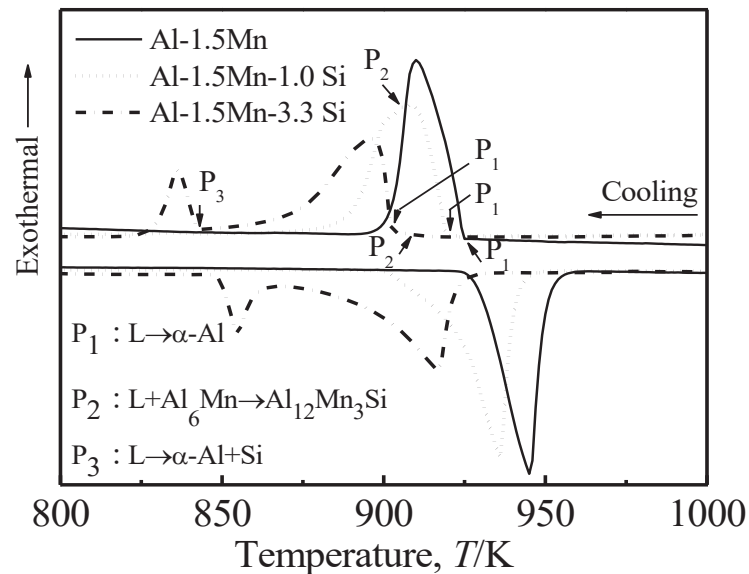


Fig. 2.4 DTA curves obtained from Al-1.5Mn-XSi alloys.

Table 2.2 The Mk_t and ΔMk values of experimental and reference¹⁵⁾ alloys and their compositions in the α -Al phase.

Experimental and reference alloys (mass%)	Mk_t	ΔMk	Compositions in the α -Al phases (mass%)			Mk value (Mk_α) in the α -Al phase
			Mn	Si	Mg	
Experimental alloys:						
Al-1.5Mn-0Si (Base)	3.35	0.01	1.31	-	-	3.35
Al-1.5Mn-1.0Si (1.0Si)	3.35	0.02	1.31	0.71	-	3.35
Al-1.5Mn-3.3Si (3.3Si)	3.33	0.03	1.01	1.27	-	3.34
Reference alloys:						
Al-1.5Mn-0.8Mg (0.8Mg) ²⁷⁾	3.36	0.02	1.42	-	0.79	3.36
Al-1.5Mn-2.4Mg (2.4Mg) ²⁷⁾	3.37	0.03	1.45	-	2.17	3.37
Al-1.5Mn-6.0Mg (6.0Mg)	3.41	0.06	1.46	-	2.58	3.38

Figure 2.5 shows the relationship between ΔMk values and the experimental alloys' lattice constant, Mk_α or Mk_t values. The lattice constant decreased linearly with the increase in ΔMk values. It was believed that the decrease of the lattice constant was related to the content of solid solution elements in the α -Al phase. The Mk_α and Mk_t values of the Al-1.5Mn alloy with a ΔMk value of 0.008 were the same, implying the formation of the α -Al phase by perfect dissolution of the added elements. In contrast, 1.0 and 3.3 Si with ΔMk values of 0.015 and 0.029 showed different values between Mk_α and Mk_t , implying that the composition of α -Al phase and eutectic was determined by a certain distribution ratio of each element, or both determine the existence of the solid solution limit of each element in the α -Al phase and the increase of the eutectic.

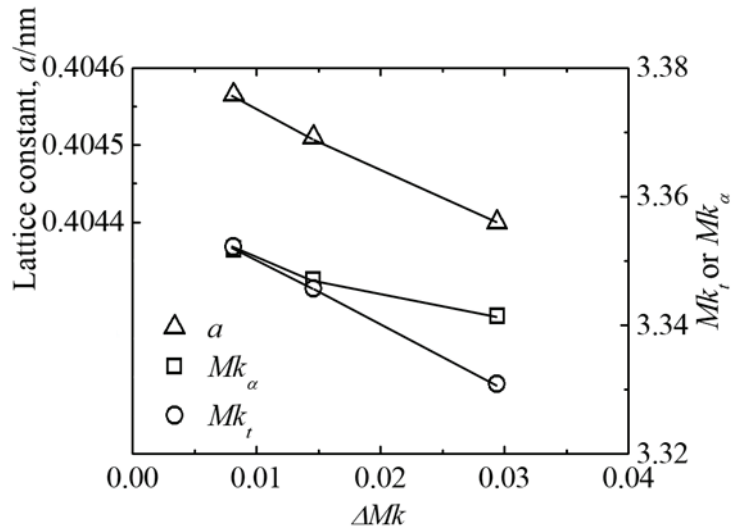


Fig. 2.5 Relationship between ΔMk values and the lattice constant, Mk_α or Mk_t values of the experimental alloys.

2.4.2 Mechanical properties

The nominal tensile stress-strain curves for the Al-1.5Mn-XSi alloys are shown in Fig. 2.4, and the nominal tensile stress-strain curves of the A1070 and Al-1.5Mn-6.0Mg have been reported previously¹⁵⁾ and studied from reference. The A1070 specimen was sufficiently annealed for minimum strength. The Al-1.5Mn alloy exhibits a stronger plastic deformation behavior, compared with the A1070. The $\sigma_{0.2}$, σ_{UTS} and ϵ_f values of the Al-1.5Mn alloy were 47MPa, 95MPa, and 18%, respectively. The alloy with 1.0Si addition exhibited stronger tensile properties, with the $\sigma_{0.2}$ of 61MPa, σ_{UTS} of 148MPa, and ϵ_f of 18%, compared with the Al-1.5Mn alloy. The alloy with the addition of 3.3Si exhibited the highest value of all flow stresses. However, ϵ_f was reduced to 9%. The sawtooth in the stress-strain curves of Si addition alloys was very pronounced, which indicated the Portevin-Le Chatelier effect³⁷⁾ due to the barrier to dislocation migration, including Si atoms mainly distributed in the α -Al phase. The increase in flow stress implied the increase in strength due to the increase in the level of solid solution strengthening and dislocation strengthening in the alloys, caused by the increase in ΔMk

value of alloys, as well as Al-1.5Mn-xMg alloys.²⁸⁾ The addition of Si increased the tensile strength of the alloys and decreased the ϵ_f . Al₁₂Mn₃Si and Si phases in the eutectic region were distributed along the grain boundary. During the tensile test, the crack propagated along the interface between its phase and α -Al phase, and the ϵ_f of 3.3Si alloy with a large amount of its phase decreased significantly. In addition, some shrinkage defects were observed in the Al-1.5Mn and Si addition alloys. But the cracks were propagated along the interface of the Al₁₂Mn₃Si or Si and the α -Al phase in the eutectic region.²⁸⁾ Therefore, shrinkage defects were not considered as factors affecting tensile properties.

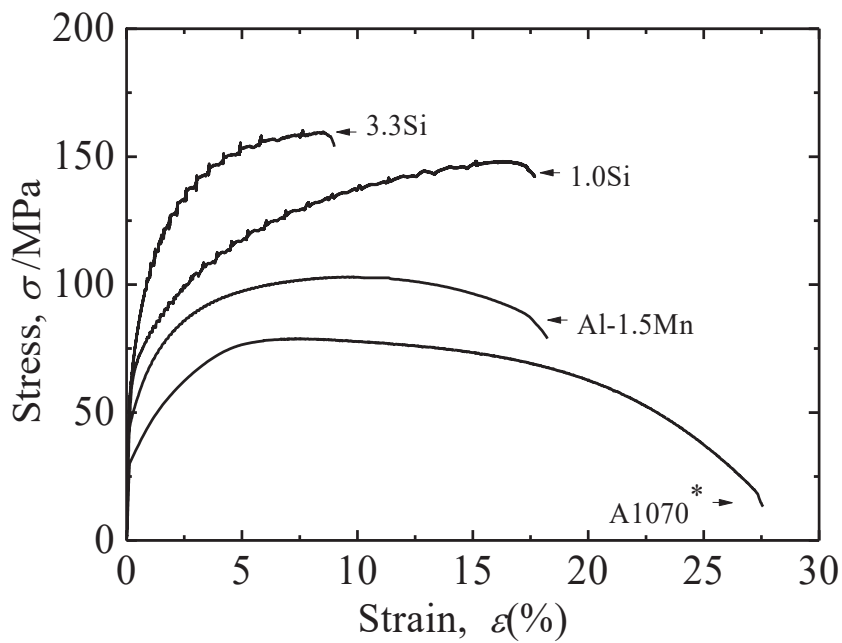


Fig. 2.6 Nominal tensile stress-strain curves of the experimental alloys.

To investigate the influence of the α -Al phase as the dominant phase on the relative mechanical properties, the nanoindentation experiments were performed using the experimental alloys and A1070. Figure 2.7 shows the typical load (P)-depth (h) curves obtained from the nanoindentation experiments. The P-h curves had similar behaviors regardless of the alloys.²⁸⁾ The α -Al phase of the 3.3Si addition alloy showed the lowest depth under the constant load, which could be attributed to solid solution strengthening.

28) This also means that the highest solid solution strengthening of the α -Al phase can be achieved by adding Si or reducing the Mka value, as shown in Figure 2.3.

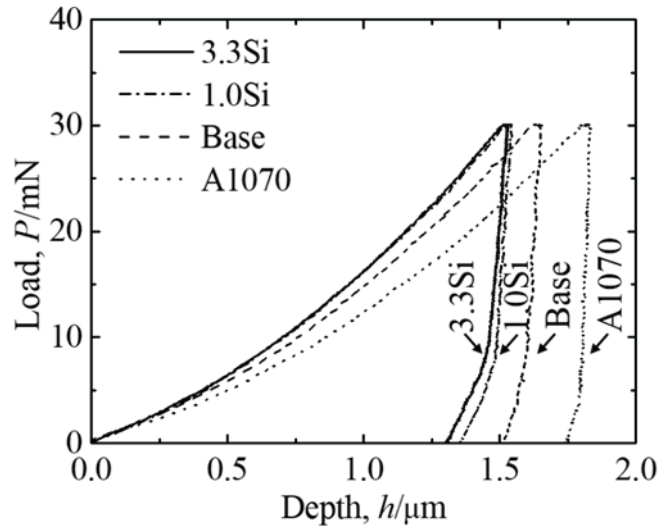


Fig. 2.7 Load-depth curves of the nanoindentation experiments of the experimental alloys and A1070.

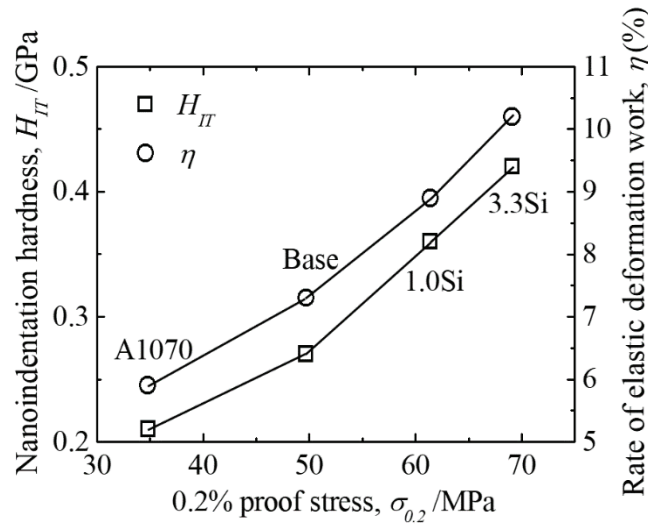


Fig. 2.8 Relationship among the nanoindentation hardness, the rate of elastic deformation work of the α -Al phase, and the $\sigma_{0.2}$ of the experimental alloys and A1070.

From the P-h curves, the nanoindentation hardness and rate of elastic deformation work were obtained from the Oliver-Pharr method³⁵). The rate of elastic deformation

work was defined as the ratio of elastic deformation work to the total deformation work, that was, the possibility of predicting the magnitude of $\sigma_{0.2}$ by this rate. Figure 2.6 shows a good linear relationship between the nanoindentation hardness of the experimental alloys and A1070, the rate of elastic deformation work of the α -Al phase, and $\sigma_{0.2}$. It can be considered that the tensile properties, such as the above-mentioned flow stress and ε_f , were mainly explained by using the level of solid solution strengthening of the α -Al phase. However, the eutectic had some influence on the Al-1.5Mn-xSi alloy.

2.4.3 Dislocation behavior

To reveal the dislocation behavior in 1%, 5% and 10% flow stress in tensile tests, 1%, 5% and 10% plastic strains in cold rolling were applied to Al-1.5Mn-XSi specimens and anneal at 453 K for 3.6 ks. TEM was used to observe their dislocation behavior. Figure 2.7 shows the typical dislocation behaviors obtained from the dark-fields of the α -Al phase since the flow stress levels were mainly determined by the solid solution strengthening level of the α -Al phase, as shown in Fig. 2.6. The 1% plastic deformation of the Al-1.5Mn alloy led to the formation of dense dislocation entanglements in the α -Al phase.¹⁵⁾ Due to the increased dislocation mobility, the characteristic dislocation cell structure can only be observed in the 1% strained Al-1.5Mn alloy. Compared with the Al-1.5Mn alloy, at the same plastic strain level, the dislocations of the 1.0 and 3.3Si alloys are more uniform and densely distributed in the α -Al phase. The lower dislocation mobility of 1.0 and 3.3Si addition alloys was due to the fact that dislocations were trapped in the α -Al phase by uniformly distributed solute elements, resulting in a uniform dislocation distribution.

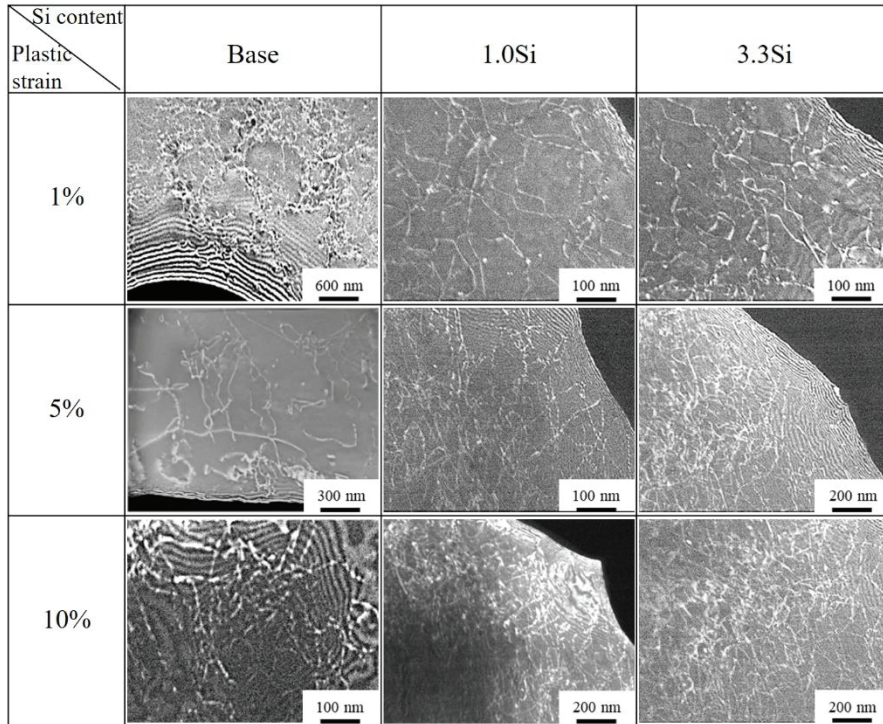


Fig. 2.9 TEM dark-field images on 1, 5, and 10% plastic strained specimens of the experimental alloys

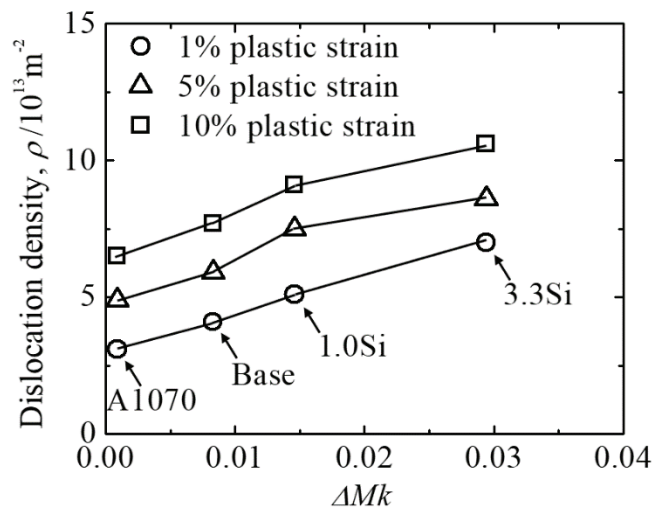


Fig. 2.10 Relationship between ΔMk values and dislocation density on 1, 5, and 10 % plastic strained specimens of the experimental alloys and A1070¹⁵⁾.

The dislocation density values for 1%, 5% and 10% strain plastic specimens are shown in Fig. 2.8. Dislocation densities were measured in alloys with strains of 1%, 5%, and 10%. However, the cellular structure was partially observed in the Al-1.5Mn alloy. The dislocation densities of the experimental alloys and A1070¹⁵⁾ varied linearly with the value of ΔMk . Read the flow stress values at 1%, 5% and 10% strain in the tensile curve shown in Figure 2.4. Figure 2.9 shows a good relationship between ΔMk value and the flow stress corresponding to 1%, 5% and 10% strain for the experimental alloys and A1070¹⁵⁾. Here, the A1070 specimen deformed in homogeneously during the tensile tests at 10% strain. The center of the gauge length showed the contraction, as shown in Figure 2.4. Since the value in ϵ_f for the 3.3Si addition alloy was 9.0 %, the value of the fracture stress of 154 MPa was used as the 10% flow stress level. The behavior of the flow stress change was qualitatively consistent with the change of the dislocation density, as shown in Fig. 2.8, which mean that ΔMk can be used to predict the flow stress level or $Mk\alpha$ value through the solid solution strengthening and dislocation strengthening of the α -Al phase.

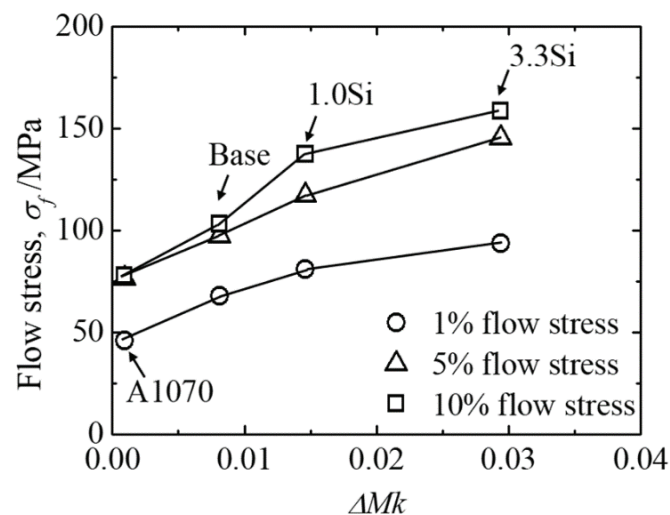


Fig. 2.11 The relationship between ΔMk values and the flow stress corresponds to the experimental alloys in 1, 5, and 10% strained

The validity of this predictive method was strongly demonstrated by examining various data on the mechanical properties of Al-1.5Mn-xSi and Al-1.5Mn-xMg¹⁵⁾ alloys.

Although dislocation density is well correlated with ΔMk values, specifically, how to physically understand this parameter within the framework of dislocation theory is unknown. It can be assumed that the dislocation theory consists of elastic and Al-1.5Mn interactions on the shear modulus effect. The yield stress of FCC solid solution alloys was explained to be due to the hindering effect of solute atoms on dislocation motion.³⁸⁾ The effects are likely due to dislocations and pinning of solute atoms.³⁹⁾ However, according to the pinning model, the solute-dislocation interactions may be mainly attributed to elastic interactions (such as the Cottrell effect) and interactions caused by the shear modulus effect.⁴⁰⁾

2.4.4 Relation between Mk values and mechanical properties in Al-1.5Mn-XSi/Mg alloys

Previously, the literature¹⁵⁾ reported the compositional optimization of Al-Mn-X alloys. Mg exhibits a higher Mki value than Al. However, as shown in Figure 2.1, the Mki value of Si is lower than that of Al. The alloying vectors of Si and Mg both show relative magnitudes and opposite directions, since the alloying vectors were determined from Al to the i ^{25, 26)}, a specific interaction between Si and Mg may be implied in the Mkt value, regardless of the value of ΔMk , as defined in Eq. (1) and (2). Table 2.2 shows the Mkt and ΔMk values for the experimental and reference¹⁵⁾ alloys. The addition of Mg and Si in Al-1.5Mn alloy implied the tensile and compressive stress fields around their replacing elements, respectively.

For example, the Mk_i value of the 3.3Si addition alloy was 3.331, which was lower than that of the Al-1.5Mn alloy (3.352). In contrast, the 2.4Mg addition alloy maintained the same ΔMk value (0.029) as the 3.3Si addition alloy, showing a higher Mk_i value (3.373) than the Al-1.5Mn alloy. The α -Al phase acted as the dominant phase. It directly affects the properties of the experimental alloys, as shown in Figs. 2.3 and 2.6. Establishing a relationship between microstructural or mechanical properties and the $Mk\alpha$ of the α -Al phase in the Al-1.5Mn-XSi alloys is necessary.

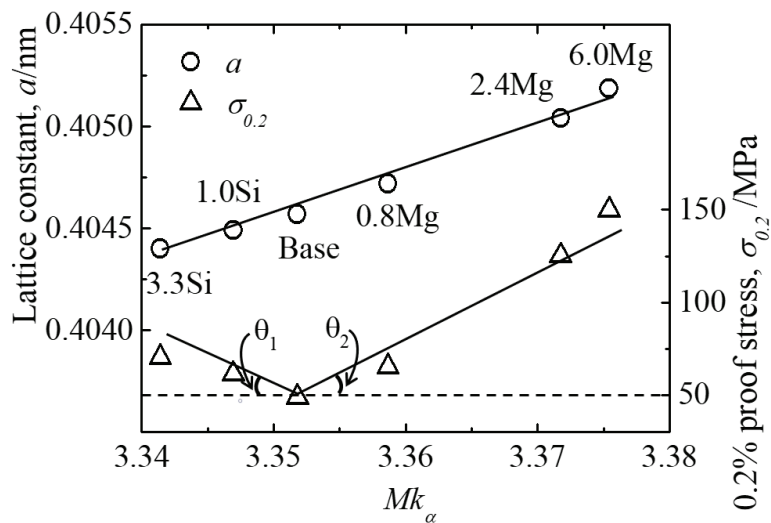


Fig. 2.12 Relationship between Mk_α values and the lattice constant, $\sigma_{0.2}$ of the Al-1.5Mn-xSi and Al-1.5Mn-xMg¹⁵⁾ alloys.

The addition of Mg and Si to the Al-1.5Mn alloy results in the replacement of Si or Mg in the α -Al phase and induces different types of lattice distortions. Figure 2.10 shows the relationship between Mk_α values and the lattice constant, $\sigma_{0.2}$ of the experimental and reference¹⁵⁾ alloys. The Al-1.5Mn-6.0Mg alloy was prepared as a reference for supersolution limit. It was clear that the constant lattice values of Mg and Si addition alloys have negative and positive increasing trends centered on Al-1.5Mn alloy, respectively. It was also found that there was a linear relationship between Mk_α values of the α -Al phase and the lattice constant in Al-1.5Mn-XSi/Mg alloys, regardless of the kinds of the third element.²⁸⁾ In addition, the $\sigma_{0.2}$ of the alloy increased compared with the Al-1.5Mn alloy with the change of Mk_α value. The increment rate of $\sigma_{0.2}$ represented by θ_1 and θ_2 was similar to that in Fig. 2.10. In addition, the relationship between the value of ΔMk_α and the amount of work hardening of the experimental and reference¹⁵⁾ alloys was also shown in Fig. 2.11. There was also a good linear relationship between ΔMk_α and the amount of working hardening in the alloys.

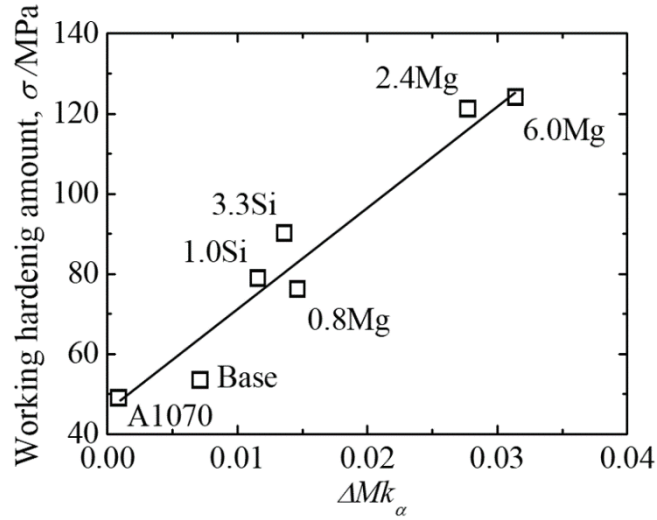


Fig. 2.13 Relationship between ΔMk_α values and working hardening amount of the experimental and reference¹⁵⁾ alloys.

The relationship between dislocation density and Mk_α of the Al-1.5Mn-XSi/Mg alloys is also shown in Fig. 2.12. There was a good relationship between dislocation density and Mk_α , regardless of the series of alloys.²⁸⁾ The Mg and Si had respectively low and high Mki values, or small and large atomic radii, or large and small electronegativity, as shown in Fig. 2.1. Elastic interactions were caused by the atomic size difference between the solute and solvent atoms. In contrast, charge transfer occurred based on the difference in electronegativity between solute and solvent atoms. The charge transfer between solute and solvent atoms may contribute to their binding strength. Compared with the Al-1.5Mn alloy, the dislocation density of the Si and Mg addition alloy increased proportionally to the value of Mk_α . In a single-parameter model of the flow stress curve, the proof stress (σ_p) depends only on the total dislocation density (ρ), which according to Eq. (2-6)^{41, 42)} is considered as a single internal variable of the material.

$$\sigma_p = aGb(\rho)^{1/2} \quad (2-6)$$

G is the shear modulus, a is a constant, and b is the Burger vector. It was considered according to the assumption in eq. (2-6) as evidence that the interaction between the $\sigma_{0.2}$ and dislocation density or dislocation migration barriers can be explained by the value

of Mk_α . This might indicate the level of solid solution strengthening using the Mk_α values of the ternary Al-1.5Mn-XSi/Mg alloys.

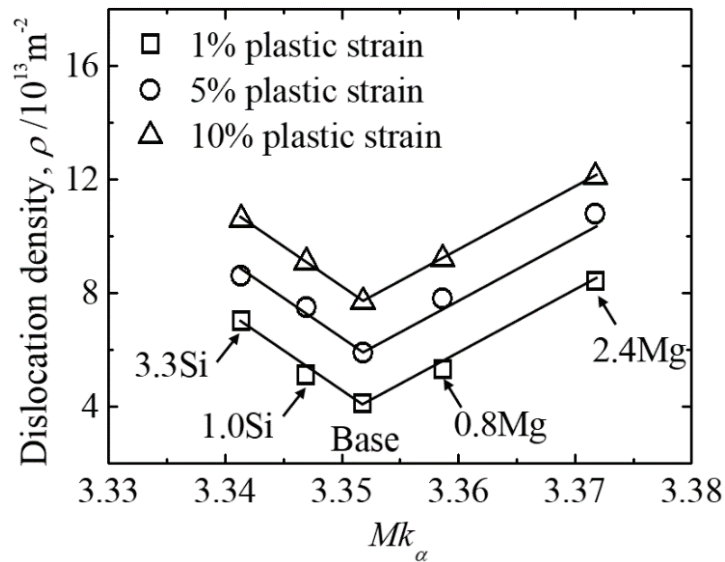


Fig. 2.14 Relationship between Mk_α values and dislocation density of the experimental and reference¹⁵⁾ alloys.

It can be considered that the variation trends of lattice constant, $\sigma_{0.2}$ and work hardening amount were mainly consistent with Mk_α or ΔMk_α , indicating solid solution strengthening at the α -Al phase level. In the tensile test procedure of this study, the influence of the difference in the mechanical properties of the third elements such as Mg and Si with higher and lower Mk_i values can be ignored. The $\sigma_{0.2}$ values of 1.0 and 3.3Si addition alloys with the Mk_i values of 3.346 and 3.331, respectively, can be predicted from the Mk_α value. Based on the relationship between $\sigma_{0.2}$ and Mk_α shown in Figure 2.10, it was considered necessary to reduce the value of Mk_α to 3.330 to achieve $\sigma_{0.2}$ of 135MPa. This $\sigma_{0.2}$ value was obtained in an as-cast suitability development for an Al-1.5Mn-2.4Mg alloy with an Mk_α value of 3.372. However, it was useless to add more than 3.3 Si to the alloy of this system, because it exceeded the solid solution limit of Si in the α -Al phase, and a brittle phase appears in the alloy, as shown in Fig. 2.3. It can be concluded that the application of Al-1.5Mn-Si alloys on automotive structural parts was tricky compared with Al-1.5Mn-Mg alloys because Al-1.5Mn-Mg alloys

2.5 Summary

- (1) The dendrite size of Al-1.5Mn alloy was 104.3 μm , and the 1.0, 3.3 Si addition for the Al-1.5Mn alloy was 98.7 μm and 43.1 μm , respectively. The reduction in dendrite size was mainly attributed to a great number of the formation of $\text{Al}_{12}\text{Mn}_3\text{Si}$ phase, which uniformly distributed in the dendrites and grain boundaries in the 3.3 mass% Si added alloy.
- (2) The DTA results showed that the formation of some α -Al matrix prefers to nucleate around the primary $\text{Al}_{12}\text{Mn}_3\text{Si}$ phase block and grew independently in the 3.3Si added alloy. The solidification sequence was consistent with the change of their microstructure.
- (3) The nano-hardness of Al-1.5Mn alloy with 0.0, 1.0 and 3.3 Si addition were 40.2, 61.3 and 69.7 MPa, respectively. Nano hardness increased continuously with an increase in the amount of Si which could contribute to the solid solution strengthening by Si.
- (4) The improvement of the ultimate tensile strength (σ_{UTS}) or yield strength ($\sigma_{0.2}$) was outstanding in 1.0 and 3.3 Si added alloy. And the tensile properties were roughly predicted by the values of ΔMk , an electron parameter which can be associated with the solid solubility. The solid solution strengthening strongly influenced the tensile properties, leading to an increase of both the yield strength ($\sigma_{0.2}$) and ultimate tensile strength (σ_{UTS}) in the 3.3 Si alloy by 42 % and 101%, respectively.
- (5) The proportion of $\text{Al}_{12}\text{Mn}_3\text{Si}$ phase with a smaller size ($<1 \mu\text{m}^2$) decrease from 42.8% to 39.6% when Si content increased from 1.0 to 3.3. The proportion of the coarser particles ($>10 \mu\text{m}^2$) was improved from 5.8% (1.0 Si) to 7.33% (3.3Si). The elongation decreased significantly in the 3.3 mass% Si added alloy due to the high-volume fraction of $\text{Al}_{12}\text{Mn}_3\text{Si}$ phase, which was the initiations of fracture.

References

- 1) Silvia Lombardo, Ildiko Peter, Mario Rosso: *Materialstoday: Proceedings* **10** (2019) 271-276.
- 2) Bo Lin, Rui Xu, Haoyu Li, Huaqiang Xiao, Weiwen Zhang, Shaobo Li: *Materials Characterization* **142** (2018) 389-397.
- 3) Radha Raman Mishra, Apurbba Kummar Sharma: *Materials & Design* **112** (2016) 97-106.
- 4) W. S Miller, L Zhuang, J Bottema, A. J Wittebrood, P De Smet, A Haszler, A Vierehhe: *Mater. Sci. Eng. A* **280** (2000) 37-49.
- 5) Antonio Rotella, Yves Nadot, Mickael Piellard, Remi Augustin, Michel Fleuriot: *International Journal of Fatigue* **114** (2020) 138554.
- 6) Zahra Zribi, Hassan Houcin Ktari, Frederic Herbst, Virgil Optasanu, Nabil Njah: *Materials Characterization* **153** (2019) 190-198.
- 7) H.A. Elhadari, H. A. Patel, D. L. Chen, W. Kasprzak: *Mater. Sci. Eng. A* **528** (2011) 8128-8138.
- 8) Huilan Huang, Yanheng Dong, Yuan Xing, Zhihong Jia, Qing Liu: *Journal of Alloys and Compounds* **765** (2018) 1253-1262.
- 9) Qingchuan Zou, Jinchuan jie, Tongmin Wang, Tingju Li: *Materials Letters* **185** (2016) 59-62.
- 10) RHEINFELDEN ALLOYS GmbH & Co. KG: *Primary aluminium Casting alloys* (2016) 37-40.
- 11) Mohammadreza Zamani, Hoda Dini, Ales Svoboda, Lars-Erik Lindgren, Salem Seifeddine, Nils-Eric Andersson, Anders E. W. Jarfors: *International Journal of Mechanical Science* **121** (2017) 164-170.
- 12) A. J. McAlister, J. L. Murray: *Journal of Phase Equilibria* **8** (1987) 438-447.
- 13) Zhen Li, Zhen Zhang, X. -Grant Chen: *Mater. Sci. Eng. A* **729** (2018) 196-207.
- 14) K. Liu, X. -Grant Chen: *Mater. Sci. Eng. A* **697** (2017) 141-148.

- 15) K. Matsugi, S. Yamamura, Z.F. Xu, Y.B. Choi, K. Sugio, G. Sasaki and N. Oda: *Mater. Trans.* **56** (2015) 1675-1682.
- 16) Y. J. Li, L. Arnberg: *Acta Materialia* **51** (2003) 3415-3428.
- 17) M. Morinaga, N. Yukawa and H. Adachi: *Tetsu-to-Hagane* **72** (1986) 555-562.
- 18) M. Morinaga, N. Yukawa: "Alloy Design Base on Molecular Orbital Method" *Computer Aided Innovation of New Materials*, Amsterdam (1991) 803-808.
- 19) M. Morinaga, S. Nasu, H. Adachi, J. Saito and N. Yukawa: *J. Phys. Condens. Matter* **3** (1991) 6817-6828.
- 20) M. Morinaga and S. Kamado: *Model. Simul. Mater. Sci. Eng.* **1** (1993) 151-164.
- 21) R. Ninomiya, H. Yukawa and M. Morinaga: *J. Japan Inst. Light Metals* **44** (1994) 171-177.
- 22) Meiqi Yu, Zhenfeng Xu, Yong Bum Choi, Takuma Konishi, Kazuhio Matsugi, Jinku Yu, Satoshi Motozuka, Kenichiro Suetsugu: *Mater. Trans.* **58** (2017) 140-147.
- 23) Meiqi Yu, Zhenfeng Xu, Yong Bum Choi, Takuma Konishi, Kazuhio Matsugi, Jinku Yu, Satoshi Motozuka, Kenichiro Suetsugu: *Mater. Trans.* **59** (2018) 303-310.
- 24) M. Morinaga, N. Yukawa, H. Adachi and H. Ezaki: *The Metallurgical Society of AIME, Warrendale (Superalloys 1984)* (1984) 523-532.
- 25) K. Matsugi, Y. Murata, M. Morinaga and N. Yukawa: *The Minerals, Metals and Materials Society, Warrendale (Superalloys 1992)* (1992) 307-316.
- 26) K. Matsugi, T. Endo, Y. B. Choi and G. Sasaki: *Mater. Trans.* **51** (2010) 740-748.
- 27) K. Matsugi, Y. Murata, M. Morinaga and N. Yukawa: *Mater. Sci. Eng. A* **172** (1993) 101-110.
- 28) Zeze Xiao, Kazuhiro Matsugi, Zhefeng Xu, Yongbum Choi, Kenjiro Sugio, Nobuyuki Oda and Jinku Yu: *Mater. Trans.* **61** (2020) 1355-1363.

- 29) M. Morinaga, Y. Murata and H. Ezaki: Material Chemistry in Nuclear Environment, Tsukuba (Proc. Int. Symp.) (1992) 241-252.
- 30) K. Matsugi, H. Mamiya, Y. B. Choi, G. Sasaki, O. Yanagisawa and H. Kuramoto: Int. J. Cast Metals Res. **21** (2008) 156-161.
- 31) M. Enomoto, H. Harada and H. Murakami: Tetsu-to-Hagane **80** (1994) 487-492.
- 32) I. Ansara, B. Sundman and P. Willemin: Acta Metall. **36** (1988) 977-982.
- 33) T. Koyama: J. Japan Inst. Metals **73** (2009) 891-905.
- 34) J. C. Slater, Phillips, James C: Physics Today **27** (1974) 49.
- 35) M. S. Turhal, T. Savaskan: Journal of Materials Science **38** (2003) 2639-2646.
- 36) W.C. Oliver, G.M: J. Mater. Res. **7** (1992) 1564-158.
- 37) H. Yoshinaga and H. Kurishita: J. Japan Inst. Light Metals **31** (1981) 359-368.
- 38) J. P. Hirth and J. Lothe: Theory of Dislocation, New York, (McGraw-Hill) (1968) 256-265.
- 39) W. G. Johnston: J. Appl. Phys. **33** (1962) 2716.
- 40) H. Suzuki: Introduction to Dislocation Theory, Tokyo (Agne Gijutsu Center Inc.) (1967) 294.
- 41) G. E. Totten, L. Xie and K. Funatani: Modeling and Simulation for Material Selection and Mechanical Design, New York Basel (Marcel Dekker, Inc.) (2004) 198-293.
- 42) O. Yanagisawa and F. Yoshida: Basic Materials Science, Tokyo (NJ, Kyoritsu Shuppan Co. Ltd.) (1994) 86-90.

Chapter 3

Effects of Mo and Zr addition on microstructure and mechanical properties of Al-9Si alloy

<u>3.1</u>	<u>Introduction</u>	55
<u>3.2</u>	<u>Electron parameter for the designation of the Al-9Si alloys</u>	56
<u>3.2.1</u>	<u>Electronic parameter representing alloying effects</u>	56
<u>3.2.2</u>	<u>Selection of experimentally alloys</u>	58
<u>3.3</u>	<u>Experimental procedures</u>	58
<u>3.3.1</u>	<u>Materials and manufacturing process</u>	58
<u>3.3.2</u>	<u>Evaluation of properties</u>	59
<u>3.4</u>	<u>Results and discussion</u>	62
<u>3.4.1</u>	<u>Microstructures</u>	63
<u>3.4.2</u>	<u>Solidification behaviors</u>	65
<u>3.4.3</u>	<u>Tensile behaviors</u>	70
<u>3.4.4</u>	<u>Nanoindentation behaviors in the α-Al phases</u>	73
<u>3.4.5</u>	<u>TEM observation for the solidification process</u>	75
<u>3.4.6</u>	<u>As-cast application possibility of the 0.2Mo+0.2Zr alloy</u>	79

<u>3.5</u> <u>Summary</u>	80
<u>References</u>	82

Introduction

Aluminium alloys are widely used in the automotive industry due to their productivity and high degree of shape freedom¹⁻⁴). Modern aluminium alloys need to meet continuously increasing mechanical performance requirements and basic requirements for functional reliability. The widely used die-casting aluminium-silicon alloy is superior to other alloys in the fluidity of molten metal, which is an important property in the die-casting process⁵). Most Al-Si alloys must be heat-treated after solidification to achieve the purpose of the alloy strengthening⁶). In light of reducing the production cost, applying the Al alloys in as-cast conditions has attracted great attention in recent years.⁷⁻⁹) For example, the Silafont-30 (Al-9mass%SiMg) showed the 0.2% proof stress ($\sigma_{0.2}$) of 90-150MPa, ultimate tensile strength (σ_{UTS}) of 180-240MPa and the fracture strain (ϵ_f) of 2-9% in the as-cast condition.⁷) The alloy compositions are referred to in mass % unless otherwise noted`. And this alloy has been applied to the automobile parts, such as cylinder heads for compressors, compressor housing, and intermediate flange for SF₆ switch system.⁷)

Conventional methods using phase diagrams for alloy design require much experimentation, labor, and cost, so we performed theoretical development using electronic parameters derived Al-9Si on electronic structure calculations. The d-electron concept proposed by Morinaga et al.^{10, 11}) based on theoretical calculation of electronic structure has been applied to the design of high-performance alloys such as Al¹²⁻¹⁷), Bi¹⁸), Ni¹⁹⁻²²) and Ti²³⁻²⁶), this Concept successfully predicts some physical or chemical properties of the designed alloy.¹³) The bond order (*Bo*), which is a measure of the strength of the covalent bond between atoms and the d-orbital level of the transitional alloying element (*Md*), which is related to charge transfer have been used in d-electron concept¹⁸). *Md* is also found to be related to the electronegativity and atomic radius of the element.¹³) Electronegativity and atomic radius are both classical parameters used to describe the nature of chemical bonds between the atoms in the solids.¹⁵) For Al alloys with s, p simple metal, the ΔMk values are defined by taking the compositional averages of s-orbital energy level as described in later, which is easy to use in practical application compared to other alloy design methods.^{27,28})

In this study, the Al-9Si-0.3Fe-0.15Mn alloy was chosen as the base alloy, and 0.2Mo and 0.2Zr were added in combination (0.2Mo+0.2Zr) to the Al-9Si alloy to maintain the ductility and improve the strength in tensile properties. Their alloying effects on the solidified microstructures, solidification paths, and tensile properties were investigated in detail for developing low-cost alloys as the as-cast applications.³⁷⁾

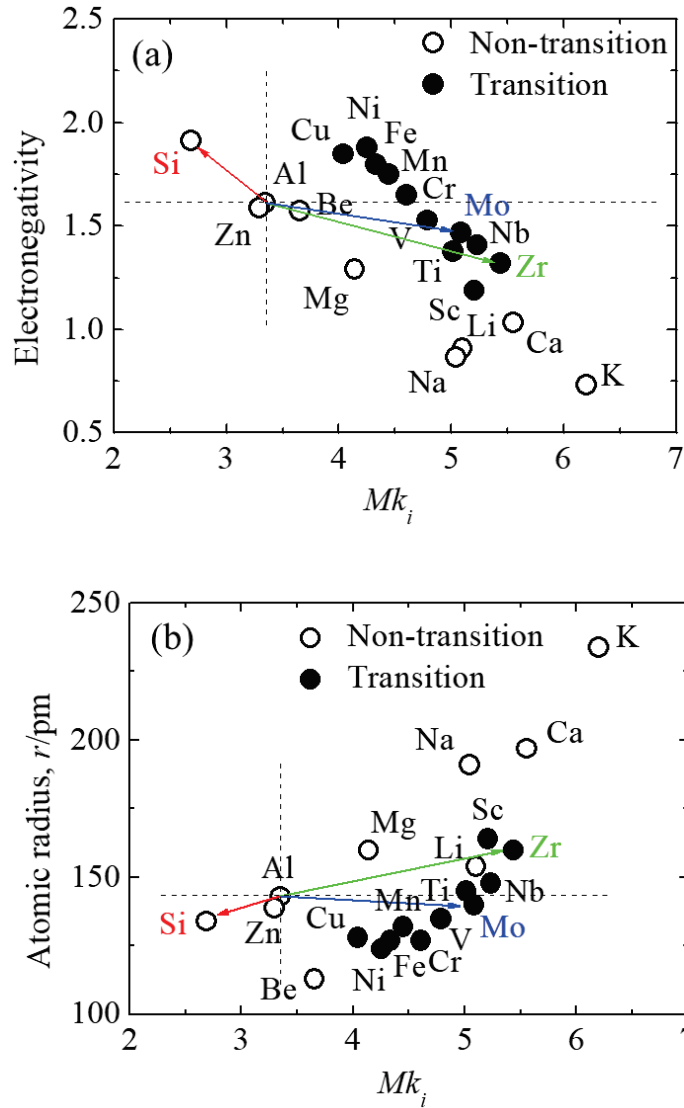


Fig. 3.1 Mk_i value of each alloying element in Al and the relations between Mk_i value and the (a) electronegativity and (b) atomic radius. (○ Non-transition, ● Transition element).

3.1 Electron parameter for the designation of the Al-9Si-Zr/Mo alloys

3.2.1 An electronic parameter representing alloying effects

The electronic parameter Mk_i for the optimization of the aluminum alloy composition is obtained from the electronic method of alloy design.¹²⁻¹⁷⁾ Mk_i is the s-orbital energy level existing above the Fermi level of the iAl18 cluster, containing the alloying element i and its surrounding aluminum atoms.¹⁵⁾ Various parameters have been proposed to describe the alloying behavior. Nevertheless, the electronegativity and atomic radius of the elements are chosen here because they represent the properties of the chemical bonds between atoms in solids.¹⁵⁾ There is a good correlation between the electronegativity or atomic radius and the Md parameter of the d-orbital energy level for transition metals, as described in Section 1. For s,p simple metals like Al, d orbital levels are no longer valid in transition metal-Al-9Sid alloys. Mk_i , the s-orbital energy level excited above the Fermi level, is obtained by discrete variational $X\alpha^{30)}$ (DV- $X\alpha$) cluster calculations. Therefore, alloying effects are inevitably involved in Mk_i .¹⁵⁾ It is well known that the energy levels obtained by DV- $X\alpha$ cluster calculations represent the electronegativity itself.^{14, 15)} The Mk_i value decreases with increasing electronegativity and increases with increasing atomic radius of the element.^{14, 15)} Furthermore, p-orbital energy levels can be considered instead of s-orbital energy levels. Nonetheless, spherically symmetric s orbitals may be better than oriented p orbitals for studying the mechanical properties of aluminum alloys.¹⁵⁾

Except for Si, Zn, Ga, and Ge, most elements have Mk_i value higher than Al. For alloys, the two mean values of the s-orbital energy levels, Mk_t and ΔMk , are defined by taking compositional averages using the equation (3-1) and (3-2).

$$Mk_t = \sum x_i Mk_i \quad (3-1)$$

$$\Delta Mk = \sum x_i |Mk_i - Mk_m| \quad (3-2)$$

Where x_i is the mole fraction of component i in the alloy, Mk_i and Mk_m are the Mk value of component i and Al, respectively. When all elements in the alloy have Mk_i value above or below Al, two averages differ only by a constant deviation of 3.344 from the

Mkm value; therefore, there is no essential difference between them. But when the elements with higher and lower Mk_i values are mixed in the alloy, the meaning of the two average values is different.¹⁵⁾

3.2.2 Selection of experimentally alloys

In this chapter, the choice of Si as the second element will also focus on describing the Mki value, as can be seen from the equation (4-2), when the alloying element has a more significant Mki value, the alloying effect decreases. Si, whose Mki value is smaller than Al, is suitable as an additive element. However, the addition of Si with an Mki value smaller than that of Al induces tensile strain in the Al lattice. It is necessary to add elements with significantly higher Mki values than Al to maintain the stability of the lattice. Both Mo and Zr have significantly more Mki values than Al¹⁵⁾. In addition, the atomic radii of Mo and Zr are close to those of Al. Iron is one of the most detrimental impurities in aluminum alloys because it forms brittle and complex needle-like intermetallic compounds that significantly affect the mechanical properties³¹⁾. Manganese, the most common alloying element, inhibits the formation of needle-like particles by promoting the formation of thermodynamically stable α -Al_{31, 32}). In general, Fe:Mn ratios below 2 are recommended for alloying to promote α -Al precipitation 31, 33). The addition amount of 9Si, 0.2Mo, and 0.2Zr is the upper limit of the component content in the Castasil-37 alloy⁷⁾.

3.2 Experimental procedures

3.3.1 Materials and manufacturing process

The pure Al, Al-Si, Al-Mn, Al-Zr, and Al-Mo master alloys were used for preparing experimental alloys. To avoid masking effects or interactions with additional elements, neither Sr nor Na was added as modifier agents. In the production of ingots, they should be produced by the die-casting method according to the purpose of this research.

However, a low-cost gravity casting method was adopted to use ingots of simple shapes that do not require high precision. The melting temperatures were kept at 990-1007K. Then, the melt was poured into a steel mold preheated at 426-488K. The size of the ingots was 195mm × 23mm × 39mm.

3.3.2 Evaluation of properties

Samples for microstructural observation were taken from half the length, width and height of each ingot. Microstructural observations of the samples were performed using an optical microscope (OM) equipped with a wavelength-dispersive X-ray spectrometer (WDS) and an electron probe microanalyzer (EPMA). Image-pro software was used to measure the volume fraction of dendrite (DA) area and interdendritic (ID) area, as well as the secondary dendrite arm spacing (SDAS) of the experimental alloys. Use at least 15 OM images to calculate the average volume fraction of DA and ID. SDAS is measured by using OM images with precise scale bars. The line-intercept method³⁴⁾ was used to measure SDAS, and at least 100 dendrites were taken to determine SDAS. Differential thermal analysis (DTA) with a heating-cooling rate of 5K min⁻¹ was used to study the solidification behavior. Thermal effects on liquidus temperature and exothermic cooling curves were also measured. Each test was repeated at least twice to ensure the reproducibility of the detected temperature. The solidification path was measured at 50μm intervals from DA to ID using mass% point analysis. Analysis points Analysis results are plotted on a 25-point triangular coordinate map, which was represented as a solidification path.

The two-dimensional local number (LN2D) is defined as the barycentric number³⁵⁾ of the second-phase particles in the measurement circle. When the particles are arranged uniformly and randomly in two dimensions, the relative frequency distribution of LN2D presents a modified Poisson distribution for any point field, and the probability of LN2D is expressed as

$$P(LN2D=k+1)=\frac{\gamma^k}{k!} \exp(-\gamma) \quad k=0, 1, 2 \dots \quad (3-3)$$

The mean and variance of this expected distribution are both 7. On Al-9Si defined by this center of gravity, the local number 7 corresponds to the number density of all particles when the space is uniformly distributed randomly. The mean of LN2D (LN2Dav) and the variance of LN2D (LN2Dvar) were used to assess the randomness of the spatial distribution of intermetallic compounds (IMCs).

Tensile test specimens with a diameter of 6 mm and a gauge length of 80 mm were machined from steel ingots. Tensile tests were performed using a testing machine (DCS-R-5000, SHIMADZU, Japan) at 293K with an initial strain rate of 1.0 mm min⁻¹. Tensile strain up to necking was accurately measured by using an extensometer. Four tensile tests were carried out for each alloy, choosing a moderate tensile curve. After the tensile test, the fracture was observed using a scanning electron microscope to interpret the deformation characteristics of the alloy. Young's modulus (*E*) in tensile testing was determined by measuring the stress-strain slope in the tensile curve at strains less than 0.2%. The Lankford value (*r*) was determined by measuring the width and length dimensions of the specimen over the gauge length before and after tensile deformation and was calculated as follows:

$$r = \ln(b/b_0) / \ln(b_0 l_0 / b l) \quad (3-4)$$

Where *l*₀ and *b*₀ are the length and width dimensions of the specimen before the tensile deformation. *l* and *b* are the length and width dimensions of the specimen after the tensile deformation.

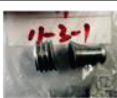








Specimen	Base (As-cast, 11-3-1) 		Mo+Zr (As-cast, 14-3-1) 	
	Before	2.708 mm 	2.654 mm 	2.816 mm 
After	2.681 mm 	2.521 mm 	2.788 mm 	2.900 mm 
	1%	5%	1%	5%

Fig. 3.2 Experimental results for 1% and 5% cold rolling of Al-9Si and 0.2Mo+0.2Zr addition alloy specimens.

To reveal the mechanism of ductile deformation, Al-9Si and 0.2Mo+0.2Zr addition alloy specimens were subjected to 1% plastic strain by cold rolling and examined by transmission electron microscopy (TEM, JEM-2010, JEOL, Japan). Dislocation densities were also measured by the equal-thickness fringe method using regions in TEM samples with a thickness greater than 100 nm. Figure 3.2 shows the results for 1% and 5% cold rolled alloy samples with Al-9Si and 0.2Mo+0.2Zr additions.

Nanoindentation experiments were performed on the primary and eutectic α -Al phases of Al-9Si and 0.2Mo+0.2Zr addition alloys by an instrument (ENT-1100a, Elionix, Japan) at room temperature using a Berkovich diamond indenter. Measurements were performed at a hold load (load control) of 3mN, loaded within 30 s, held at peak load for 20 s, and unloaded for each sample within 30 s. Nanoindentation hardness (H_{IT}) was calculated using the Oliver-Pharr method³⁶⁾ as shown in Eq. (3-5) and (3-6) respectively according to the load-depth curve.

$$H_{IT}=P_{max}/A_p \quad (3-5)$$

$$A_p=23.46 \times h_c^2 \quad (3-6)$$

Where H_{IT} is the nanoindentation hardness of the α -Al phase, P_{max} is the maximum indentation load, A_p is the projected area of the indentation, and h_c is the depth of indentation.

3.3 Results and discussion

3.4.1 Microstructures

The OM images of the experimental alloys in the as-cast conditions are presented in Fig. 3.3. The general features of the alloys were the dendrite arm (DA) areas, which were composed of the primary α -Al phase with dendrite features and the inter-dendritic

(ID) areas, which consisted of the eutectic α -Al phase and eutectic Si particles with inter-dendrite features in the alloys.³⁷⁾ The principal change brought to the microstructure by 0.2Mo, and 0.2Zr addition was the volume fraction of the ID areas. Compared with other alloys, the 0.2Zr+0.2Mo addition alloy showed the highest volume fraction in the ID areas, which was 77.3%. It was also found that the secondary dendrite arm spacings (SDAS) in the base, 0.2Mo, 0.2Zr, and 0.2Zr+0.2Mo addition alloys were 41.2, 37.7, 35.4, and 33.6 μ m, respectively. The volume fraction of the ID areas and the area ratio between the DA and ID were summarized in Table 3.1. The area ratio between the DA and ID of the base, 0.2Mo, 0.2Zr, and 0.2Zr+0.2Mo addition alloys was 1: 2.0, 1: 2.2, 1: 2.5, and 1: 2.6, respectively. The results indicated that 0.2Mo or 0.2Zr plays a significant role in refining primary α -Al, and 0.2Zr is a more significant refining effect than 0.2Mo. While the 0.2Mo and 0.2Zr combined additions to the base alloy could lead to better refinement than the 0.2Mo and 0.2Zr added alone.

Table 3.1 Volume fraction of the ID areas and area ratio of the DA and ID.

Experimental alloys(mass%)	$\Delta M k_{total}$ (10^{-3} eV)	Volume fraction(%)		Area ratio	SDAS (μ m)
		DA	ID	DA:ID	
Al-9Si-0.3Fe-0.15Mn (Base)	60.0	33.3	66.7	1:2.0	41.2
Al-9Si-0.3Fe-0.15Mn-0.2Mo+0.2Zr (0.2Mo+0.2Zr)	62.4	27.8	72.2	1:2.6	33.6

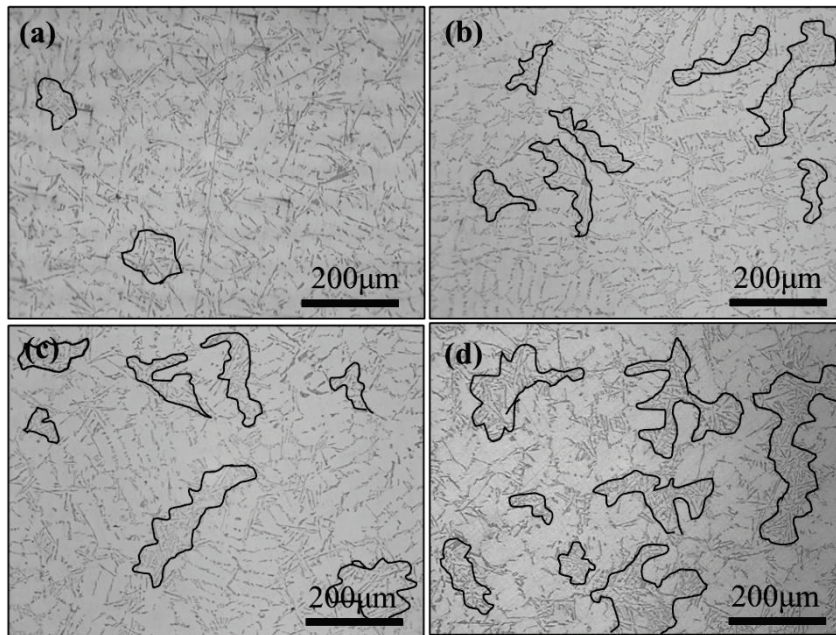


Fig.3.3 OM images of the (a) Al-9Si, (b) 0.2Mo, (c) 0.2Zr, and 0.2Mo+0.2Zr addition alloys in the as-cast conditions.

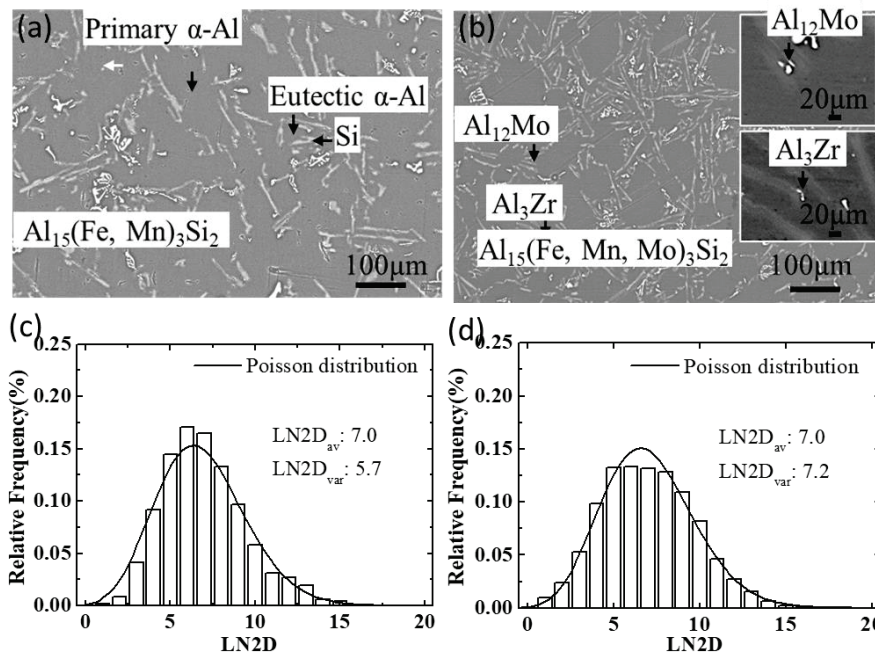


Fig. 3.4 BSE image of the (a) base and (b) 0.2Mo+0.2Zr addition alloys, and (c) and (d) distribution results of (a) and (b), respectively.

Figure 3.4(a) and (b) show the IMCs morphology of Al-9Si and 0.2Mo+0.2Zr addition alloys in the as-cast conditions by EPMA characterization. Table 3.2 presents representative chemical compositions of the studied phases as determined by WDS. The $\text{Al}_{15}(\text{Fe}, \text{Mn})_3\text{Si}_2$ exhibited a "Chinese-script" morphology³⁷⁾ with a volume fraction of 2.4% obtained in the Al-9Si alloy. The 0.2Mo+0.2Zr addition alloy showed the $\text{Al}_{15}(\text{Fe}, \text{Mn}, \text{Mo})_3\text{Si}_2$ with "Chinese-script" morphology³⁷⁾, Al_{12}Mo , and Al_3Zr as shown in Fig.3.4(b). The Al_{12}Mo and Al_3Zr with an average size of $0.3\mu\text{m}$ were observed in or near the Si phase, and Al_{12}Mo and Al_3Zr served as nucleation sites for eutectic Si and reduced the size of eutectic Si with an average thickness of $2.1\mu\text{m}$.³⁷⁾ The addition of 0.2Mo+0.2Zr alloy with the Al_{12}Mo and Al_3Zr results in an ID volume fraction of 72.2% with fine Si particles, which was higher than 66.7% in the Al-9Si alloy. The size of $\text{Al}_{15}(\text{Fe}, \text{Mn}, \text{Mo})_3\text{Si}_2$ in the 0.2Mo+0.2Zr addition alloy was small and the volume fraction was large, as shown in Table 3.2, as shown in Table 3.2. The LN2D results of distribution of IMCs for the Al-9Si and 0.2Mo+0.2Zr addition alloys are shown in Fig.3.4(c) and (d), respectively. The Poisson distribution was calculated to show the distribution condition. Poisson distribution is a discrete random distribution, which is the probability of occurrence when the number of particles in the measurement circle is n (n is a constant value). Randomly distributed particles are consistent when there are enough measuring circles (10^6 in this test). Variance is a Poisson distribution parameter that describes how far a variable is from its expected value. In the definition of LN2D, a uniform random distribution has a variance of 7.0. If the variance of the experiment is less than 7.0, the particles are ordered (or perfectly ordered if the variance is 0). Conversely, if the variance exceeds 7.0, the particles are clustered. The Al-9Si and 0.2Mo+0.2Zr addition alloy showed the same level of LN2D_{av} with 7.0 and the LN2D_{var} with 5.7 and 7.2, respectively.³⁷⁾ The Al-9Si alloy exhibited a small LN2D_{var} , probably due to the larger mean size of the $\text{Al}_{15}(\text{Fe}, \text{Mn})_3\text{Si}_2$, about $29.8\mu\text{m}$, which had some volume in overlapping. The distribution of IMCs in 0.2Mo+0.2Zr addition alloy with a smaller mean size of $11.4\mu\text{m}$ than base alloy was close to Poisson distribution, which was the theoretical probability distribution for a uniform random arrangement. The

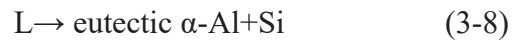
0.2Mo+0.2Zr addition alloy had $LN2D_{var}$ greater than 7.0 for a random point filed predicted by eq. (3-3), that is, the smaller $Al_{15}(Fe, Mn, Mo)_3Si_2$, Al_3Zr , and $Al_{12}Mo$ with in the 0.2Mo+0.2Zr addition alloy were clustered in or near the eutectic grains.³⁷⁾

Table 3.2 Chemical compositions and the volume fraction of the Al-9Si and 0.2Mo+0.2Zr addition alloys.

Alloys	Composition(mol%)						Phase formula	Volume fraction(%)	Size (μm)
	Al	Si	Fe	Mn	Mo	Zr			
Base (mol% ratio)	72.6 (15)	10.8 (2)	12.5 ()	4.1 (3)			$Al_{15}(Fe, Mn)_3Si_2$	2.4	29.8
	73.1 (15)	11.2 (2)	10.5 ()	3.7 ()	1.5 (3)		$Al_{15}(Fe, Mn, Mo)_3Si_2$	2.8	19.4
0.2Mo+0.2Zr (mol% ratio)	57.6 (3)	19.8				22.6 (1)	Al_3Zr	0.3	0.3
	26.7 (12)	56.9	10.1	4.2	2.1 (1)		$Al_{12}Mo$	0.4	0.3

3.4.2 Solidification behaviors

Typical DTA heating and cooling curves obtained from the Al-9Si and 0.2Mo+0.2Zr addition alloys are shown in Fig. 3.4. The main peak A showing the liquidus temperature (T_A) of the Al-9Si alloy was the main crystal reaction (3-7), which occurred at 864K. Then, the eutectic reaction (3-8) occurred in T_B at 844K. The reaction of (3-9) at T_C of 841K appeared to be involved the eutectic reaction peak in the DTA curves.



Instead, peak A was considered to be generated by the mixed exothermic reaction of crystallization of Al_3Zr , $Al_{12}Mo$, and α -Al crystallization, and both of which were formed before the crystallization of the primary α -Al phase in the 0.2Mo+0.2Zr addition alloy. The DTA curves revealed a clear trend in which the T_A shifted to around 20K due to the formation of the Al_3Zr and $Al_{12}Mo$ in the 0.2Mo+0.2Zr addition alloy. There were

different peaks, showing downward and upward convex shapes in the Al-9Si and 0.2Mo+0.2Zr addition alloy, respectively, at a temperature between T_A and T_B . In addition, the thermal effect was calculated based on the area of the peaks. It was found that the ratio of the thermal effect between the primary peak A and eutectic peak B of each alloy was consistent with the area ratio between the DA and ID, as shown in Fig.3.3 and Table 3.1.

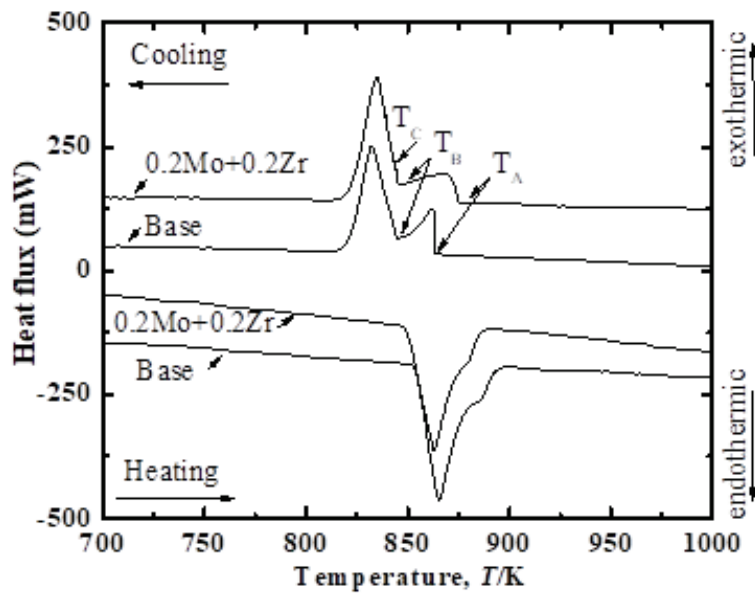


Fig. 3.4 Typical DTA curves obtained from the experimental alloys.

The solidification paths showed the changes of element composition from DA to ID after solidification. The solidification paths of the Al-9Si and 0.2Mo+0.2Zr addition alloys are shown in Fig. 3.4. Due to non-equilibrium solidification, the composition deviates from the average composition, resulting in a concentrated area where the element is added during solidification. The $Al_{12}Mo$ and Al_3Zr phases were formed in the 0.2Mo+0.2Zr addition alloy, followed by the crystallization of the primary α -Al phase, as shown from position ① to ② in Fig.3.5(c). While the primary α -Al phase crystallized first in the Al-9Si alloy with no concentration regions of the added elements, as shown from position ① to ② in Fig. 3.5(a). The eutectic reaction of the Si and α -Al phase had a lower concentration of solute elements than that of the primary α -Al phase which was caused by the repetition of the non-isothermal form in the eutectic due to the

redistribution of solute elements as shown by position ② and ③ in the Al-9Si and 0.2Mo+0.2Zr addition alloys, respectively. The primary and eutectic α -Al phase components of Al-9Si and 0.2Mo+0.2Zr addition alloys are shown as enlarged portions of (a) and (c) in Figures 3.5 (b) and (d), respectively.

The average component of α -Al phase in 0.2Mo+0.2Zr alloy was 97.7Al-0.54Si-0.08Fe-0.10Mn-0.09Mo-0.13Zr and its $\Delta M k_{p\alpha}$ was 5.4eV. It was higher than that of Al-9Si alloy with average component of 98.3Al-0.62Si-0.05Fe-0.11Mn, as shown in Fig.3.5(b)and (d), which was caused by Mo and Zr atoms in the solid solution. However, the eutectic α -Al phase of 99.1Al-0.33Si-0.04Fe-0.04Mn-0.2Mo-0.1Zr with $\Delta M k_{e\alpha}$ was 4.1eV, while $\Delta M k_{p\alpha}$ was 5.4eV. This is the solute diffusion caused by the diffusion mode during non-isothermal solidification of the alloy with the 0.2Mo+0.2Zr addition. In addition, the formation of $\text{Al}_{15}(\text{Fe}, \text{Mn})_3\text{Si}_2$ and $\text{Al}_{15}(\text{Fe}, \text{Mn}, \text{Mo})_3\text{Si}_2$ were finally formed, as shown in position ③ and ④ in the Al-9Si and 0.2Mo+0.2Zr addition of alloys, respectively. The solidification paths was also consistent with the DTA results, as shown in Fig. 3.3.

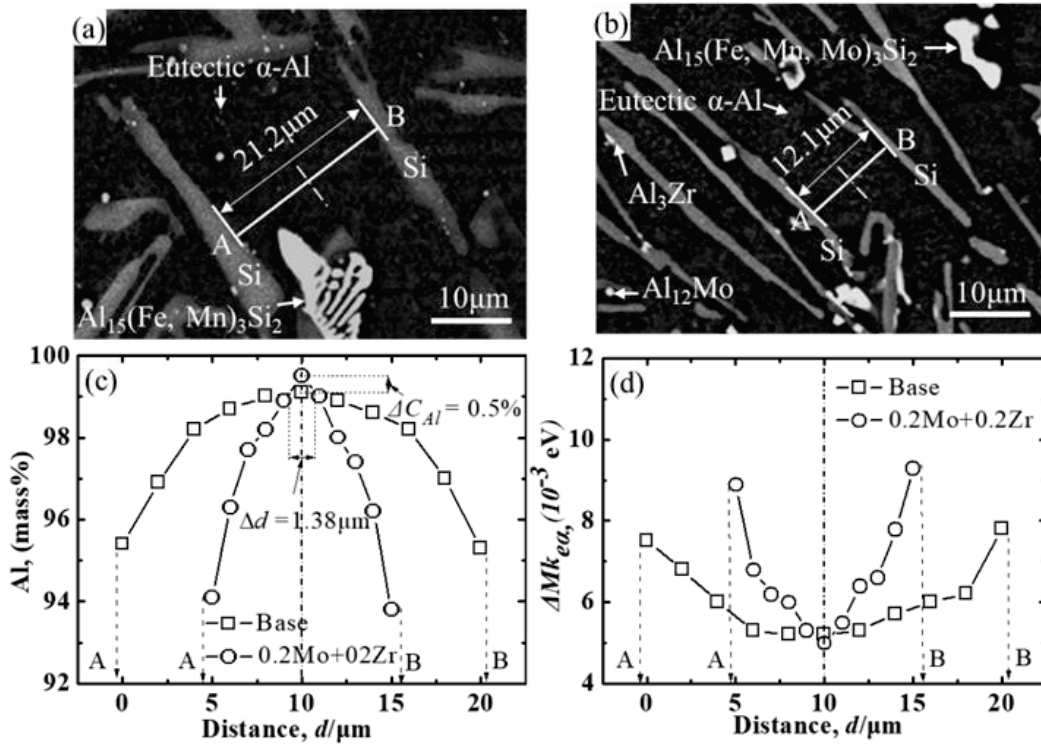


Fig.3.6 The BSE images of (a) Al-9Si and (b) 0.2Mo+0.2Zr addition alloys in as-cast condition and (c) the Al content and (d) $\Delta M k_{ea}$ of the Al-9Si and 0.2Mo+0.2Zr addition alloys.

The chemical composition analysis of the eutectic α -Al phase of the Al-9Si and 0.2Mo+0.2Zr addition alloys is shown in Fig. 3.6. The 0.2Mo+0.2Zr addition alloy obtained a refined Si phase with an average thickness of 2.1 μm , while the Al-9Si alloy was 4.6 μm . Chemical composition analysis of Al-9Si and 0.2Mo+0.2Zr addition alloys were selected as a eutectic α -Al phase between two adjacent Si phases, as shown in the BSE image. The direction of elemental analysis was from points A to B, and the elemental analysis results were calculated into the $\Delta M k_{ea}$, using the eq. (3-2) to show the indication of the solid solution strengthening eutectic α -Al phase level. The results of the Al content and $\Delta M k_{ea}$ in the Al-9Si and 0.2Mo+0.2Zr addition alloys are shown in Fig. 3.6 (c) and (d), respectively. The $\Delta M k_{ea}$ values of the alloys had a similar variation trend, being high close to the Si phase and low far away from the Si phase, which reflected the different levels of solid solution strengthening in the eutectic α -Al phase. The central region with Al content up to 99.6% in the 0.2Mo+0.2Zr addition alloy,

compared with 99.1% in the Al-9Si alloy. Furthermore, the 0.2Mo+0.2Zr addition alloy exhibited a higher $\Delta Mke\alpha$ than the Al-9Si alloy due to the solid solution of Mo and Zr atoms. The area with high Al content has fewer solid-solution atoms, and the value of $\Delta Mke\alpha$ was lower. The variation of $\Delta Mke\alpha$ in 0.2Mo+0.2Zr addition alloys indicated that Mo and Zr atoms with a non-isothermal system redistribute or micro-segregate in the eutectic α -Al phase during solidification^{34, 37}.

3.4.3 Tensile behaviors

The nominal tensile stress-strain curves at 293K for the experimental alloys in the as-cast conditions are shown in Fig. 3.7, and the characterization of tensile properties of the experimental alloys is shown in Table 3.3. The $\sigma_{0.2}$, σ_{UTS} , and ε_f of the Al-9Si alloy were 76MPa, 145MPa, and 6.1%, respectively. The 0.2Mo+0.2Zr addition alloy showed tensile properties with the $\sigma_{0.2}$ of 89MPa, σ_{UTS} of 160MPa, and ε_f of 7.1%. The 0.2Mo+0.2Zr addition alloy showed an increment in the σ_{UTS} and ε_f by 8% and 14%, respectively, compared to the Al-9Si alloy. The solid solution strengthening effect (ΔMk : 60.0eV in the Al-9Si and 62.4eV in the 0.2Mo+0.2Zr addition alloys) caused by the addition of 0.2Mo+0.2Zr increased Young's modulus (E) of the alloy from 73GPa of the Al-9Si alloy to 76GPa. Microstructural features might primarily affect other behaviours in the S-S curve. The work hardening coefficient calculated by the true S-S curve of the 0.2Mo+0.2Zr alloy was 0.3, which was greater than 0.2 of the Al-9Si alloy, indicating that the 0.2Mo+0.2Zr alloy had good uniform deep drawing deformation ability and was affected by Al₃Zr and Al₁₂Mo uniformly distributed eutectic domains arise, as described later in Section 4.5. Adding 0.2Mo+0.2Zr alloy had an r value 0.1 larger than that of Al-9Si alloy, which had good deep drawing deformation ability. In addition, the 0.2Mo+0.2Zr addition alloy exhibited a higher work hardening rate and work hardening amount than the Al-9Si alloy at the same strain rate at 293K. This may be related to the formation of small-sized eutectic α -Al phases and the extent of solution hardening during solidification, which will be discussed in a later section. It is found that the

0.2Mo+0.2Zr addition alloy showed an improvement in flow stress and ϵ_f even at the as-cast conditions because of solid solution strengthening and microstructural control.³⁷⁾

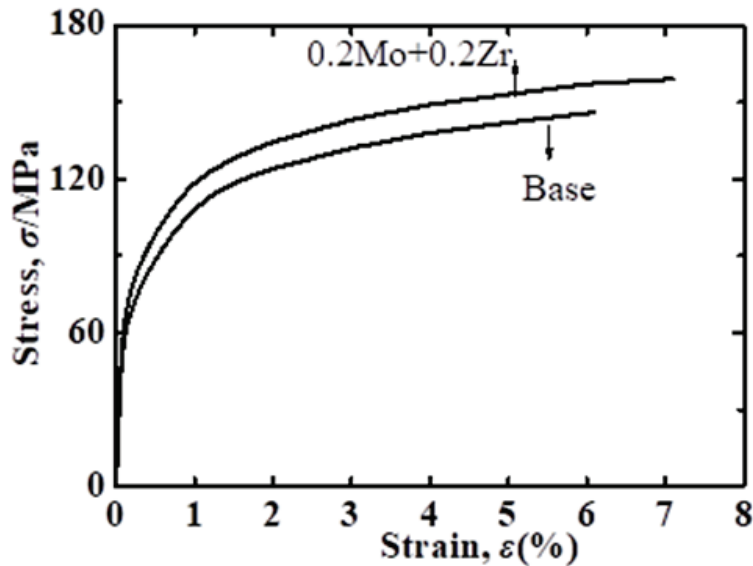


Fig.3.7 The nominal tensile stress-strain curves of the experimental alloys in the as-cast condition.

Fracture longitudinal sections of Al-9Si and 0.2Mo+0.2Zr addition alloys are shown in Figure 3.8. The fracture surface of Al-9Si alloy was relatively flat with Al-Si. In contrast, the fracture surface of 0.2Mo+0.2Zr addition alloy had more obvious Al-Al interface undulation and irregularity. High-magnification longitudinal cross-sections of the fracture surfaces of Al-9Si and 0.2Mo+0.2Zr addition alloys are shown in Fig. 3.8(b) and (d), respectively. Fractured eutectic Al-Si interfaces could be observed in Al-9Si alloys. Due to the smaller size of Si, it was not evident in the 0.2Mo+0.2Zr addition alloy. However, the longitudinal section of the 0.2Mo+0.2Zr addition alloy exhibited plastic fracture in the eutectic α -Al phase. It was believed that the high Al or low solute element regions in the eutectic α -Al phase acted as a continuous phase in the alloy, resulting in increased ductility and strength due to severe micro segregation.³⁷⁾

Table 3.3 The characterization of tensile properties of the Al-9Si and 0.2Mo+0.2Zr addition alloys.

Alloys	Young's modulus, E/GPa	0.2% proof stress, $\sigma_{0.2}/\text{MPa}$	Ultimate tensile strength, σ_{UTS}/MPa	Fracture strain, $\epsilon_f(\%)$	Working hardening coefficient, n	Work hardening rate, $\frac{d\sigma}{d\epsilon}/\text{MPa}$	Work hardening amount, $\Delta\sigma/\text{MPa}$	Lankford value, $r(\%)$
Base	73	76	145	6.1	0.2	14.9	69	0.6
0.2Mo+0.2Zr	76	89	160	7.1	0.3	16.7	73	0.7

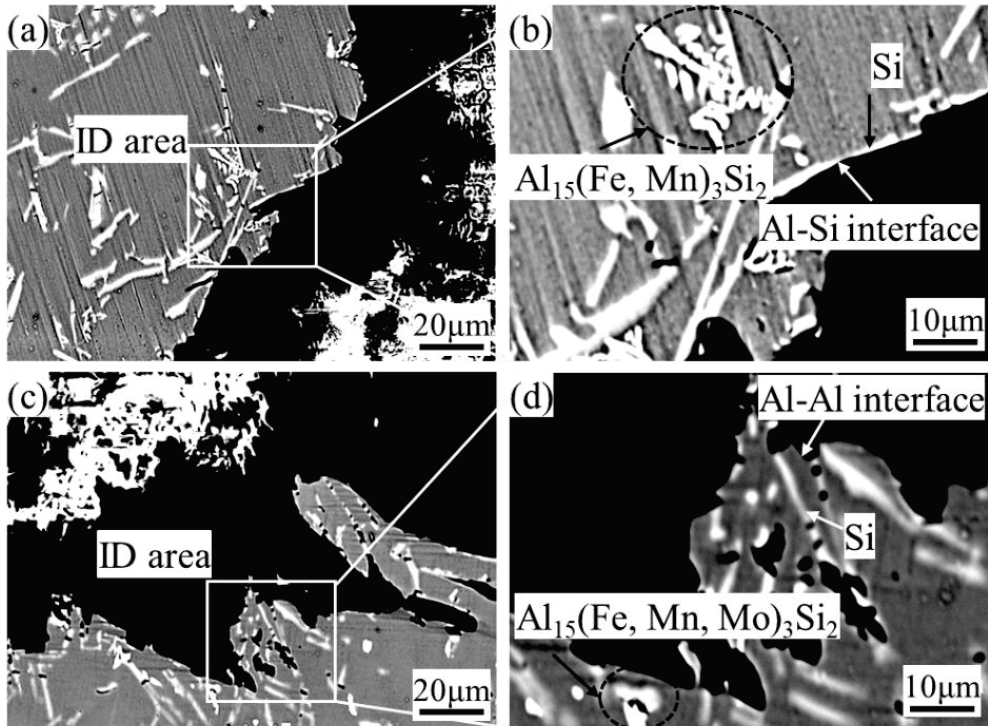


Fig.3.8 The fractured longitudinal sections of the (a) Al-9Si and (c) 0.2Mo+0.2Zr addition alloys in the as-cast conditions. The high-magnification longitudinal cross-section of the fracture surface of the ID area in the (a) Al-9Si and (c) 0.2Mo+0.2Zr addition alloys are shown in (b) and (d), respectively.

3.4.4 Nanoindentation behaviors in the α -Al phases

To clarify that the mechanical properties of the alloys were related to the α -Al phase in eutectic as the continuous phase, the nanoindentation measurements were performed on the primary and eutectic α -Al phases in Al-9Si and 0.2Mo+0.2Zr addition alloys.³⁷⁾ Figure 3.9 shows a typical load (P) -depth (h) curves obtained from the nanoindentation experiments. The primary α -Al phase in the alloy with 0.2Mo+0.2Zr addition showed a lower depth than the Al-9Si alloy at the constant load. As shown in Fig. 3.10, the degree of solid solution strengthening of the primary α -Al phase in the 0.2Mo+0.2Zr addition alloy was higher and the value of $\Delta Mkp\alpha$ was higher, which led to higher H_{IT} and E values. The H_{IT} and E of the primary α -Al phase in the Al-9Si and 0.2Mo+0.2Zr addition alloys were 825MPa and 67GPa, and 901MPa and 71GPa, respectively.³⁷⁾ The nanoindentation measurements were performed on the eutectic α -Al phase between two adjacent eutectic Si phases, as shown in Fig. 3.10. The minimum value of the H_{IT} ($H_{IT, min}$) of the eutectic α -Al phase occurred in the central region between the Si phases, as shown in Fig. 3.6(a) and (b), both alloys exhibited high Al content. The typical P-h curves for the maximum H_{IT} ($H_{IT, max}$) and $H_{IT, min}$ obtained from the nanoindentation measurements are shown in Fig.3.10(a) and (b). The $H_{IT, max}$, E_{max} , and $H_{IT, min}$, E_{min} , in the Al-9Si alloy were 907MPa, 71GPa, and 801MPa, 67GPa, respectively.³⁷⁾ The difference between $H_{IT, max}$ and $H_{IT, min}$ was 46.1MPa. In contrast, the $H_{IT, max}$, E_{max} , and $H_{IT, min}$, E_{min} , in the 0.2Mo+0.2Zr addition alloy were 912MPa, 72GPa, and 764MPa, 67GPa, respectively, and its ΔH_{IT} was 96.1MPa.³⁷⁾ The alloy with the addition of 0.2Mo+0.2Zr showed twice as high a ΔH_{IT} due to the inhomogeneity of the degree of solid solution strengthening through the eutectic α -Al phase due to segregation during solidification. Furthermore, the alloy with the addition of 0.2Mo+0.2Zr had the slightest $H_{IT, min}$ showed the highest Al content layer or $\Delta Mkea$ in the eutectic α -Al phase as a continuous layer, as shown in Fig. 3.6(c) and (d). The deformation ability was better than that of Al-9Si alloy. Compared with the Al-9Si alloy, the ϵ_f of the alloy with the addition of 0.2Mo+0.2Zr was increased by 14%, as shown in Table 3.3.

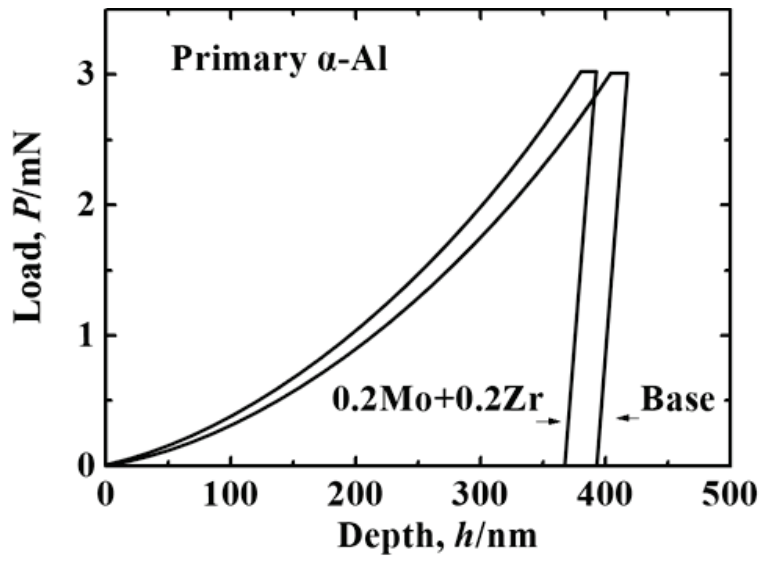


Fig.3.9 Load-depth curves of the primary α -Al phase of the Al-9Si and 0.2Mo+0.2Zr addition alloys.

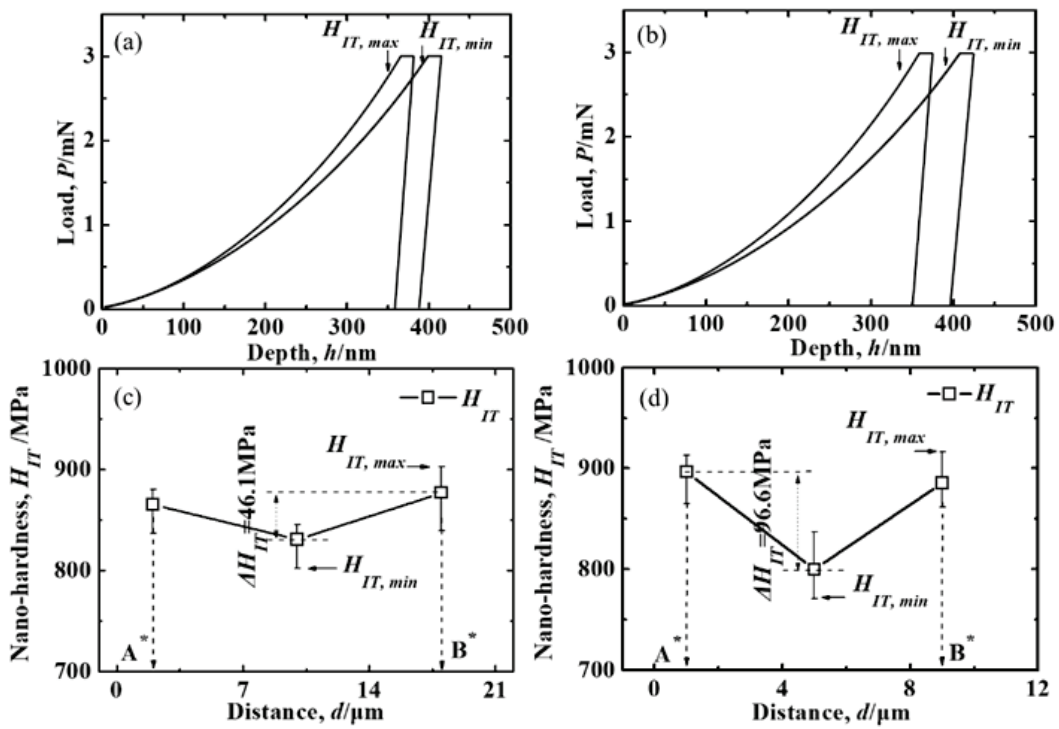


Fig. 3.10 (a) and (b) Load-depth curves, and (c) and (d) nanoindentation hardness distribution of the eutectic α -Al phase in Al-9Si 0.2Mo+0.2Zr addition alloys.

3.4.5 TEM observation for the solidification process

It seemed that the improvement of the ε_f in 0.2Mo+0.2Zr addition alloy was mainly related to the compositional inhomogeneity of the eutectic α -Al phase inhomogeneity segregation of solute atoms such as Mo and Zr. The dark-field image of the eutectic α -Al phase in Al-9Si and 0.2Mo+0.2Zr addition alloys cold-rolled with a plastic strain of 1% is shown in Fig. 3.11. The Al-9Si alloy showed a unit cell structure with an average size of 820 nm. The alloy with 0.2Mo+0.2Zr addition exhibited several small-sized unit cells with an average length of 250 nm at 1% plastic strain. The size of the cell structure may be related to one of the eutectic grains, as shown in Figures 3.1 and 3.3 and 3.6. Plastic deformation caused dislocations to form dense tangles of dislocations in areas with fewer dislocations or in the walls around the cell, which could be termed cellular structure.¹³⁾ The separated atoms may lead to the formation of walls, and the higher level of solid solution strengthening makes it difficult for dislocations to move. Several small-sized cell structures were observed in the 0.2Mo+0.2Zr addition alloy.³⁷⁾

In order to reveal the distribution of Mo and Zr in the eutectic α -Al phase, the bright field TEM image and element distribution of the eutectic α -Al phase of the 0.2Mo+0.2Zr addition alloy prepared by focused ion beam equipment are shown in Fig. 3.12. Light and dark fringes corresponding to areas marked "A" and "B" were observed within eutectic α -Al grains scaled from points 1 to 10. Points 1 to 10 in Fig. 3.12(a) corresponded to point (ii) in Fig. 3.12. As shown in Fig. 3.12(b), the black stripes showed the accumulation of dislocations due to the segregation of Mo and Zr atoms. The eutectic α -Al phase exhibited a heterogeneous structure with segregation of solute atoms, affected by solidification, which could improve the ductility of aluminum alloys.³⁸⁾

Al_3Zr and Al_{12}Mo were localized in the eutectic region of the 0.2Mo+0.2Zr addition alloy, as shown in Fig.3.3. However, they nucleate heterogeneously for subsequent eutectic reactions, especially in the Si phase during non-isothermal solidification. Their IMCs do not act as nucleation sites for primary α -Al phases. They are randomly distributed in the eutectic region and serve as nucleation sites for the eutectic Si phase.

During the non-isothermal solidification process after the crystallization of the primary α -Al phase, the solute elements in the liquid show an inhomogeneous concentration distribution even in the eutectic phase. The IMC of Al_3Zr and Al_{12}Mo crystallized (peak A) before the eutectic phase (peak B), as shown in the DTA curves. Al_3Zr and Al_{12}Mo with an average size of $0.3\ \mu\text{m}$ were observed in the eutectic Si phase, as shown in Fig. 3.3(d) and 3.6(b). It was thought that the added solute elements such as Mo and Zr migrate towards Al_3Zr and Al_{12}Mo , which acted as nucleation sites for eutectic Si.³⁷⁾

In contrast, Al content increased in the center area between Si phases in eutectic regions. The nucleation of the Si phase was caused at the surface of both IMCs (seen in Fig. 3.6(c)), and then the depleted zone of Mo and Zr was caused near Si.³⁷⁾ Thus, the α -Al phase with low solute elements was nucleated on the Si phase. Figure 3.12(a) and (b) revealed the abovementioned phenomena. Point 1 near Si showed a high Al content level or low ΔM_{ke} , as shown in Fig. 3.12(a) and (b). Region A and B with high and low Al or low and high Mo and Zr contents corresponded to low and high levels in hardness, respectively, as shown in Fig. 3.10.³⁷⁾

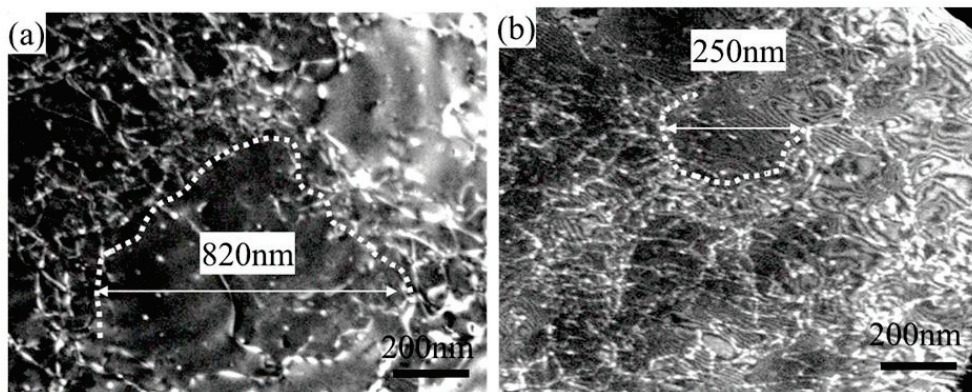


Fig. 3.11 Dark-field TEM images of the eutectic α -Al phase in the (a) Al-9Si and (b) 0.2Mo+0.2Zr addition alloys with 1 % plastic strain.

It is believed that in the 0.2Mo+0.2Zr addition alloy, Al_3Zr and Al_{12}Mo were the nucleation sites of eutectic Si, the solutes enrichment depended greatly on their diffusion coefficients in the liquid caused by keeping the local equilibrium in liquid

ahead of the solid and liquid interface, under same concentration between the solidified α -Al solid solution and infinity $C_{L\infty}$ in liquid representing by the effective equilibrium coefficient and a certain thickness of boundary layer depending on the solidification rate when $C_{L\infty}$ is equal to C_s in this model³⁹⁾. Solute mixing in liquid was conducted by just solute diffusion in this solidification process.

As shown in Fig. 3.12(b), these concentration profiles of Al, Mo, Zr, or $\Delta Mke\alpha$ correspond to the initial or steady phase of solidification³⁹⁾, according to the above model of solute enrichment with constitutive supercooling, which leads to heavy micro-segregation. Even in the eutectic region, solidification proceeded non-isothermally. The difference in solute atomic concentration denoted by ΔC_L between C_L and $C_{L\infty}$ corresponded to a larger Al or $\Delta Mke\alpha$ difference in the shortened distance, as shown in Fig. 3.6(c), (d) and Table 3.4. The degree of resolution (K) was approximated by Eq. (3-10) Use $C_{Al, max}$, $C_{Al, min}$, and $C_{Al, total}$ to show the concentrations of the maximum, minimum, and total Al content in eutectic α -Al, respectively, as listed in Table 3.4.

$$K = (C_{Al, max} - C_{Al, min}) / C_{Al, total} \times 100\% \quad (3-10)$$

Compared to the Al-9Si alloys (1.9 and 2.6), the 0.2Mo+0.2Zr alloy had a higher K value of 2.9 and a $\Delta Mke\alpha$ difference of 4.3 in the shorter region. In contrast, the Al-9Si alloy exhibited a different concentration distribution between α -Al solid solution and infinite liquid compared with 0.2Mo+0.2Zr addition, and its $C_{L\infty}$ was higher than that of C_s , which was due to the effect of solute diffusion and convection. Compared with the 0.2Mo+0.2Zr addition alloy, the Al-9Si alloy showed a smaller Al concentration or $\Delta Mke\alpha$ difference in a more significant area, as shown in Fig. 3.6(c), (d) and Table 4, which probably corresponded to the poorer liquid flow and refinement of the α -Al phase in the eutectic region of the 0.2Mo+0.2Zr addition alloy. Figure 3.6 reveals the different levels of Al content (ΔC_{Al} : 0.5%, 99.1%, 99.6%) between the aforementioned Al-9Si and 0.2Mo+0.2Zr addition alloys, respectively.

Table 3.4 The segregation coefficient K , $C_{Al, max} - C_{Al, min}$ and $\Delta Mke_{ea, max} - \Delta Mke_{ea, min}$ values of Al-9Si and 0.2Mo+0.2Zr addition alloys at the as-cast conditions.

Alloys	$C_{Al, max} - C_{Al, min}$ (%)	K	$\Delta Mke_{ea, max} - \Delta Mke_{ea, min}$ ($10^{-3}eV$)
Base	3.8	1.9	2.6
0.2Mo+0.2Zr	5.7	2.9	4.3

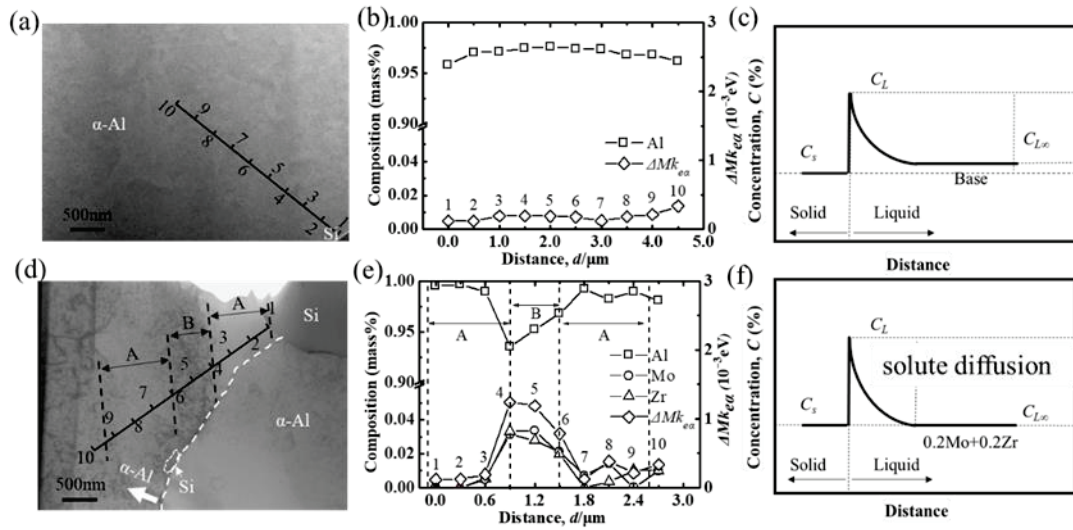


Fig. 3.12 (a) and (d) the bright-field TEM images of the eutectic α -Al phase in Al-9Si and 0.2Mo+0.2Zr addition alloys (b) and (e) the distribution of the elements and calculated ΔMke_{ea} of the Al-9Si and 0.2Mo+0.2Zr addition alloys. (c) and (f) schematic diagram of the solid-liquid interface of eutectic α -Al in the Al-9Si and 0.2Mo+0.2Zr addition alloys.

3.4.6 As-cast application possibility of the 0.2Mo+0.2Zr alloy

The Al-9Si-0.3Fe-0.15Mn alloy was selected as the base alloy, and 0.2Mo+0.2Zr was added to the Al-9Si alloy to maintain the ductility and increase the strength. Both σ_{UTS} (160MPa) and ε_f (7.1%) of the 0.2Mo+0.2Zr addition alloy in the as-cast conditions, were better than those of the (145 MPa, 6.1%) Al-9Si alloy. Figure 3.13 shows Vickers hardness for DA, ID, and a typical wide area composed of DA and ID for Al-9Si and 0.2Mo+0.2Zr addition alloys. The mixture rule in hardness was roughly established in both alloys. The ID consisting of eutectic and IMCs showed the highest hardness among alloys, especially because their error bars were large, and their values varied widely in the 0.2Mo+0.2Zr alloy. The characterization of the eutectic structure was believed to be the main reason for the improvements in both strength and ductility, which were usually correlated. Small IMCs such as Al_3Zr , $Al_{12}Mo$, and $Al_{15}(Fe, Mn, Mo)_3Si_2$ were scattered and aggregated in or near the eutectic grains of the 0.2Mo+0.2Zr addition alloy. Therefore, an increase in the volume fraction of Al_3Zr and $Al_{12}Mo$ ³³⁾ increases the tensile strength due to the solid solution and precipitation hardening mechanisms.³⁷⁾

On the contrary, in order to improve the ductility, the inhomogeneous α -Al phase in the eutectic took 72.2% as a continuous layer, which appeared as a high Al content layer or a solute-depleted zone, formed by the cluster distribution of Al_3Zr and $Al_{12}Mo$, which can be improved ductility by 0.2 Mo+0.2Zr addition to the base alloy. Thus, the inhomogeneous eutectic grains including IMC acted as a harmonic structure that enhances strength and ductility⁴¹⁾. It was found that the use of gravity casting method and the addition of Mo and Zr based on the progress of tensile properties indicated the possibility of as-cast applications because the eutectic Si particles were refined due to the crystallization of the two IMCs and the two IMCs both act as nucleation sites for eutectic Si⁴²⁾. Furthermore, the eutectic α -Al phase was characterized by high Al content or low ΔMke regions through micro segregation of Mo and Zr atoms.

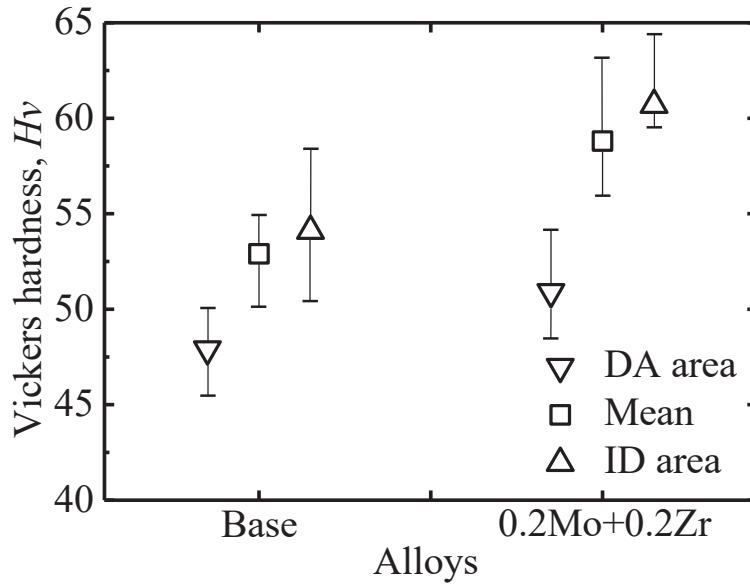


Fig. 3.13 Vickers hardness in the DA, ID, and typical wide area consisting of DA and ID of the Al-9Si and 0.2Mo+0.2Zr addition alloys.

3.4 Summary

(1) The microstructure with a finer SDAS values of $33.6\mu\text{m}$ and a larger eutectic region of 72.2% was obtained in 0.2Mo+0.2Zr addition alloy. The addition of 0.2Mo+0.2Zr alloy formed Al_3Zr and Al_{12}Mo before the primary $\alpha\text{-Al}$ phase crystallizes. They aggregated in the eutectic region and acted as nucleation sites for the eutectic Si phase.

(2) Both σ_{UTS} (160MPa) and ϵ_f (7.1%) of the alloy with 0.2Mo+0.2Zr addition in the as-cast condition were better than those of the Al-9Si alloy (145 MPa, 6.1%) due to solid solution strengthening and microstructural control., σ_{UTS} and ϵ_f increased by 8% and 14% with 0.2Mo+0.2Zr addition, respectively.

(3) Eutectic $\alpha\text{-Al}$ with minimum $H_{IT, min}$ showed high Al or low $\Delta M_{ke\alpha}$ due to severe micro segregation present as continuous phase in 0.2Mo+0.2Zr addition alloys leading to enhanced ductility. The size of the unit cell structure caused by dense dislocation entanglements was about 250 nm, corresponding to the similar size of high Al or low

$\Delta M_{ke\alpha}$ regions in 0.2Mo+0.2Zr addition alloys.

(4) Based on the improvement in tensile properties, it was found that the use of gravity casting method and the addition of Mo and Zr both indicated the possibility of as-cast applications, since the eutectic Si particles were refined due to the crystallization of the two IMCs and both IMCs acted as Nucleation sites for eutectic Si. The eutectic α -Al phase is characterized by regions of high Al content or low $\Delta M_{ke\alpha}$ through micro segregation of Mo and Zr atoms. The inhomogeneity of the eutectic grains (including IMC) acted as a harmonic structure that enhances strength and ductility.

References

- 1) Yoshihiko Hangai, Hiroto Kamada, Takao Utsunomiya, Soichiro Kitahara, Osamu Kuwazuru, Nobuhiro Yoshikawa: *Journal of Materials Processing Technology* **214** (2014) 1928-1934.
- 2) Peidong He, Richard F. Webster, Vladislav Yakubov, Hui Kong, Qin Yang, Shuke Huang, Michael Ferry, Jamie J. Kruzic, Xiaopeng Li: *Acta Materialia* **220** (2021) 117312.
- 3) J.G. Kaufman, E.L. Rooy: *Aluminum Alloy Castings: Properties, Processes, and Applications* (ASM International, USA) (2004) 9-20.
- 4) Lei Zhang, Shuying Chen, Qingchun Li, Guowei Chang: [Materials & Design](#) **193** (2020) 108853.
- 5) Qingyou Han, Hanbing Xu: *Scripta Materialia* **53** (2005) 7-10.
- 6) Jun Wang, Shuxian He, Baode Sun, Qixin Guo, Mitsuhiro Nishio: *Journal of Materials Processing Technology* **141**(2003) 29-34.
- 7) RHEINFELDEN ALLOYS GmbH & Co. KG: *Primary Aluminum Casting alloys* (2016) 17-63.
- 8) Silvia Lombardo, Ildiko Peter, Mario Rosso: *Materials Today: Proceedings* **10** (2019) 271-276.
- 9) Mohammadreza Zamani, Hoda Dini, Ales Svoboda, Lars-Erik Lindgren, Salem Seifeddine, Nils-Eric Andersson, Anders E. W. Jarfors: *International Journal of Mechanical Science* **121** (2017) 164-170.
- 10) M. Morinaga, N. Yukawa, and H. Adachi: *Tetsu-to-Hagane* **72** (1986) 555-562.
- 11) M. Morinaga, N. Yukawa: "Alloy Design Base on Molecular Orbital Method" *Computer Aided Innovation of New Materials*, Amsterdam (1991) 803-808.
- 12) Zeze Xiao, Kazuhiro Matsugi, Zhifeng Xu, Yongbum Choi, Kenjiro Sugio, Nobuyuki Oda and Jinku Yu: *Mater. Trans.* **61** (2020) 1255-1361.
- 13) K. Matsugi, S. Yamamura, Z.F. Xu, Y.B. Choi, K. Sugio, G. Sasaki and N. Oda: *Mater. Trans.* **56** (2015) 1675-1682.
- 14) M. Morinaga, S. Nasu, H. Adachi, J. Saito, and N. Yukawa: *J. Phys. Condens.*

- Mater 3 (1991) 6817-6828.
- 15) M. Morinaga and S. Kamado: *Model. Simul. Mater. Sci. Eng.* 1 (1993) 151-164.
 - 16) R. Ninomiya, H. Yukawa and M. Morinaga: *J. Japan Inst. Light Metals* 44 (1994) 171-177.
 - 17) Zeze Xiao, Kazuhiro Matsugi, Zhefeng Xu, Taishi Matsuoka, Tomoshi Uomi, Nobuyuki Oda, Hironobu Kominato, and Yasuo Uosaki: *PRICM-10, Xi'an (CHINA MACHINE PRESS)* (2019) 449-456.
 - 18) Meiqi Yu, Zhenfeng Xu, Yong Bum Choi, Takuma Konishi, Kazuhio Matsugi, Jinku Yu, Satoshi Motozuka, Kenichiro Suetsugu: *Mater. Trans.* 58 (2017) 140-147.
 - 19) M. Morinaga, N. Yukawa, H. Adachi, and H. Ezaki: *The Metallurgical Society of AIME, Warrendale (Superalloys 1984)* (1984) 523-532.
 - 20) K. Matsugi, Y. Murata, M. Morinaga, and N. Yukawa: *The Minerals, Metals and Materials Society, Warrendale (Superalloys 1992)* (1992) 307-316.
 - 21) K. Matsugi, T. Endo, Y. B. Choi and G. Sasaki: *Mater. Trans.* 51 (2010) 740-748.
 - 22) K. Matsugi, Y. Murata, M. Morinaga and N. Yukawa: *Mater. Sci. Eng. A* 172 (1993) 101-110.
 - 23) M. Morinaga, Y. Murata, and H. Ezaki: *Material Chemistry in Nuclear Environment, Tsukuba (Proc. Int. Symp.)* (1992) 241-252.
 - 24) K. Matsugi, H. Mamiya, Y. B. Choi, G. Sasaki, O. Yanagisawa and H. Kuramoto: *Int. J. Cast Metals Res.* 21 (2008) 156-161.
 - 25) XiLong Ma, Kazuhiro Matsugi, Zhefeng Xu, Yongbum Choi, Ryohei Matsuzaki, Zifeng Lin, Xingang Liu and Hao Huang: *Mater. Trans.* 60 (2019) 2426-2434.
 - 26) XiLong Ma, Kazuhiro Matsugi, Zhefeng Xu, Yongbum Choi, Ryohei Matsuzaki, Zifeng Lin, Xingang Liu and Hao Huang: *Mater. Trans.* 61 (2020) 740-749.
 - 27) M. Enomoto, H. Harada and H. Murakami: *Tetsu-to-Hagane* 80 (1994) 487-492.
 - 28) I. Ansara, B. Sundman, and P. Willemin: *Acta Metall.* 36 (1988) 977-982.
 - 29) T. Koyama: *J. Japan Inst. Metals* 73 (2009) 891-905.
 - 30) J. C. Slater, Phillips, James C: *Physics Today* 27 (1974) 49.
 - 31) Stefano Ferraro, Alberto Fabrizi, Giulio Timelli: *Materials Chemistry and Physics*

- 153 (2015) 168-179.
- 32) S. Seifeddine, I.L. Svensson: *Metall. Sci. Technol.* 27 (2009) 11-20.
- 33) S. Ji, W. Yang, F. Gao, D. Watson, Z. Fan: *Mater. Sci. Eng. A* 564 (2012) 130-139.
- 34) Geoffrey K. Sigworth: *International Journal of Metalcasting* 8 (2014) 7-20.
- 35) Kenjiro Sugio, Yasutaka Momota, Di Zhang, Hiroshi Fukushima and Osamu Yanagisawa: *Mater. Trans.* 48 (2007) 2762-2767.
- 36) W.C. Oliver, G.M.: *J. Mater. Res.* 7 (1992) 1564-158.
- 37) Zeze Xiao, Kazuhiro Matsugi, Zhefeng Xu, Nobuyuki Oda, Hironobu Kominato and Yasuo Uosaki: *Mater. Trans.* 63 (2022) 1452-1461.
- 38) A. R. Farkoosh, X. Gran Chen, M. Pekguleryuz: *Mater. Sci. Eng. A* 627 (2015) 127-138.
- 39) Yukio Saito: *Materia Japan* 49 (2010) 593-597.
- 40) W. Kurz and D. J. Fisher: *Fundamentals of solidification*, (Trans Tech Publications Ltd, Switzerland, 1998) 102-105.
- 41) Key Ameyama: *Sanyo Technical Report* 20 (2013) 1-9.
- 42) Akihiko Kamio: *J.JFS* 68 (1996) 1075-1083.

Chapter 4

Effects of Ti and V addition on microstructure and mechanical properties of Al-9Si alloys

<u>4.1 Introduction</u>	86
<u>4.2 Experimental procedure</u>	88
<u>4.2.1 Materials and manufacturing process</u>	88
<u>4.2.2 Evaluation of properties</u>	88
<u>4.3 Results and discussion</u>	89
<u>4.3.1 Microstructural characterization</u>	89
<u>4.3.2 Tensile properties</u>	92
<u>4.4 Summary</u>	95
<u>References</u>	96

4.1 Introduction

Al-Si alloys have been widely used in automotive industry production due to their high strength-to-weight ratio, low coefficient of thermal expansion, excellent castability and ease of recycling¹⁻³). With increasing demands for greater fuel efficiency and improving applied material safety and stability, there is a need to develop high-performance Al-Si alloys that are able to withstand severe operating conditions. Good mechanical properties of Al-Si alloys can be improved by alloy strengthening and subsequent heat treatment. However, under the background of reducing the production cost, the application of the Al-Si alloys in the casting condition has attracted attention.

The development of high-performance aluminum alloys relies on a lot of experiments and some experience. In order to develop new Al-Si alloys more efficiently, we urgently need scientific alloy design theory. The d-electron concept based on theoretical calculations has been applied to the design of high-performance materials such as Al, Bi, Ni, Ti, Mg, Fe-based alloys, and some physical or chemical properties of the designed materials have been successfully predicted by this concept⁴⁻⁹). The parameters of the aluminum alloy composition were also obtained from electronic methods¹⁰⁻¹³). It is the s-orbital level Mki of the alloying transition or non-transition element i . For s, p simple metals, such as aluminum, the d orbital energy levels are no longer applicable to the transition metal-based alloys mentioned above. The s orbital level exists above the Fermi level of the $MAl18$ cluster containing the alloying element M and its surrounding aluminum atoms. This parameter is calculated by DV- $X\alpha$ cluster, so this parameter inevitably involves alloying effects. Mki levels decrease with increasing electronegativity and increase with increasing atomic radius of the element. It is well known that the energy levels obtained by DV- $X\alpha$ cluster calculations represent the electronegativity itself¹⁴). There is also a linear relationship between the Mki energy level and the average energy level of all s-orbitals of the element M present in the $MAl18$ cluster. Also, p-orbital energy levels can be considered instead of s-orbital levels, but spherically symmetric s-orbitals may be better than oriented p-orbitals for studying

the mechanical properties of aluminum alloys¹⁵).

In order to further increase the strength of the Al-Si alloys in critical structural applications, reinforcing particles have been applied¹⁶⁻¹⁸). Among the reinforcing materials, the Al₃Ti intermetallic phase is superior to other materials due to its low density and high modulus. Furthermore, Al₃Ti particulates generally exist inside α -Al grains through a peritectic reaction in solidification, resulting in strong interfacial bonding between the reinforcing particulates and the Al matrix¹⁸). The peritectic reaction not only eliminates the degradation of ductility due to the segregation of reinforced particulates at the grain boundaries but also results in the grain refinement of the Al matrix¹⁹). The addition of solutes such as V is known to be an effective method to introduce active heterogeneous nucleate particles promoting the grain refinement of Al alloys¹⁹). Recently, Kasprzak et al.²⁰) studied the addition of Ti, V and Zr to the A356 alloy. They indicated that compared to the base alloys, the stable Al-Si-Zr-Ti nanoprecipitates in the α -Al matrix are responsible for the excellent mechanical properties at high temperatures. However, the effect of V is still unclear even though the concentration was increased to 0.2 mass%. They also observed that V in concentrations up to 0.06% remains in solid solution or is dissolved in ternary Al-Fe-Si phases and not found the V-based intermetallic compounds in the microstructure of the alloys.

The values of Mk_i for Ti and V element which were calculated on the MAI_{18} cluster model in the case of FCC Al are 5.009 and 4.782, respectively. Among the transition element elements, they have a higher Mk value¹⁴), which may lead to poor phase stability and high segregation degree in solidification. High and different Mk values mean that Ti and V have different effects on Al alloys. It is important to establish whether the addition of Ti and V to Al-Si alloys have a beneficial or detrimental effect on the microstructural features and consequently on mechanical properties. Therefore, the aim of the present work is to investigate the effect of the elements Ti and V on the mechanical properties of as-cast Al-9Si-0.3Fe-0.15Mn alloy foundry alloys. Microstructural and fractographic analyses were performed to investigate the microstructural features involved in the fracture process.

4.2 Experimental procedure

4.2.1 Materials and manufacturing process

A series of Al-9Si alloys with Ti and V addition were prepared using industrially pure Al and Si chips. In order to avoid any masking effects or interactions with additional elements, neither Sr nor Na was added as modifier agents. The raw materials prepared in a clay-graphite crucible were melted in an induction furnace at 1009K~ 1013K for 1.2ks. An Argon gas purification technique was used to eliminate gases for 300s and then the melt was poured into a steel mold preheated at 477K. The ingots were cooled to room temperature in the mold. The size of the cast ingots was 195mm × 23mm × 39 mm. The chemical compositions of alloys analyzed with inductively coupled plasma (ICP) apparatus are shown in Table 4.1.

Table 4.1 The compositions and $\Delta M k_t$ values of designed alloys.

Alloys	$\Delta M k_t$	SDAS (μm)	Chemical composition, mass %					
			S	F	M	T	V	A
			i	e	n	i		l
Base	0.0601	35	8.83	0.38	0.15	/	/	Bal.
0.2Ti	0.0611	37	8.13	0.39	0.15	0.17	/	Bal.
0.2V	0.0610	33	8.68	0.40	0.15	/	0.17	Bal.

4.2.2 Evaluation of some properties

Specimens for microstructural observations were taken from each ingot at a position one half of its length (195mm), width (23mm) and height (39mm). The microstructures of alloys were performed using optical microscopy (OM) and electron probe microanalyzer (EPMA). The Image-pro software was employed to measure volume fraction of phase and grain sizes, which determined the mean grain size as the average

diameter length measured by the centroid of each grain. Differential thermal analysis (DTA) with a heating-cooling rate of $5\text{K}\cdot\text{min}^{-1}$ was used to investigate solidification paths, and the liquidus temperature of the alloys was also measured. Each test was repeated at least two times to ensure reproducibility of the detected temperature.

Tensile test specimens with a diameter of 6 mm and a gauge length of 80mm were machined from the cast ingot. The tests of tensile were performed at a strain rate of $1.0\text{mm}\cdot\text{min}^{-1}$ at room temperature with CATY2005S testing machine. The tensile strain was accurately measured by using extensometer until the necking. The tensile tests were repeated four times and taken the average value. After the tensile tests, the fracture surfaces were observed using a scanning electron microscope (SEM) to explain the alloy deformation characteristics.

4.3 Results and discussion

5.3.1 Microstructural characterization

The OM and the backscattered electron (BSE) images of the experimental alloys were shown in Fig. 4.1. The general features were α -Al dendrites (light grey) and needle-like Si particles (dark grey) and no micropores are observed in any of the samples due to good casting conditions. As a direct consequence, this defect is not regarded as a parameter influencing the tensile properties. It was also observed that the base alloy is presenting a dendritic structure with the secondary dendrite arm spacing (SDAS) range around $35\mu\text{m}$, as shown in Fig. 4.1(a). All experimental alloys showed primary α -Al phase with dendritic structure and eutectic region. The eutectic region was increased by the addition of Ti and V. The SDAS of the experimental alloys were also shown in Table 4.2. The SDAS showed similar values among experimental alloys. However, the smallest SDAS was shown in the 0.2V addition alloy. This indicated that the V additions have a slight grain refinement on the microstructure in the as-cast condition. Mondofo.²⁰⁾, Edwards et al.²¹⁾, Maitland.²²⁾ and Thomas et al.²³⁾ also reported that V has a mild grain refinement effect.

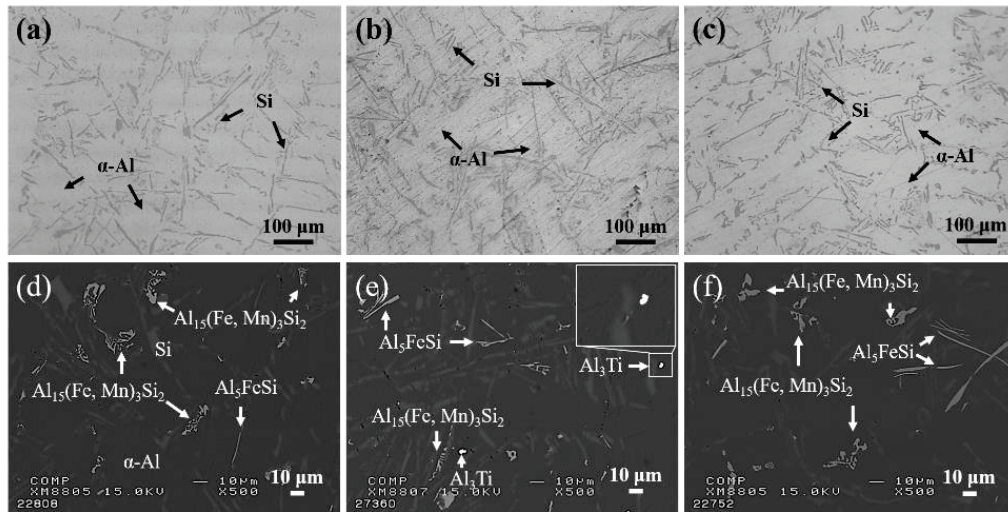


Fig. 4.1 OM and BSE images obtained from the base alloy: (a) and (d); 0.2Ti addition alloy: (b) and (e); 0.2V addition alloy: (c) and (f). The general features were the dendrite arm area (DA) and the inter-dendritic area (ID) among the alloys. The ID was increased by the addition of Ti and V.

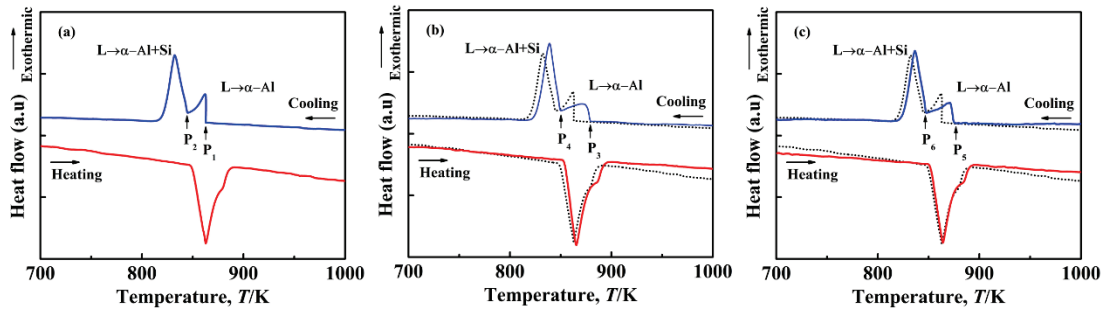
Table 4.2 The chemical composition of phases measured by EDS and the volume fraction results of phase in the alloys.

Alloys	Identified Phase	Volume fraction (%)	Compositions (mol%)					
			Al	Si	Fe	Mn	Ti	V
Base	α -Al	86.9	99.33	0.62	0.02	0.03	/	/
	$\text{Al}_{15}(\text{Fe, Mn})_3\text{Si}_2$	2.1	75.15	10.21	11.08	3.56		
	Al_3FeSi	0.3	54.86	30.82	11.67	2.65	/	/
0.2Ti	α -Al	87.3	99.30	0.61	0.02	0.04	0.03	/
	$\text{Al}_{15}(\text{Fe, Mn})_3\text{Si}_2$	2.0	75.22	11.10	10.13	3.55	0.00	/
	Al_3Ti	0.1	57.62	19.79	0.04	0.00	22.55	/
0.2V	α -Al	84.1	99.32	0.56	0.01	0.03	/	0.07
	$\text{Al}_{15}(\text{Fe, Mn})_3\text{Si}_2$	2.7	73.56	10.89	9.71	3.93	/	1.91
	Al_3FeSi	1.1	59.01	26.89	8.98	3.57	/	1.55

The BSE images of the base alloy exhibited α -Al dendrites, needle-like Si particles, $\text{Al}_{15}(\text{Fe},\text{Mn})_3\text{Si}_2$ and Al_5FeSi phases (Fig. 4.1(d)). The representative chemical composition of some of the investigated phases determined by EDS is given in Table 4.2. The morphology of Al_5FeSi was acicular polygonal, whereas $\text{Al}_{15}(\text{Fe}, \text{Mn})_3\text{Si}_2$ exhibited a “Chinese-script” morphology. The addition of 0.2Ti to base alloy resulted in the formation of Ti based intermetallic phases in addition to the phases observed in the base material (Fig. 4.1(e)). According to the EDS measurements, these particles were identified as Al_3Ti . Microstructural observations also revealed an increased amount of $\text{Al}_{15}(\text{Fe}, \text{Mn})_3\text{Si}_2$ phases and Al_5FeSi phases in the 0.2V addition alloy (Fig. 4.1(f)). Additionally, a certain amount of V can accumulate into $\text{Al}_{15}(\text{Fe}, \text{Mn})_3\text{Si}_2$ phase and Al_5FeSi phase. The volume fraction of each phase has been analysed by image processing software and the obtained results were demonstrated separately in Table 4.2. The volume fraction of α -Al dendrites, needle-like Si particles, $\text{Al}_{15}(\text{Fe}, \text{Mn})_3\text{Si}_2$ and Al_5FeSi phases in the base alloy were 86.9, 10.7, 2.1 and 0.3%, respectively. The introduction of 0.2Ti to base alloy resulted in the formation of Al_3Ti compound, which distributed in the Al-Si eutectic region. The volume fraction of the Al_3Ti was 0.1%. The volume fraction of the $\text{Al}_{15}(\text{Fe}, \text{Mn})_3\text{Si}_2$ and the Al_5FeSi phases in the 0.2V addition alloy were 2.7 and 1.1%, respectively. As shown in Fig. 4.1(f), some coarsening Al_5FeSi phase were observed in the 0.2V addition alloy (compare with Fig. 4.1(d)). This is because of the V segregated in the Al_5FeSi phase which changes its growth morphology. The intermetallic could not be acted as the sites of heterogeneity nucleation in solidification. The Ti and V addition alloys showed a narrow and shorted Si phase in the eutectic grains.

In particular, the smaller Al_3Ti compound was formed in the eutectic region on Ti addition alloy, as shown in Fig. 4.1(e). Fig. 4.2 shows the DTA results of experimental alloys. There were similar peaks in heating curves, but different P_a (Liquidus temperature) and P_b (Eutectic reaction temperature) in cooling curves. The summary of the characteristic temperatures that are determined by analysing the cooling curves was

shown in Table 4.3. The intermetallic compounds increased by the addition of Ti and V, which led to the 12-17 K increase in melting temperatures and micro-segregation in solidification. The intermetallic could not be acted as the sites of heterogeneity nucleation in solidification. It is considered that Ti and V were present gradually in



eutectic regions, keeping the high segregation degree.

Fig. 4.2 DTA curves obtained from (a) base, (b) 0.2Ti and (c) 0.2V alloys.

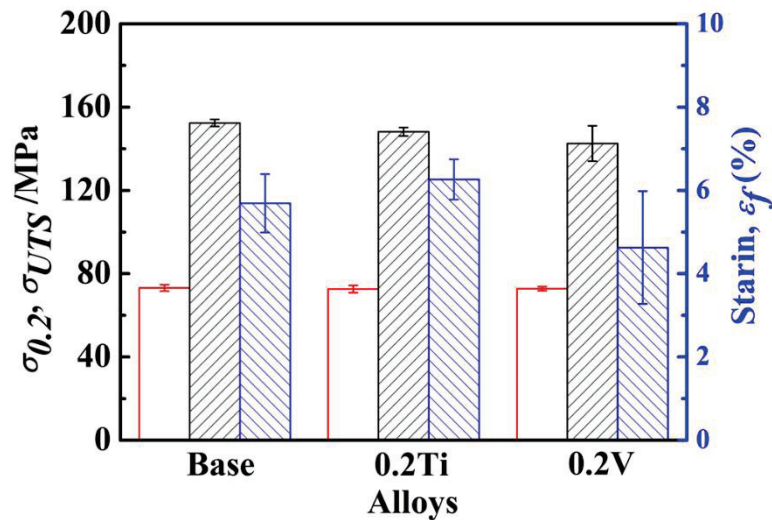
Table 4.3 Characteristic temperatures from traditional thermal analysis of the experimental alloys in kelvin (K).

Alloys	P_a (Liquidus temperature)	P_b (Eutectic reaction temperature)
Base	862.9	844.5
0.2Ti	879.5	846.9
0.2V	874.7	846.2

5.3.2 Tensile properties

The average values of the tensile properties of the experimental alloys are summarized in Fig. 4.3. It was observed that the 0.2% flow stress ($\sigma_{0.2}$) and ultimate tensile strength (σ_{UTS}) of the base alloy were 73MPa and 152MPa, respectively. The fracture strain of the base alloy was 5.7%. The 0.2Ti and 0.2V addition alloys showed the same $\sigma_{0.2}$ value of 73MPa. In contrast, the σ_{UTS} value decreased a little by V addition. The 0.2Ti and 0.2V addition alloys showed 0.6% increase and 1.1% decrease in fracture

strain, respectively, compared with the base alloy. In addition, the effect of 0.2V addition is accompanied by a larger scatter in fracture strain, compared to other alloys. This corresponded to the unstable in microstructure by V addition. The longer shaped



Al_5FeSi phase, as seen in Fig. 4.1(f), contributes to the initiation of fatigue cracks²⁴).

Fig. 4.3 The average values of the tensile properties of the experimental alloys.

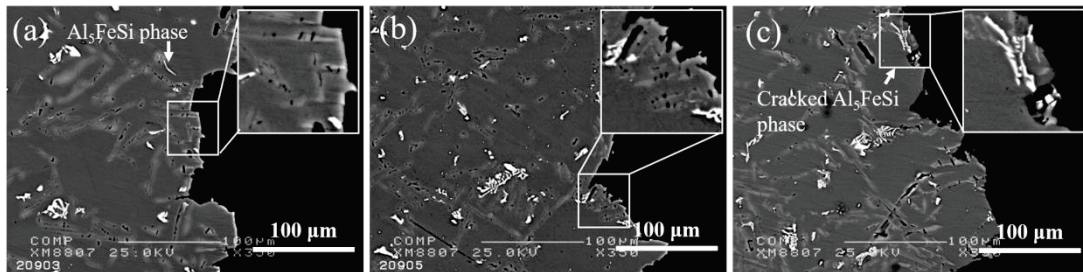


Fig. 4.4 The photographs of longitudinal sections nearby tensile fracture of the (a) base alloy, (b) 0.2Ti and (c) 0.2V alloys.

The fracture surface of longitudinal sections nearby tensile fracture of the experimental specimens is shown in Fig. 4.4. Similar to other studies of the fracture mechanism in Al-Si alloys²⁴⁻²⁶), fracture initiates because of intercrystallite cracking of needle-like eutectic Si particles and some brittle intermetallic. Once a critical number of fractured particles is reached, the principal crack is formed by the local linkage of

adjacent microcracks, and subsequent propagation of these. The crack follows a preferential path through the needle-like eutectic Si particles in the interdendritic regions, thus showing a trans granular fracture mode. The aforementioned fracture behavior provides evidence that eutectic Si particles located between the secondary dendrite arms constitute an easier path for crack propagation than those located at or near the α -Al grain boundaries. This seems to be completely consistent with previous findings²⁶⁻²⁸. No significant differences in fracture paths are observed between the base and 0.2Ti addition alloys. However, the cracked Al_5FeSi phase can be observed in the fracture surface in the 0.2V addition alloy. This result is also consistent with the decrease of the ductility of the alloys with the addition of 0.2V. The 0.2Ti addition alloy showed the fracture morphology consisting of wavy crack propagation lines in the eutectic region, as seen Fig. 4.4 (b) right corner, which resulted from the ductilization of α -Al phase in eutectic by Ti addition. The 0.2Ti addition alloy showed the formation of thin region of pure Al with high ductility by segregation gradient of Ti in the eutectic region as shown in Fig .4.5. It is found that 0.2Ti addition alloy showed improvement of fracture strain keeping the strength level, which was suitable for as-cast applications intended for lightweight materials for the automobiles.

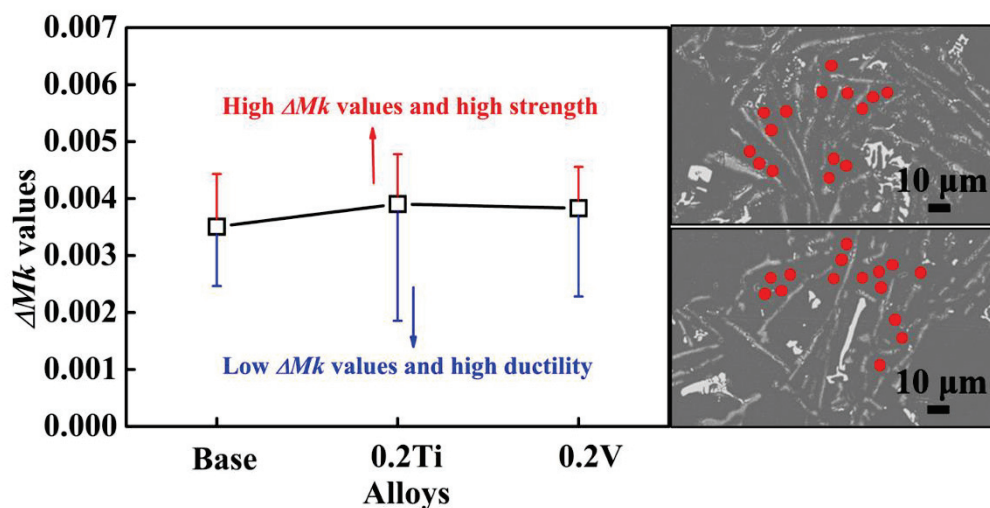


Fig. 4.5 The results in the eutectic α -Al phase by point analysis.

4.4 Summary

(1) The base and 0.2V addition alloys exhibited the α -Al dendrites, eutectic Si and a small amount of the intermetallic compounds, such as $\text{Al}_{15}(\text{Fe}, \text{Mn})_3\text{Si}_2$ and Al_5FeSi . In particular, the smaller Al_3Ti compound was formed in the eutectic region on Ti addition alloy. The intermetallic compounds increased by the addition of Ti and V, which led to the 12-17 K increase in melting temperatures and micro-segregation in solidification.

(2) The experimental alloys showed the following tensile values of the strain (ϵ_f) and 0.2% flow stress ($\sigma_{0.2}$): base: 5.7% and 73 MPa; 0.2Ti addition alloy: 6.3% and 73 MPa; 0.2V addition alloy: 4.6% and 73MPa, respectively. The Ti and V addition led to similar strength level to the base alloy. In contrast, the 0.2Ti and 0.2V addition alloys showed 0.6% increase and 1.1% decrease in fracture strain, respectively, compared with the base alloy.

(3) The 0.2Ti addition alloy showed the fracture morphology consisting of wavy crack propagation lines in the eutectic region, which resulted from the ductilization of α phase in eutectic by Ti addition. The 0.2Ti addition alloy showed the formation of thin region of pure Al with high ductility by segregation gradient of Ti in the eutectic region.

(4) It is found that 0.2Ti addition alloy showed improvement of fracture strain keeping the strength level, which was suitable for as-cast applications intended for lightweight materials for the automobiles.

References

- 1) R.X. Li, R.D. Li, Y.H. Zhao, L.Z. He, C.X. Li, H.R. Guan, Z.Q. Hu, *Mater. Lett.* 58 (2004) 2096–2101.
- 2) G. Jha, S. Ningileri, X. Li, R. Bowers, in B. Sadler (Ed.), *Light Metals 2013*, John Wiley & Sons Inc., Hoboken, New Jersey. 2013, 929–934.
- 3) J. Grandfield, L. Sweet, C. Davidson, J. Mitchell, A. Beer, S. Zhu, X. Chen, M. Easton, in B. Sadler (Ed.), *Light Metals 2013*, John Wiley & Sons Inc. Hoboken, New Jersey. 2013, 39–44.
- 4) M. Yu, Z. Xu, Y. Choi, T. Konishi, K. Matsugi, S. Motozuka, K. Suetsugu and J. Yu: *Mater. Trans.* 58 (2017) 140-147.
- 5) M. Morinaga, N. Yukawa, H. Adachi and H. Ezaki: *Superalloys 1984*, (The Metallurgical Society of AIME, Warrendale, PA, 1984), 523-532.
- 6) K. Matsugi, Y. Murata, M. Morinaga and N. Yukawa: *Superalloys 1992*, (The Minerals, Metals and Materials Society, Warrendale, PA, 1992), 307-316.
- 7) K. Matsugi, T. Endo, Y. B. Choi and G. Sasaki: *Mater. Trans.* 51 (2010) 740-748.
- 8) K. Matsugi, Y. Murata, M. Morinaga and N. Yukawa: *Mater. Sci. Eng. A.* 172 (1993) 101-110.
- 9) W. J. Boesch and J. S. Slaney: *Metal Progress.* 86 (1964) 109-111.
- 10) L. Pauling. *Phys. Rev.* 54 (1938) 899.
- 11) M. Morinaga, Y. Murata and H. Ezaki: *Proc. Int. Symp. Material Chemistry in Nuclear Environment*, (Tsukuba, March 1992), 241-252.
- 12) K. Matsugi, H. Mamiya, Y. B. Choi, G. Sasaki, O. Yanagisawa and H. Kuramoto: *Int. J. Cast Metals Res.* 21 (2008) 156-161.
- 13) M. Morinaga, N. Yukawa and H. Adachi. *Tetsu-to-Hagane.* 72 (1986) 555-562.
- 14) K. Matsugi, S. Yamamura, Z.F. Xu, Y.B. Choi, K. Sugio, G. Sasaki and N. Oda. *Mater. Trans.* 56 (2015) 1675–1682.
- 15) M. Morinaga, S. Nasu, H. Adachi, J. Saito and N. Yukawa, *J. Phys. Condens. Matter* 3 (1991) 6817-6828.

- 16) S.K.Shaha, F.Czerwinski, W.Kasprzak, J.Friedman, D.L.Chena. Thermal stability of $(\text{AlSi})_x(\text{ZrVTi})$ intermetallic phases in the Al–Si–Cu–Mg cast alloy with additions of Ti, V, and Zr [J]. *Thermochimica Acta*. 595 (2014) 11-16.
- 17) S.K.Shaha, F.Czerwinski, W.Kasprzak, J.Friedman, D.L.Chena. Monotonic and cyclic deformation behavior of the Al–Si–Cu–Mg cast alloy with micro-additions of Ti, V and Zr [J]. [International Journal of Fatigue](#). 70 (2015) 383-394.
- 18) N. Saheb, T. Laoui, A.R. Daud, et al. Influence of Ti addition on wear properties of Al-Si eutectic alloys[J]. *Wear*. 248 (2001) 656-662.
- 19) F. Wang, Z. Liu, D. Qiu, J.A. Taylor, M.A. Easton, M.-X. Zhang, *Acta Mater*. 61 (2013) 360–370.
- 20) W. Kasprzak, D. Emadi, M. Sahoo, M. Aniolek, *Mater. Sci. Forum* 618–619 (2009) 595–600.
- 21) Lucio F. Mondolfo. *Aluminum alloys: structure and properties* (London, Butterworths, 1976), 392-394.
- 22) W. M. Edwards et al. Development of near-eutectic Al-Si casting alloys for piston applications [J]. *Materials Science Forum*, 625 (2002) 396-402.
- 23) A. H. Maitland and D. Rodriguez. Vanadium in aluminum. *Proceedings of the 8th international light metals congress, 1987*, 423-425.
- 24) Thomas H. Ludwig, Paul L. Schaffer, Lars Amberg. Influence of vanadium on the microstructure of A356 foundry alloy. *Light Metals*. 2013.
- 25) TongGao, Pengting Li, Yunguo Li, Xiangfa Liu. Influence of Si and Ti contents on the microstructure, microhardness and performance of TiAlSi intermetallics in Al–Si–Ti alloys[J]. *Journal of Alloys and Compounds*. 509 (2011) 8013-8017.
- 26) Q.G. Wang. Microstructural effects on the tensile and fracture behavior of aluminum casting alloys A356/357[J]. *Metall. Mater. Trans. A*. 34 (2003) 2887–2899.
- 27) M. Zhu, Z. Jian, G. Yang, Y. Zhou. Effects of T6 heat treatment on the microstructure, tensile properties, and fracture behavior of the modified A356 alloys [J]. *Mater. Des*. 36 (2012) 243–249.
- 28) D. Casari, A. Fortini, M. Merlin, Fracture behavior of grain refined A356 cast

aluminum alloy, in Proceedings of the Convegno Nazionale IGN XXII, Rome, 2013.

Investigate the as-cast applicability for different series of Al-Mn and Al-Si alloys by electronic parameters

5.1 Introduction..... 101

5.2 Proposed method for the estimation of mechanical properties 103

5.3 Results and discussion 105

 5.3.1 Microstructural characterization 105

 5.3.2 Tensile properties for as-cast applicability..... 107

5.4 Summary..... 111

References 112

Apendix..... 113

5.1 Introduction

The mechanical properties of metals and alloys have been by dislocation theory. For Al alloys, the strain hardening of alloys is related to the high densities of dislocations introduced by cold working¹⁾. The solid- solution hardening will arise from the disturbing effects of solute atoms on dislocation motion²⁾. However, although dislocation theory has made significant progress in understanding mechanical properties, there are still significant obstacles in quantitatively predicting alloy strength with the help of this theory. This may be due to the complexity of the interactions between dislocations and solute atoms and the poor understanding of the dislocation core structure. In order to solve these difficulties, being distinct from the continuum approach to solids, atomistic approaches to the core structure and the fracture problems have been undertaken, assuming proper interatomic potentials and forces³⁻⁵⁾. Through microscopic methods, the mechanical properties of alloys can be fundamentally understood.

In the present study, we tried to find a way to predict the mechanical properties of different series of aluminum alloys. Several physical parameters such as bond order, ionicity, and s-orbital energy levels of alloying elements are related to the electronegativity and atomic radius of the elements, as shown in Fig. 5.1, were obtained and found to be essential to the understanding of various alloy properties⁶⁾. Among these parameters, the s-orbital energy level Mk was found to be suitable for estimating the mechanical properties of commercial aluminum alloys with multiple components. This chapter presents a series of results and will propose a new approach to the mechanical properties of Al-Mn and Al-Si alloys.

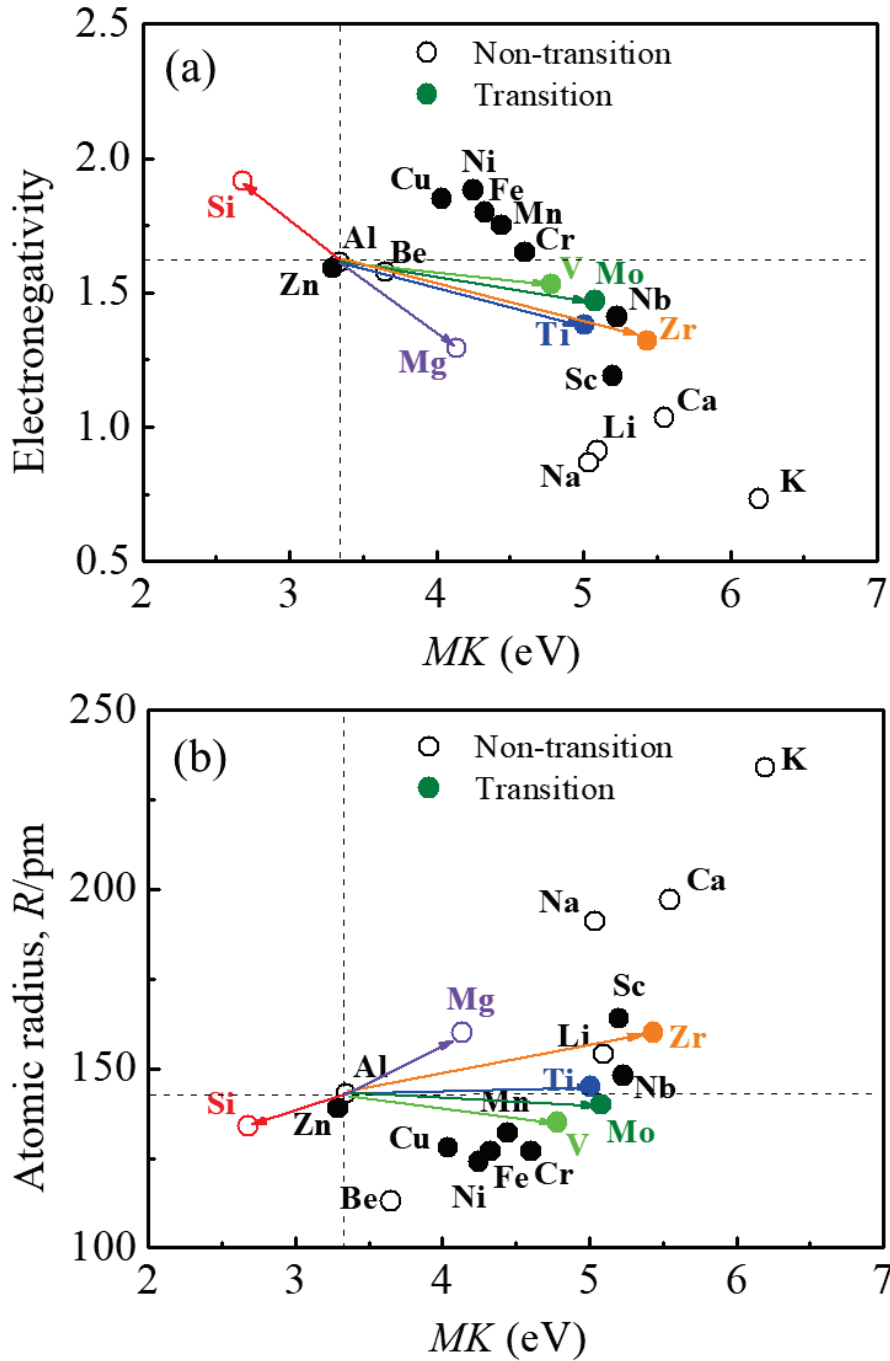


Fig. 5.1 Mk values of each alloying element of aluminum and the relations of the (a) electronegativity (b) atomic radius (\circ Non-transition, \bullet Transition element).

5.2 The proposed method for the estimation of mechanical properties

The parameters used in the compositional optimization of aluminum alloys were obtained from electronic methods of alloy design.⁸⁻¹⁰⁾ The electronic parameter Mki is the s-orbital energy level that exists above the Fermi level of the $iAl18$ cluster, containing the alloying element i and its surrounding aluminum atoms.¹¹⁾ Various parameters have been proposed to describe the alloying behavior. However, the electronegativity and atomic radius of the elements are chosen here because they represent the properties of chemical bonds between atoms in solids.¹¹⁾ There is a good correlation between electronegativity or atomic radius and the Md parameter of the d-orbital energy level for transition metals, as described in Section 1. For s,p simple metals such as Al, d orbital levels are no longer valid in transition metal-Al-1.5Mnd alloys. Mki is the s-orbital energy level excited above the Fermi level, and the discrete variation $X\alpha$ cluster calculation. Therefore, alloying effects are inevitably involved in Mki .¹¹⁾ It is well known that the energy levels obtained by DV- $X\alpha$ cluster calculations represent the electronegativity itself.^{10,11)} The Mki values of each alloy element calculated by the $iAl18$ cluster model in FCC Al are shown in Table 2.1.^{10, 11)} The Mki value decreases with increasing electronegativity. Instead, it increases with the atomic radius of the element, as shown in Fig. 5.1.^{10,11)} Also, p orbital energy levels can be considered instead of s orbital energy levels. However, for studying the mechanical properties of aluminum alloys, spherically symmetric s-orbitals may be better than oriented p-orbitals.¹¹⁾

Table 5.1 List of Mk_i values of alloying elements in the FCC Al cluster.^{19, 20)}

Elements	Mk_i (eV)	Elements	Mk_i (eV)	Elements	Mk_i (eV)
Li	5.096	Sc	5.200	Cu	4.037
Be	3.650	Ti	5.009	Zn	3.290
Na	5.036	V	4.782	Ga	3.013
Mg	4.136	Cr	4.601	Ge	2.614
Al	3.344	Mn	4.443	Zr	5.433
Si	2.680	Fe	4.328	Nb	5.227
K	6.196	Co	4.314	Mo	5.079
Ca	5.550	Ni	4.248		

Except for Si, Zn, Ga and Ge, most elements have higher Mk_i values than Al. For alloys, two average values of s-orbital energy levels, Mk_t and ΔMk were defined by taking the compositional average using Eqs. (5-1) and (5-2).

$$Mk_t = \sum x_i Mk_i \quad (5-1)$$

$$\Delta Mk = \sum x_i |Mk_i - Mk_m| \quad (5-2)$$

Where x_i is the mole fraction of component i in the alloy, Mk_i and Mk_m are the Mk value for component i and Al, respectively. When all the elements in the alloy have a higher (or lower) Mk_i value than Al, these two averages differ only by a constant bias of Mk_m value of 3.344; hence, there is no essential difference between them.

5.3 Results and discussion

5.3.1 Microstructures characterization

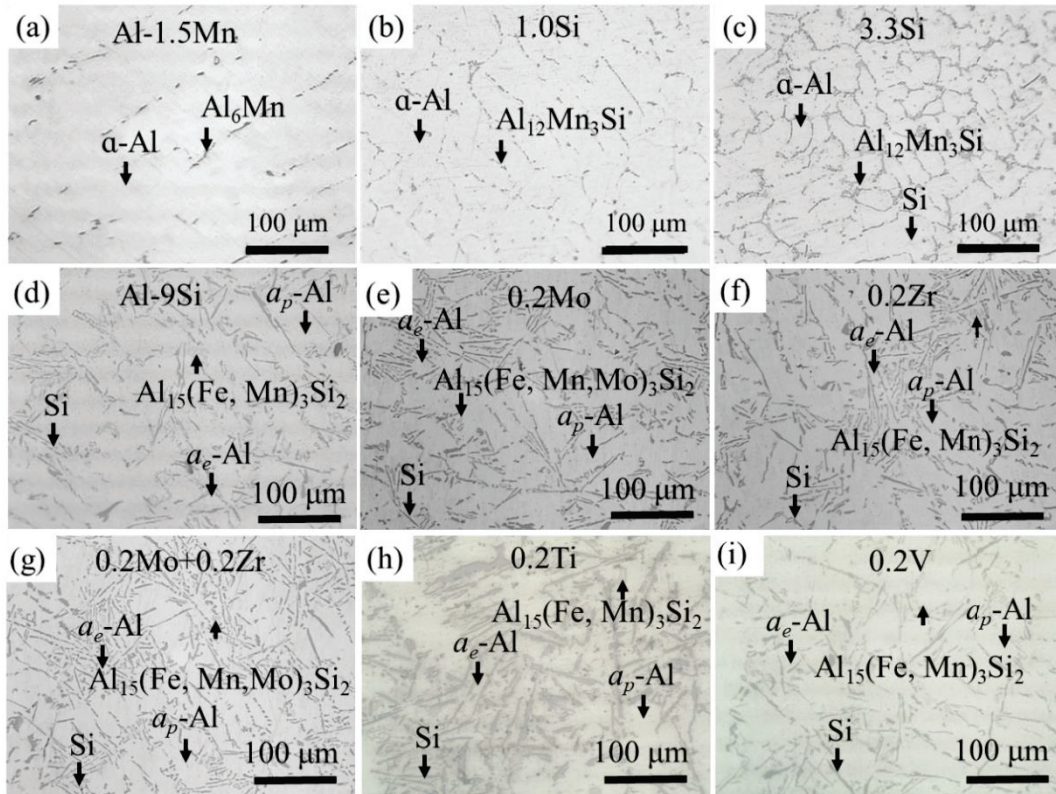


Fig. 5.2 Optical micrographs of the Al-1.5Mn and Al-9Si alloys.

The microstructures of the Al-1.5Mn and Al-9Si alloys in the as-cast conditions are shown in Fig.5.2. No micropores were observed throughout the samples due to good casting ability. Dendritic structures with different size were obtained in Al-1.5Mn and Al-9Si alloys, and these dendritic structures predominantly consisted of the primary α -Al phase (α_p -Al). The volume fractions of the α_p -Al phase in the Al-1.5Mn, 1.0 and 3.3Si, Al-9Si and 0.2Mo+0.2Zr alloys were 99.3, 98.6, 96.1%, 33.3% and 27.3%, respectively, and other parts were defined as the eutectic consisting of the eutectic α -Al (α_e -Al), Si and some intermetallic compounds (IMCs). The phase and phase volume fraction were shown in Appendix 1. With the increase of Si, the volume fraction of α_p -Al phase decreased, while the volume fraction of eutectic increased. The addition of

elements refined the solidified structure of the addition of Si to Al-1.5Mn and the addition of Mo+Zr to Al-9Si with the SDAS of 47.9, 36.5, 41, and 33 μm , respectively.

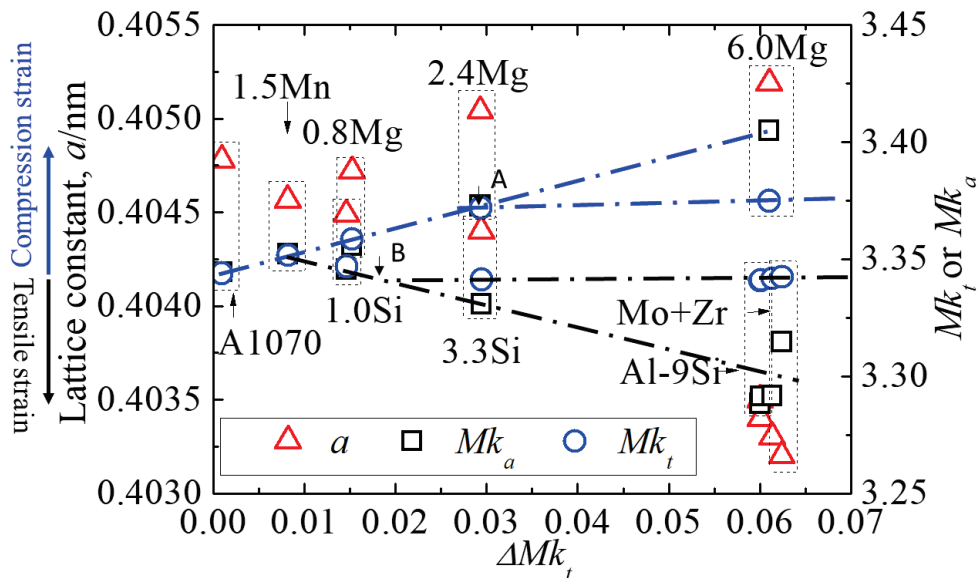


Fig. 5.3 Relationship between ΔMk_t value and the lattice constant, Mk_α or Mk_t values of the experimental alloys.

Figure 5.3 shows the relationship between ΔMk_t value and the lattice constant, Mk_α or Mk_t values of the experimental alloys. The lattice constant decreased or increased linearly with the increased in ΔMk_t values. It is considered that the decrease or increase in lattice constant was related to the amounts of solid solution elements in the α -Al phase. In addition, Mg addition alloys and Si addition alloys have different directions in the changing trend of lattice constants. This is because Mg and Si have different atomic radius, the solute Mg with a larger atomic radius expands the lattice of aluminum, and conversely, the solute Si with a smaller atomic radius shrinks the lattice of aluminum. The Al-1.5Mn alloy with ΔMk value of 0.008 showed the same value between the Mk_α and Mk_t , which meant the formation of the α -Al phase by the perfect solution of added elements in it. In contrast, 6.0Mg, 3.3Si and Al-9Si, 0.2Mo+0.2Zr alloys showed different values between Mk_α and Mk_t , which meant the decision of compositions of both the α_p -Al phase and the eutectic by a certain partition ratio of each element, the

existence of solid solubility limit (Points A and B) of each element in the α -Al phase and the increase of the eutectic.

5.3.2 Mechanical properties for as-cast applicability

The Al-1.5Mn alloy showed a strengthened plastic deformation behavior compared with the A1070. The values of the $\sigma_{0.2}$, σ_{UTS} and ε_f were 47MPa, 95MPa, and 18% in the Al-1.5Mn alloy, respectively. The 1.0Si addition alloy showed strengthened tensile behavior with the $\sigma_{0.2}$ of 61MPa, σ_{UTS} of 148MPa, and ε_f of 18%, compared with the Al-1.5Mn alloy. The increase stress and strain resulted from the increment of solid solution strengthening level caused by the increase in ΔM_k value of the alloys. The 3.3Si addition alloy showed the strengthened tensile behavior with the $\sigma_{0.2}$ of 67MPa and σ_{UTS} of 160MPa, although the ε_f was reduced to 9%. The increase and decrease in flow stress and strain resulted from the increment of microstructure refinement caused by the $Al_{12}Mn_3Si$ acted as the nucleation sites for the α -Al phase and solid solution strengthening level caused by the increase in ΔM_k value of the alloys.

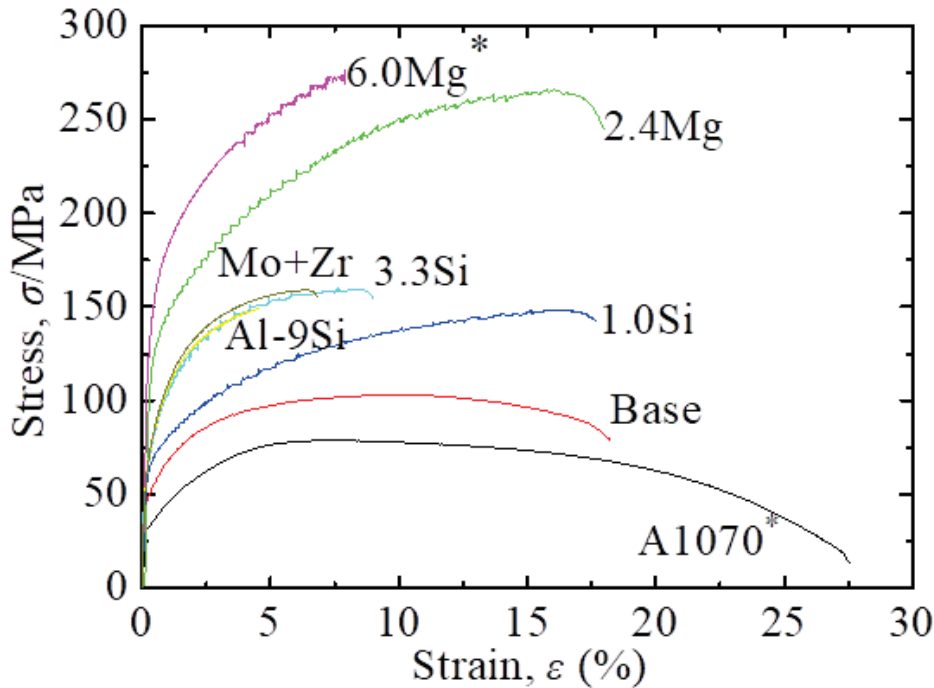


Fig. 5.4 Nominal tensile stress-strain curves of the experimental alloys.

The 0.2Mo+0.2Zr addition alloy showed improvement in both σ_{UTS} (160MPa) and ϵ_f (7.1%) at the as-cast conditions, compared with those (145 MPa, 6.1%) of the Al-9Si alloy. The ID consisting of eutectic and IMCs showed maximum hardness in alloys, especially since their error bars were large, and their values varied widely in the 0.2Mo+0.2Zr alloy in Fig. 3.13. It is considered that the characterizations of the eutectic structure are the main reason why both the strength and ductility, which are usually in a reciprocal relationship, are improved. Small IMCs such as Al_3Zr , $Al_{12}Mo$, and $Al_{15}(Fe, Mn, Mo)_3Si_2$ were clustered dispersedly in or near the eutectic grains of the 0.2Mo+0.2Zr addition alloy. Thus, the increase of the volume fraction of the Al_3Zr and $Al_{12}Mo$ improved the tensile strength because of the solid solution and precipitation hardening mechanisms.

In contrast, for improvement in ductility, the inhomogeneity α -Al phase in eutectics with 72.2% as a continuous layer, exhibiting a high Al content layer or depleted area of solutes, which was formed by the clustered distribution of the Al_3Zr and $Al_{12}Mo$, which could improve the ductility of the 0.2Mo+0.2Zr addition alloy. Therefore, the

inhomogeneity eutectic grains, including of IMCs, acted as the harmonic structure for enhancing strength and ductility.

The relationship between ΔMk_α , 5% dislocation density (ρ) and 5% flow stress of the experimental alloys is shown in Fig. 5.5. The definition of ΔMk_α and ρ is the average value of the alloy for different series of the alloys, the formula is as follows:

$$\Delta Mk_\alpha = \Delta Mk_{p\alpha} \times V.f_{p\alpha} + \Delta Mk_{e\alpha} \times V.f_{e\alpha} \quad (5-1)$$

$$\rho = \rho_{p\alpha} \times V.f_{p\alpha} + \rho_{e\alpha} \times V.f_{e\alpha} \quad (5-2)$$

Where, $\Delta Mk_{p\alpha}$ is the ΔMk value of primary α -Al phase. $V.f_{p\alpha}$ is volume fraction of primary α -Al phase. $\Delta Mk_{e\alpha}$ is the ΔMk value of eutectic α -Al phase. $V.f_{e\alpha}$ is volume fraction of eutectic α -Al phase. $\rho_{p\alpha}$ is 5% dislocation density of primary α -Al phase, $\rho_{e\alpha}$ is 5% dislocation density of eutectic α -Al phase.

There was a good relationship between ΔMk_α and dislocation density, regardless of kinds of alloys. The Si and Mg had low and high Mk_i values, or small and large atomic radius, or large and small electronegativity, respectively. The elastic interaction is caused by the difference in atomic size between the solute and the solvent atoms. In contrast, the charge transfer occurs based on the difference in electronegativity between the solute and the solvent atoms. The charge transfer between the solute and the solvent atoms may contribute to the bond strength between them. The dislocation density of Si and Mg addition alloys increased in the proportion to the ΔMk_α value, compared with the base alloy. The increase of ΔMk_α meant that the solid solution level of the alloy increases, that is, the solid solution strengthening effect is enhanced. Solid solution strengthening is beneficial to the improvement of alloy strength. Thus, there was a good relationship between ΔMk_α and 5% flow stress.

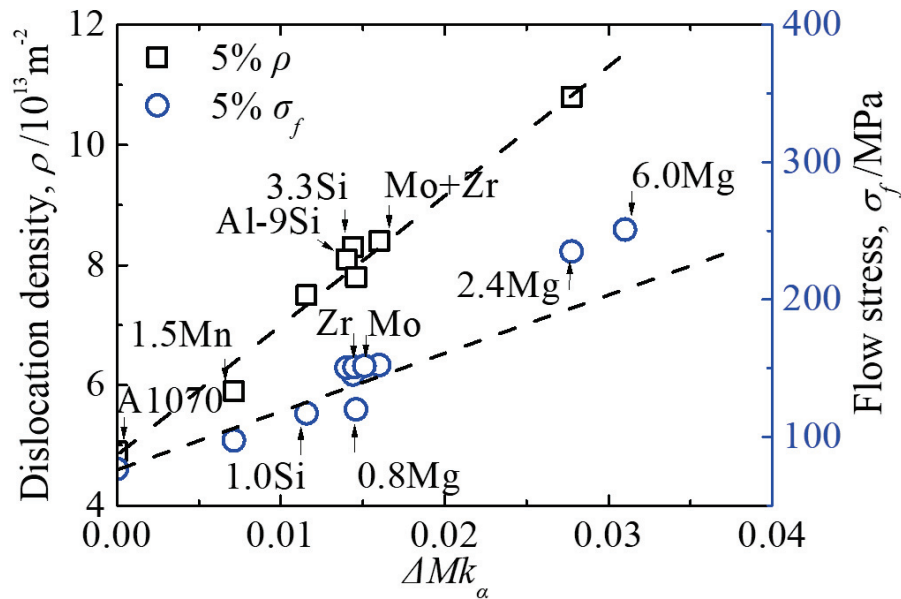


Fig. 5.5 Relationship between $\Delta M k_{\alpha}$ value and the dislocation density and flow stress of the experimental alloys.

The composition of the 1.0Si addition alloy was close to the limit solid solubility of the Al-1.5Mn-XSi alloy, the increase in tensile strength was mainly caused by solid solution strengthening. However, the 3.3Si addition alloy had the composition exceeded the limit solid solubility of the Al-1.5Mn-XSi alloy. There were more IMCs and Si phases in the microstructures. They were acted as the nucleation site of Al phase and refined the size of Al phase, but the brittle phase of high hardness reduces the ductility of the alloy by 50%. The increase in the strength of the 3.3 addition alloy was mainly due to the refinement of the microstructure compared with the 1.0Si addition alloy.

The 0.2Mo+0.2Zr addition alloy showed improvement in both σ_{UTS} and ϵ_f at the as-cast conditions, compared with the Al-9Si alloy. It was found, based on progress in tensile properties, that both usages of the gravity casting method and the addition of Mo and Zr suggested the possibility for the as-cast application because the eutectic Si particles were refined due to the crystallization of both IMCs, and both IMCs acted as a nucleation site for eutectic Si. Furthermore, the eutectic α -Al phase was characterized by high Al content or low $\Delta M k_{e\alpha}$ region by micro-segregation of the Mo and Zr atoms.

5.4 Summary

1) The addition of elements refined the solidified structure of the addition of Si to Al-1.5Mn and the addition of Mo+Zr to Al-9Si with the SDAS of 47.9, 36.5, 41, and 33 μm , respectively.

2) The decrease or increase in lattice constant was related to the amounts of solid solution elements in the α -Al phase. The different values between Mk_{α} and Mk_t , which meant the decision of compositions of both the α_p -Al phase and the eutectic by a certain partition ratio of each element, the existence of solid solubility limit of each element in the α -Al phase and the increase of the eutectic.

3) The Al-1.5Mn, 1.0Si, 3.3Si, 0.8Mg, 2.4Mg and Al-9Si, Mo+Zr alloys show a linear relationship between the dislocation density, flow stress under the same plastic strain rate in each alloy increased with increasing of ΔMk value of the α -Al phase, regardless of alloy series and additive elements.

4) It was shown that electronic method could predict the mechanical properties of aluminum alloys regardless of alloy series and additive elements, which was convenient for designing high performance aluminum alloys efficiently for as-cast applicability. The alloy with composition close to the limit solid solution had a certain strength and high ductility. The alloys with component exceeded the limit solid solution, eutectic phases and intermetallic compounds appeared in the structures, resulting in decrease in ductility. In addition, Intermetallic compounds were precipitated at higher temperatures, and they acted as nucleation sites for the primary or eutectic phase, thereby improving the strength of the alloy.

References

- 1) Nabarro F R N 1967 Theory of Crystals Dislocations (Oxford Clarendon)
- 2) Johnston W G 1962 J. Appl. Phys 33 2716.
- 3) Morinaga M, Nasu S, Adachi H, Saito J and Yukawa N 1991 J. Phys.: Condens. Matter 3 6817.
- 4) Mulliken R S 1955 J. Chem. Phys. 23 1833, 1841,2339 and 2343
- 5) Mura T 1987 Micromechanics of Defects in Solids (Dordrecht: Martinus Nijhoff)
- 6) Nabarro F R N 1967 Theory of Crystals Dislocations (Oxford Clarendon)
- 7) M. Morinaga, N. Yukawa and H. Adachi: Tetsu-to-Hagane **72** (1986) 555-562.
- 8) M. Morinaga, N. Yukawa: "Alloy Design Base on Molecular Orbital Method"
Computer Aided Innovation of New Materials, Amsterdam (1991) 803-808.
- 9) M. Morinaga, S. Nasu, H. Adachi, J. Saito and N. Yukawa: J. Phys. Condens. Matter **3** (1991) 6817-6828.
- 10) M. Morinaga and S. Kamado: Model. Simul. Mater. Sci. Eng. **1** (1993) 151-164.
- 11) Mura T 1987 Micromechanics of Defects in Solids (Dordrecht: Martinus Nijhoff)

Appendix 1

Alloys series	Alloys	Volume fraction (%)		
		α -Al (a_p+a_e)	Si	IMCs
Pure	Al1070	99.97	0	0.03
Al-1.5Mn	Base	99.3	/	0.7
	0.8Mg	99.8	/	0.2
	1.0Si	98.6	/	1.4
	2.4Mg	99.5	/	0.5
	3.3Si	96.1 (0.03+0.97)	0.3	3.6
	6.0Mg	98.3	/	1.7
Al-9Si-0.3Fe-0.15Mn	Base	89.1 (0.33+0.67)	8.5	2.4
	0.2Mo	88.6	8.5	2.9
	0.2Zr	88.8	8.4	2.8
	0.2Mo+0.2Zr	88.1 (0.27+0.73)	8.4	3.5

Conclusions

In the context of reducing manufacturing costs, the practical application of casting has received attention. Focusing on Al-1.5Mn-based and Al-9Si-based alloys, which are widely used as automotive body parts, the alloys have been characterized and tested for their mechanical properties, considering that there is a unified viewpoint even if the alloys are different in series. A quantitative method for predicting the mechanical properties of Al-1.5Mn-based and Al-9Si-based alloys was proposed on the basis of the ΔMk parameter. The conclusions of this thesis are summarized as follows:

1. The addition of Si to Al-1.5Mn and the addition of Mo+Zr to Al-9Si increased the strength of the alloy by 43.7% and 8.9%, respectively. The addition of elements refined the solidified structure of the base alloy with the SDAS of 47.9, 36.5, 41, and 33 μm , respectively.
2. The lattice constant decreased linearly with the increase in ΔMk_t values. It is considered that the decrease in lattice constant was related to the amounts of solid solution elements in the α -Al phase. The different values between Mk_α and Mk_t , which meant the decision of compositions of both the α_p -Al phase and the eutectic by a certain partition ratio of each element, the existence of solid solubility limit of each element in the α -Al phase and the increase of the eutectic.
3. The increase in the strength of the as-cast alloy was attributed to the degree of solid solution strengthening of the continuous α -Al phase. Furthermore, the increase in ductility was attributed to the degree of segregation of solid solution element concentrations in the α -Al phase. As a result of the dislocations, it was found that there

were places where dislocations aggregated and places where there were few dislocations in the α -Al phase. Therefore, it is believed that ductility occurs in the depleted region of solute elements, and in as-cast alloys, it is believed that the random distribution of the α -Al phase with a low concentration of solute elements improves ductility.

4. The Al-1.5Mn, 1.0Si, 3.3Si, 0.8Mg, 2.4Mg and Al-9Si, Mo+Zr alloys show a linear relationship between the dislocation density, flow stress under the same plastic strain rate in each alloy increased with increasing of ΔMk value of the α -Al phase, regardless of alloy series and additive elements.

5. It was shown that electronic method could predict the mechanical properties of aluminum alloys regardless of alloy series and additive elements, which was convenient for designing high performance aluminum alloys efficiently for as-cast applicability. The alloy with composition close to the limit solid solution had a certain strength and high ductility. The alloys with component exceeded the limit solid solution, eutectic phases and intermetallic compounds appeared in the structures, and resulting in decrease ductility. In addition, Intermetallic compounds were precipitated at higher temperatures, and they acted as nucleation sites for the primary or eutectic phase, thereby improving the strength of the alloy.

Acknowledgements

I would like to express my gratitude to all those who helped me during the writing of this thesis. My deepest gratitude goes first and foremost to Professor Kazuhiro Matsugi, my supervisor, for his constant encouragement and guidance. He provided me with abundant suggestions and priceless criticisms for my writing of the thesis. Without his consistent and illuminating instruction, this thesis could not have reached its present form. He gave me full support not only on my research, but also on my life and career, which has played an important role in both of my professional and personal development.

My sincere thanks go to Professor Yongbum Choi and Professor Zhefeng Xu. They gave me so much positive help on the research, the accumulation of the knowledge and my life, and I have learnt so much from them. In addition, I would like to express my heartfelt thanks to Professor Gen Sasaki, Professor Kenjiro Sugio in Hiroshima University and Nobuyuki Oda in Mazda Motor Corporation for their technical advice and experimental assistance. And my sincere thanks also go to the Doctor Yingju Wu at Yanshan University for their FIB and TEM assistance.

I am thankful to Doctor Shaoming Kang, Doctor Meiqi Yu for considerable assistance and help in my experiments and my life when I first came to Japan. Moreover, I would also like to thank all the past and present members of Property Control of Materials Laboratory, in Department of Mechanical Physical Engineering, Hiroshima University, for their enthusiastic help to both of my life and study.

I also owe my sincere gratitude to Japan Foundry Engineering Society Found.

Finally, I would like to thank to my parents and my girlfriend who are always by my side and back up me no matter where I am and what I am.

Published papers in regard to this thesis

1. **Zeze Xiao**, Kazuhiro Matsugi, Zhefeng Xu, Nobuyuki Oda, Hironobu Kominato and Yasuo Uosaki. Effects of 0.2Mo +0.2Zr Addition on Microstructure and Tensile Properties of Al -9Si -0.3Fe -0.15Mn Casting Alloy, *Materials Transactions*, Vol. 63, No. 10, pp. 1452-1563, Aug 2022. (Chapter 3& 5)

2. **Zeze Xiao**, Kazuhiro Matsugi, Zhefeng Xu, Yongbum Choi, Kenjiro Sugio, Nobuyuki Oda and Jinku Yu. Effect of Si Addition on Microstructure and Mechanical Properties of Al1.5%Mn Alloys, *Materials Transactions*, Vol. 61, No. 7, pp. 1355 to 1363, May 2020. (Chapter 2& 5)

3. **Zeze Xiao**, Kazuhiro Matsugi, Zhefeng Xu, Taishi Matsuoka, Tomoshi Uomi, Nobuyuki Oda, Hironobu Kominato and Yasuo Uosaki, Characterizations of the Microstructural and Tensile Properties of Al-9Si-0.3Fe-0.15Mn Alloys with Ti and V Additions, *The 10th Pacific Rim International Conference on Advanced Materials and Processing (PRICM-10)*, pp. 449-456, Aug 2019. (Chapter 4& 5)

Presentations

1. **Zeze Xiao**, Kazuhiro Matsugi, Zhefeng Xu, Nobuyuki Oda, Hironobu Kominato and Yasuo Uosaki. Effects of 0.2Mo +0.2Zr Addition on Microstructure and Tensile Properties of Al -9Si -0.3Fe -0.15Mn Casting Alloy, *Materials Transactions*, Vol. 63, No. 10, pp. 1452-1563, Aug 2022.

2. **Zeze Xiao**, Kazuhiro Matsugi, Zhefeng Xu, Yongbum Choi, Kenjiro Sugio, Nobuyuki Oda and Jinku Yu. Effect of Si Addition on Microstructure and Mechanical Properties of Al1.5%Mn Alloys, *Materials Transactions*, Vol. 61, No. 7, pp. 1355 to 1363, May 2020.

3. **Zeze Xiao**, Kazuhiro Matsugi, Zhefeng Xu, Taishi Matsuoka, Tomoshi Uomi, Nobuyuki Oda, Hironobu Kominato and Yasuo Uosaki, Characterizations of the Microstructural and Tensile Properties of Al-9Si-0.3Fe-0.15Mn Alloys with Ti and V Additions, *The 10th Pacific Rim International Conference on Advanced Materials and Processing (PRICM-10)*, pp. 449-456, Aug 2019.

4. **Zeze Xiao**. Effect of Si Addition on Microstructure and Mechanical Properties of Al1.5%Mn Alloys. 日本鑄造工学会 中国四国支部. (Katajima Award)

5. **Zeze Xiao**, Kazuhiro Matsugi, Zhefeng Xu, Nobuyuki Oda, Hironobu Kominato and Yasuo Uosaki. Development of Al-9Si-Mo/Zr alloys for their as-cast applications. 第10回 軽金属学会 中国四国支部 講演大会. July 28, 2018, Hiroshima, Japan; Hiroshima Institute of Technology University.

6. **Zeze Xiao**, Kazuhiro Matsugi, Zhefeng Xu. Effect of Si additions on microstructural and mechanical properties of Al-1.5Mn-xSi alloys for as-cast usages. Aug 3, 2019. Okayama, Japan; Okayama University of Science.

7. **Zeze Xiao**, Kazuhiro Matsugi, Zhefeng Xu, Yongbum Choi. Fabrication of Al-1.5Mn-XSi alloys for as-cast usages. 日本鑄造工学会 第174回全国講演大会, Sep 28-29, 2019 福岡国際会議場.

8. **Zeze Xiao**, 日本鑄造工学会 第4回学生鑄物コンテスト, Sep 9-10, 2018. Morioka, Japan; Iwate University. (Rewards)
9. **Zeze Xiao**, Kazuhiro Matsugi, Zhefeng Xu, Yongbum Choi. 鑄放し状態で使用可能なAl-1.5Mn系合金の作製. 産学地域連携センター. Feb 23, 2019, Hiroshima, Japan; Hiroshima University.
10. **Zeze Xiao**, Jinku Yu, Lili Zhao, Kazuhiro Matsugi, Zhefeng Xu, Yongbum Choi, Meiqi Yu. Fabrication of Ni-Fe-W alloy coatings by Jet-electrodeposition. 日本鉄鋼協会・日本金属学会 中国四国支部 鉄鋼第59回・金属第57回 合同講演大会. August 21, 2017, Kochi, Japan; Kochi University of Technology.
11. **Zeze Xiao**, Kazuhiro Matsugi, Yongbum Choi, Kenjiro Sugio, Tatsuya Kakui, Zhefeng Xu. Al-9Si合金の組織および引張特性に及ぼすMoおよびZr添加の影響. 日本鑄造工学会 第180回全国講演大会, Sep 27-30, 2022. Hiroshima, Japan; Hiroshima University.

Awards

1. **Zeze Xiao**, 日本鑄造工学会 第4回学生鑄物コンテスト, Sep 9-10, 2018. Morioka, Japan; Iwate University. (Rewards)

2. **Zeze Xiao**. Effect of Si Addition on Microstructure and Mechanical Properties of Al1.5%Mn Alloys. 日本鑄造工学会 中国四国支部. (Katajima Award)